Hemp-lime Composite Integration with Phase Change Materials and their Application in Cold Climates

Yaser Abdellatef

Thesis submitted to the University of Ottawa in partial Fulfillment of the requirements for the degree of Doctor of Philosophy in Civil Engineering

Academic Advisor: Prof. Miroslava Kavgic

Department of Civil Engineering
Faculty of Engineering
University of Ottawa

ABSTRACT

This research explores developing, characterizing, and analyzing a new low-carbon composite material combining hemp-lime (hempcrete) and phase change materials (PCMs) for enhanced thermal performance in buildings. The study is divided into four main phases. In the first phase, novel hemp-lime composites were created using recycled, locally sourced, low-embodied energy binders and pozzolans. These composites were experimentally characterized for mechanical, thermal, and moisture buffering properties. Results showed that density affects hempcrete's properties and locally sourced pozzolans like metakaolin and recycled brick performed better than traditional hydraulic lime.

The second phase included developing new hemp-lime composites with metakaolin and microencapsulated PCMs (MPCM). Numerical simulations compared the energy performance of timber-frame walls with hempcrete and HPCMs. The inclusion of MPCMs enhanced the heat storage potential of the composites.

Consequently, in the third phase, a novel hysteresis modelling approach was proposed to improve the accuracy of phase change simulations. The new model was validated experimentally and compared with existing hysteresis methods. The study highlighted the importance of selecting appropriate hysteresis models and PCM integration techniques. Finally, numerical simulations investigated the effect of different heating schedules on hempcrete-PCM wall assemblies. The scenarios tested included heating setback temperature and temperature ramp-up. Results indicated that changing setpoints significantly influences PCM behaviour and wall thermal performance.

Overall, this research demonstrates the potential of PCM-enhanced hemp-lime composites as sustainable building materials with improved thermal mass capacity suitable for cold climates like Canada.

ACKNOWLEDGMENT

I would like to thank my academic supervisor, Dr. Miroslava Kavgic, whose guidance and support have been elemental in completing this doctoral thesis. I also wish to extend my gratitude to Dr. Scott Ormiston for his guidance in the entire journey and his valuable contributions to this thesis. I also want to thank Dr Evola Gianpiero and my colleagues, Asif Khan, Amil Khan, and Mehdi Iftekhar, for their excellent assistance. I am thankful to my parents for their encouragement throughout my journey. I offer my sincerest appreciation to everyone who has played a role in shaping this thesis and my journey as a scholar. Thank you for being a part of this milestone in my career.

TABLE OF CONTENTS

LIST OF TABLES

LIST OF FIGURES

NOMENCLATURE AND SYMBOLS

C_p	specific heat capacity (J/kg K)
h	enthalpy (J/ kg)
k	thermal conductivity (W/m K)
Q	heat flow meter's signal output (μV)
q''	heat flux (W/m^2)
S	heat flow meter's calibration factor ($W/(m^2\ \mu V)$
S_E	source term in energy equation (W/m^3)
T	temperature (^oC)
t	time (seconds)
V	wind speed (m/s)
ρ	density (kg/m^3)
β	liquid fraction
HFMA	heat flow meter apparatus
PCM	phase change material
MPCM	microencapsulated phase change material
HPCM	hempcrete-phase change material composite
H-Micro	hempcrete-microencapsulated phase change material composite
H-Panel	hempcrete-panel phase change material composite
RMSD	Root mean square difference
CV(RMSD)	Normalised root mean square difference

1. Introduction

1.1. Context

The building sector is one of the significant contributors to energy consumption and its greenhouse gas emissions [1, 2]. Therefore, new technologies are emerging to improve energy efficiency in buildings while maintaining the occupants' thermal comfort criteria [3, 4]. Furthermore, according to the International Energy Agency (IEA), energy-related greenhouse gas emissions are expected to double by 2050 if the building sector does not undergo drastic energy efficiency improvements [5]. The building envelope is a crucial component of the building structure that separates the external environment and internal space and, as such, plays a crucial role in determining the building's energy consumption [6]. Hence, utilizing efficient passive technologies in envelopes is a must to improve the energy efficiency of buildings [7].

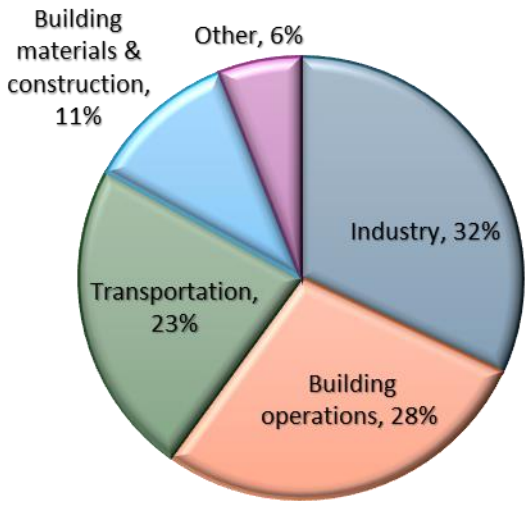

Figure 1.1. Global CO2 emission by sectors [8].

Thermal energy storage is one of the most efficient techniques in sustainable buildings, and it can reduce energy consumption and its associated greenhouse gas emissions [9]. Phase change material (PCM) is a latent heat storage technique through a change of the material phase with low or no

temperature variation, which has a high energy storage density compared to sensible heat storage technologies [10]. Hence, the integration of PCMs in building envelopes can reduce the influence of the outdoor weather on indoor conditions and decrease cooling and heating energy demands while maintaining thermal comfort by absorbing part of a building's heat load during the daytime while melting and discharging this stored heat back during the cooler night-time through freezing [11].

According to their phase change processes, there are three main types of PCMs: solid-liquid PCMs, solid-solid PCMs, and solid-gas (or liquid-gas) PCMs [12]. Although the phase change by evaporation has a high latent heat, it adds some applicability difficulties, such as high volume and pressure changes during the phase transition process [12]. The solid-liquid transition is preferred for thermal energy storage in building applications since it does not experience significant volume change during the phase transition and has high latent heat in the temperature ranges related to building comfort requirements [13]. Moreover, solid-solid PCMs are similar to solid-liquid PCMs, without any risk of leakage problems, but with significantly lower energy storage capacity in the temperature ranges required for building applications [12].

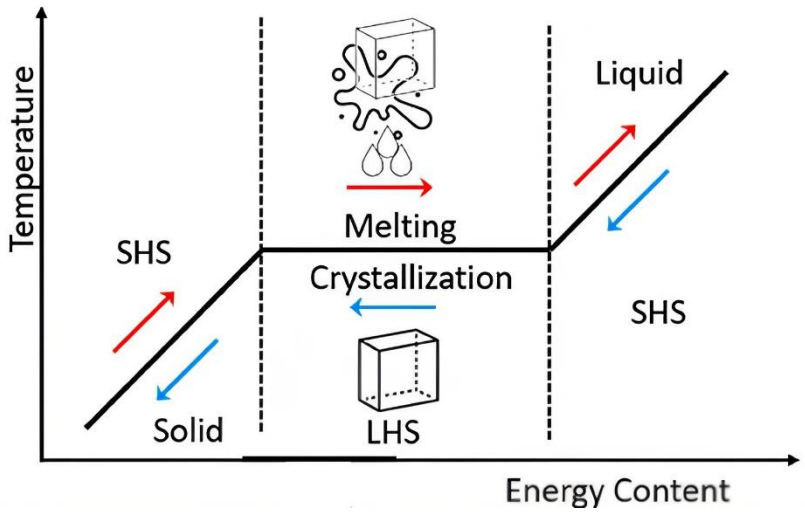

Figure 1.2. PCM working principle [14].

However, several challenges must be overcome to efficiently apply PCMs in building envelopes. One of the significant barriers reported for expanding the use of PCMs is their relatively high cost [15]. Moreover, the heat transfer with phase change process in PCMs is accompanied by complex phenomena such as hysteresis and partial phase change processes [16, 17], which require careful assessment, appropriate modelling, and control strategy to make their integration fully effective and maximize energy savings. [18]. Neglecting such complex properties of PCMs can overestimate/underestimate the energy savings and thermal behaviour of adding PCMs to walls. Therefore, the efficient and cost-effective application of PCMs requires optimal integration into the building envelope harmonized with the heating, ventilation, and air-conditioning (HVAC) system operation to consider their accurate thermal properties and complex phase change behaviour.

Numerical analysis is a widely used method to investigate and test the integration of PCMs into building envelopes under different design strategies, HVAC operations, and weather conditions to find optimal solutions cost-effectively [19-21]. In particular, numerical simulation can help define the control strategies that facilitate optimal charge and discharge of PCMs embedded into the building envelope to ensure their effective operation [22]. Although a realistic simulation of the PCM is essential, the widely available hysteresis models (Track, Switch, Scale) utilize simplified techniques in interrupted phase change situations, such as remaining on the same phase change curve and neglecting hysteresis (i.e., Track model), or following a sensible storage approach in transition between phase change curves (i.e., Switch and Scale models). Therefore, the simulation predictions of these models do not correspond to the actual behaviour and show significant discrepancies compared to the experimental observations, which can underestimate/overestimate the potential energy savings of the passive application of the PCMs.

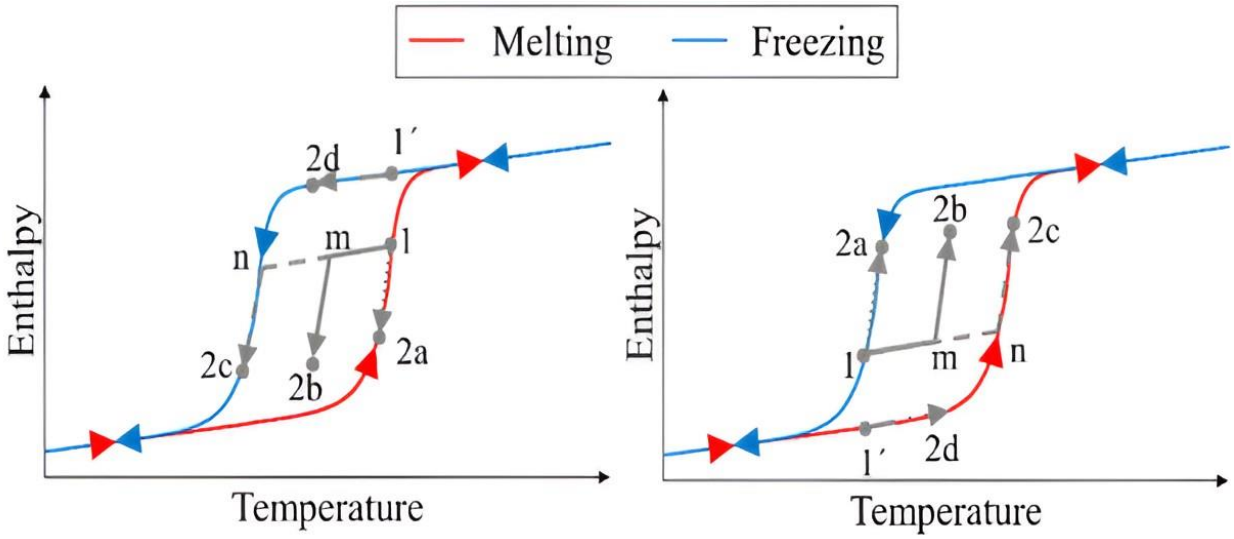

Figure 1.3. Principle of operation for the hysteresis models (Path 1-2a: Track model; Path 1-n-2c: Switch model; Path 1-m-2b: Scale model) [23].

Using lightweight bio-based building materials in envelopes can decrease the high embodied energy problem associated with conventional building materials usually integrated with PCMs (e.g., gypsum, concrete) [24]. For example, lightweight bio-based composites, typically made of mineral binder and bio-aggregate particles, can reduce embodied energy through cost-effective manufacturing and recycling processes and offer a low-carbon or carbon-negative potential [25]. In this respect, lignocellulosic materials, such as hemp, flax, and wood particles, are abundant waste materials in the Canadian agriculture and forestry industries with the potential to decarbonise the construction industry due to their carbon sink properties. In particular, biobased building materials, such as cementitious lignocellulosic composites (e.g., hempcrete, woodcrete), provide an excellent balance between thermal insulation and thermal mass while having a high moisture-buffering capacity, improving energy performance and indoor hygrothermal comfort [26-28]. For example, hempcrete, made of the hemp plant's core mixed with a lime-based binder, is a promising lightweight bio-composite material that can solve the high embodied energy problem and improve the energy sustainability of buildings [25, 29]. A hempcrete-based envelope can have many distinct

advantages, including excellent thermal properties [30, 31], high acoustic performance [27], high moisture buffering [32], good fire resistance [33, 34], high carbon sequestration [25], and simplification and reduction in the number of layers and processes involved in timber-frame construction [33, 35]. Considering that hemp hurd contributes to hempcrete's thermal insulating and low-carbon properties, an increase of hemp hurd in the mix design is desirable. However, a higher hemp amount also leads to a lower specific heat capacity of the hempcrete mixture, lowering its ability to absorb and store thermal energy and ultimately reducing thermal inertia against outdoor weather fluctuations, leading to increased heating and cooling energy demand of the building envelope [36].

Lightweight building materials often have lower thermal mass than conventional heavyweight materials, resulting in lower thermal inertia against outdoor weather fluctuations, higher heating and cooling energy consumption, and higher operational carbon [36]. Thus, the passive integration of PCMs in the envelopes of lightweight structures can increase the building's storage capacity and thermal inertia [37]. Nevertheless, there is a lack of research on integrating PCMs with lightweight, low-embodied energy materials, while the existing studies mainly focused on heavyweight or high-embodied energy composites [12]. Considering all the advantages, hempcrete represents an excellent alternative to conventional building materials for mixing with PCMs as, on the one hand, such mix design could reduce the embodied carbon of the PCM-enhanced composite and, on the other hand, could exhibit better thermal storage potential than traditional hempcrete. Yet, this potential has to be explored, as the only research study focused on PCM hemp-lime composite material only investigated its flammability [38]. At the same time, other vital physical properties and performance aspects of such composites (hempcrete-PCM) remained unexamined, such as thermal properties, moisture buffering performance, accurate numerical representation, potential

integration into the envelope assemblies, and the impact of HVAC control strategies on hempcrete-PCM efficiency.

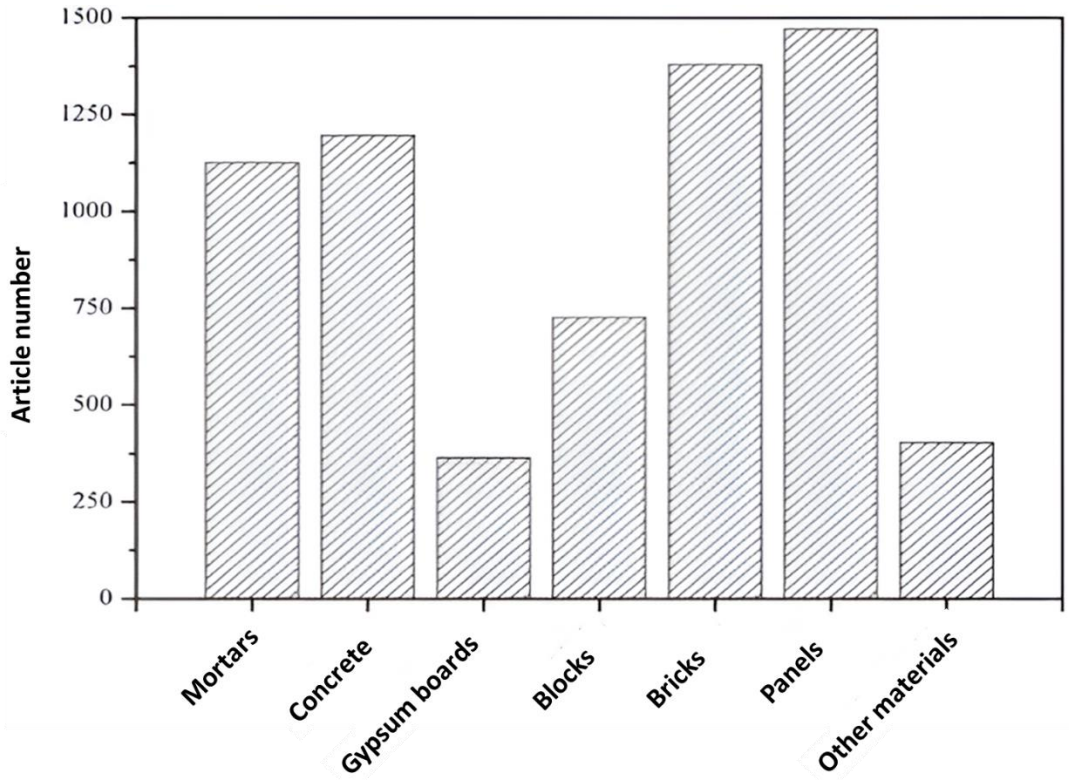

Figure 1.4. Articles number for PCM integration with different construction materials [12].

1.2. Research objectives

The research study aims to develop, experimentally characterise, and numerically analyse a new low-carbon latent heat storage, PCM-enhanced hemp-lime composites with excellent hygrothermal properties suitable for cold Canadian climates and maximised content of locally sourced ingredients. The following objectives that contribute to the overall goal have been undertaken:

- Develop and characterise hygrothermal and mechanical properties (i.e., compressive and tensile strength) of various hempcrete mix designs made of locally sourced ingredients,

including hemp hurd, non-hydraulic binders such as hydrated lime, and natural pozzolans such as metakaolin and crushed brick.

- Develop and characterise hygrothermal properties of PCM-enhanced hemp-lime composites with excellent insulating and thermal storage properties using two microencapsulated PCM types and previously developed hempcrete from locally sourced ingredients. The PCM-enhanced hemp-lime composites are created by carefully considering the hemp-to-binder ratio and percent share of microencapsulated PCMs to minimize the negative impact on the mechanical properties and fire resistance while improving the new latent composite's thermal insulating and storage potential.
- Extend material-level experimental analysis to envelope assembly applications for cold climates through comprehensive numerical investigation and comparison between the thermal performance of hempcrete and PCM-enhanced hempcrete as infills in buildings' timber-frame walls.
- Develop a new model for realistic simulation of complex hysteresis phenomenon and partial (incomplete) phase change processes, occurring when the melting process is interrupted and followed by the freezing process (and vice versa) within ANSYS Fluent.
- Validate the new hysteresis model against experimental results and compare its performance with three widely used simulation methods: Track, Switch, and Scale using two different PCM integration methods in walls, microencapsulation (PCM enclosed in microcapsules), and macroencapsulation (PCM encased in pouches or panels of various sizes, making independent layers).
- Investigate the impact of heating setpoints and PCM percentage on the performance of PCM-enhanced hempcrete walls and develop control strategies that facilitate their charge

and discharge while reducing undesirable increases in energy consumption of wall assembly with PCM.

1.3. Contribution to the field

This thesis's contributions to the field of low-carbon thermal storage building materials for passive envelope applications are several, including:

- A limited number of studies conducted in Canada used only locally sourced materials to create hempcrete mixes. This study closes this gap by developing hempcrete mixes using ingredients widely available in Canada to, on the one hand, enable the reduction of hempcrete's price and embodied energy as ingredients wouldn't be shipped from abroad and, on the other hand, contribute to an increase in hempcrete's availability and affordability.
- Most previous studies in their hempcrete mix designs used pozzolans such as hydrated lime, which is not locally produced in Canada and must be imported. This study's contribution is introducing the possibility of using recycled crushed brick as a pozzolan for the first time to reduce the hempcrete's embodied energy and showing comparative hygrothermal and mechanical behaviours against hempcrete mixes made with traditionally used pozzolans such as hydraulic lime.
- In contrast to the existing studies that applied higher binder than hurd share for wall formulas to increase mechanical strength, this research focused on maximizing the hemp hurd amount with a hemp-to-binder ratio of 1:1 by weight for a targeted density of 300 kg/m³ to 400 kg/m³ to improve hempcrete's thermal properties while reducing carbon footprint and price.
- For the first time, this study uses microencapsulated PCMs integrated with hempcrete composites to develop low-carbon thermal storage materials with enhanced storage density and characterize their thermal and moisture behaviour.

- This study advanced the field of numerical representation of PCMs by developing a new model for realistic modelling of the hysteresis process, including incomplete phase change, necessary for accurate energy-saving predictions. Furthermore, this is the first study to introduce such an advanced hysteresis model in the widely used software ANSYS Fluent, which until now used an oversimplified representation of PCMs. Additional contributions include a comparison against three popular hysteresis simulation methods using two widely used PCM integration methods into envelope components, microencapsulation, and macroencapsulation.
- Although PCMs must change their phase daily to be fully effective, a limited number of studies have investigated the impact of HVAC setpoints on the performance of PCMs installed in building envelopes. Therefore, different heating setpoint strategies designed to improve the energy-saving potential of PCM-enhanced hempcrete wall assemblies have been investigated to address this research gap.
- Real-world application of building materials requires detailed characterisation of all vital physical parameters, and in cold climates such as Canada, hygrothermal behaviour is paramount. Hence, unlike previous studies that examined the mechanical performance of hempcrete mix designs, this research focuses on measuring hygrothermal properties that describe the insulating, storing, and moisture-buffering potential of hempcrete and PCM-enhanced hempcrete.

1.4. Scientific publications

The publications resulting from this thesis, categorized as peer-reviewed journal and conference papers, include:

Journal papers:

1- Abdellatef, Y., Khan, M.A., Khan, A., Alam, M.I. and Kavgic, M. (2020) "Mechanical, Thermal, and Moisture Buffering Properties of Novel Insulating Hemp-Lime Composite Building Materials." Materials (MDPI).

2- Abdellatef, Y. and Kavgic, M. (2020) "Thermal, microstructural and numerical analysis of hempcrete-microencapsulated phase change material composites." Applied Thermal Engineering.

3- Abdellatef, Y. and Kavgic, M. Ormiston, S., Evola, G. (2024) "Hysteresis model predictions of thermal performance of hempcrete-based walls with phase change materials" Journal of Building Engineering.

4- Kavgic, M. and Abdellatef, Y. (2021) "Temperature Control to Improve Performance of Hempcrete-Phase Change Material Wall Assemblies in a Cold Climate." Energies (MDPI).

Conference papers:

1- Abdellatef, Y. and Kavgic, M. Foruzanmehr, R. (2021) "Thermal and moisture buffering properties of novel hemp-lime composites integrated with microencapsulated phase change materials" Proceedings of the 4th International Conference on Bio-based Building Materials, Barcelona, Spain.

2- Abdellatef, Y. and Kavgic, M. (2022) “Improvement of the hempcrete-phase change material wall performance during the heating season using temperature control strategies” Proceedings of eSim 2022:12th Conference of IBPSA-Canada.

1.5. Outline of the thesis

The thesis is divided into seven chapters**. Chapter 1** presents a general context, objectives, and contributions to the field.

Chapter 2 provides a literature review of this research's different aspects, including energy consumption in buildings, phase change materials, hemp-lime composites, and defining the research gap and objectives.

Chapter 3 briefly describes the methodology overview of this research, with more details provided in the following chapters.

Chapter 4 describes hempcrete composites' mechanical, thermal, and moisture buffering properties. The chapter describes the composition of hempcrete, the experimental setup, and the results of the experiments. This chapter is published in the journal article “*Mechanical, Thermal, and Moisture Buffering Properties of Novel Insulating Hemp-Lime Composite Building Materials*.” Materials (MDPI).

Chapter 5 presents the hempcrete-PCM (HPCM) samples that were produced and the experimental analysis performed on them, including thermal conductivity and specific heat capacity measurements. Then, the hempcrete and HPCM wall sections were numerically analyzed to compare the wall’s thermal performance throughout the year. The material presented in this chapter is from the journal and conference articles; “*Thermal, microstructural and numerical analysis of hempcrete-microencapsulated phase change material composites*.” Applied Thermal

Engineering, and "*Thermal and moisture buffering properties of novel hemp-lime composites integrated with microencapsulated phase change materials*," Proceedings of the 4th International Conference on Bio-based Building Materials, Barcelona, Spain.

Chapter 6 analyses the hysteresis modeling of PCMs and their effect on the wall performance. A comparison and validation were performed between the developed MScale model and the widely available models (Track, Switch, and Scale). Then, it compares the models on the performance of walls with two PCM integration approaches, microencapsulation and macroencapsulation. Further analyses were performed regarding the impact of microencapsulated PCM percentage on variation in hysteresis models' predictions. The material presented in this chapter is from the journal article; "*Hysteresis model predictions of thermal performance of hempcrete-based walls with phase change materials*" Journal of Building Engineering.

Chapter 7 presents the performance of the hysteresis models under different heating setpoints and compares their predictions in two hempcrete-PCM walls. The material presented in this chapter is from the journal and conference articles; "*Temperature Control to Improve Performance of Hempcrete-Phase Change Material Wall Assemblies in a Cold Climate*." Energies (MDPI), and "*Improvement of the hempcrete-phase change material wall performance during the heating season using temperature control strategies*," Proceedings of eSim 2022:12th Conference of IBPSA-Canada.

Finally, **Chapter 8** presents conclusions from different chapters, limitations, and recommendations for further research.

2. Literature review

2.1. Energy consumption in buildings

2.1.1. General background

Buildings consume approximately 32-40% of the global energy demand and produce nearly 30% of energy-related carbon dioxide (CO_2) emissions worldwide [39-43]. Hence, the sustainable design of existing and future buildings is essential to increase energy efficiency and carbon neutrality of buildings in the efforts to encounter climate change and global warming [44]. As a result, building energy codes and regulations are becoming more stringent worldwide, and higher requirements for the energy performance of buildings in return have prompted the emergence of new technologies that can decrease the energy consumption of buildings and achieve the decarbonization process while maintaining the required thermal comfort [12, 45].

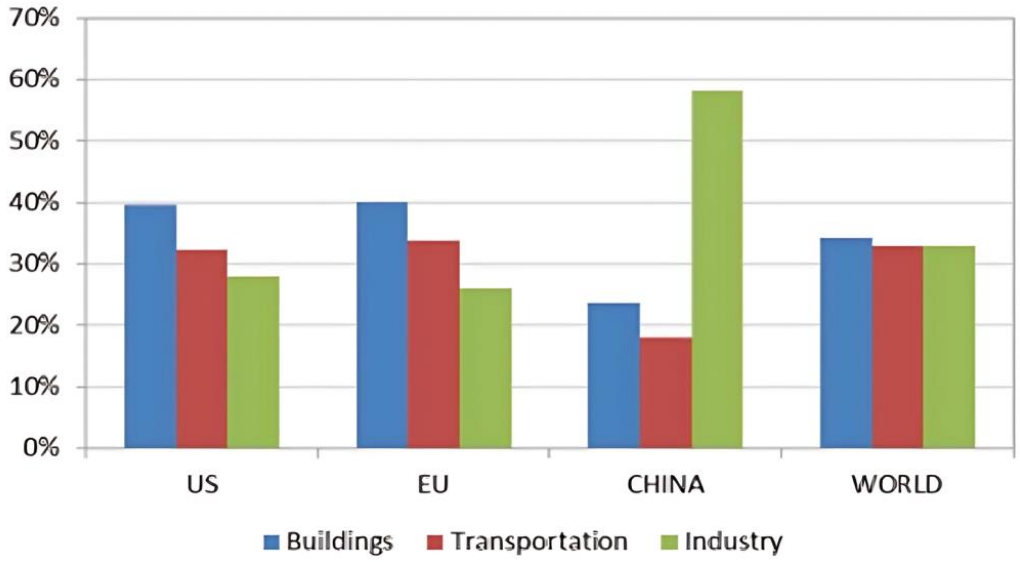

Figure 2.1. Global energy consumption sectors [43].

In Canada, buildings were responsible for around 28.8% of the energy used in 2018 (16.7% residential, 12.1% commercial/institutional), with space heating accounting for the most significant portion of the energy consumed in both types: 53%-64% [46]. In this respect, Canada

has pledged in the Paris Agreement to cut its greenhouse emissions by 30% from 2005 levels by 2030 [47]. As such, energy in buildings is one of the critical components to meet this goal, as it is responsible for about 22.2% of energy-related greenhouse gas emissions in Canada [46].

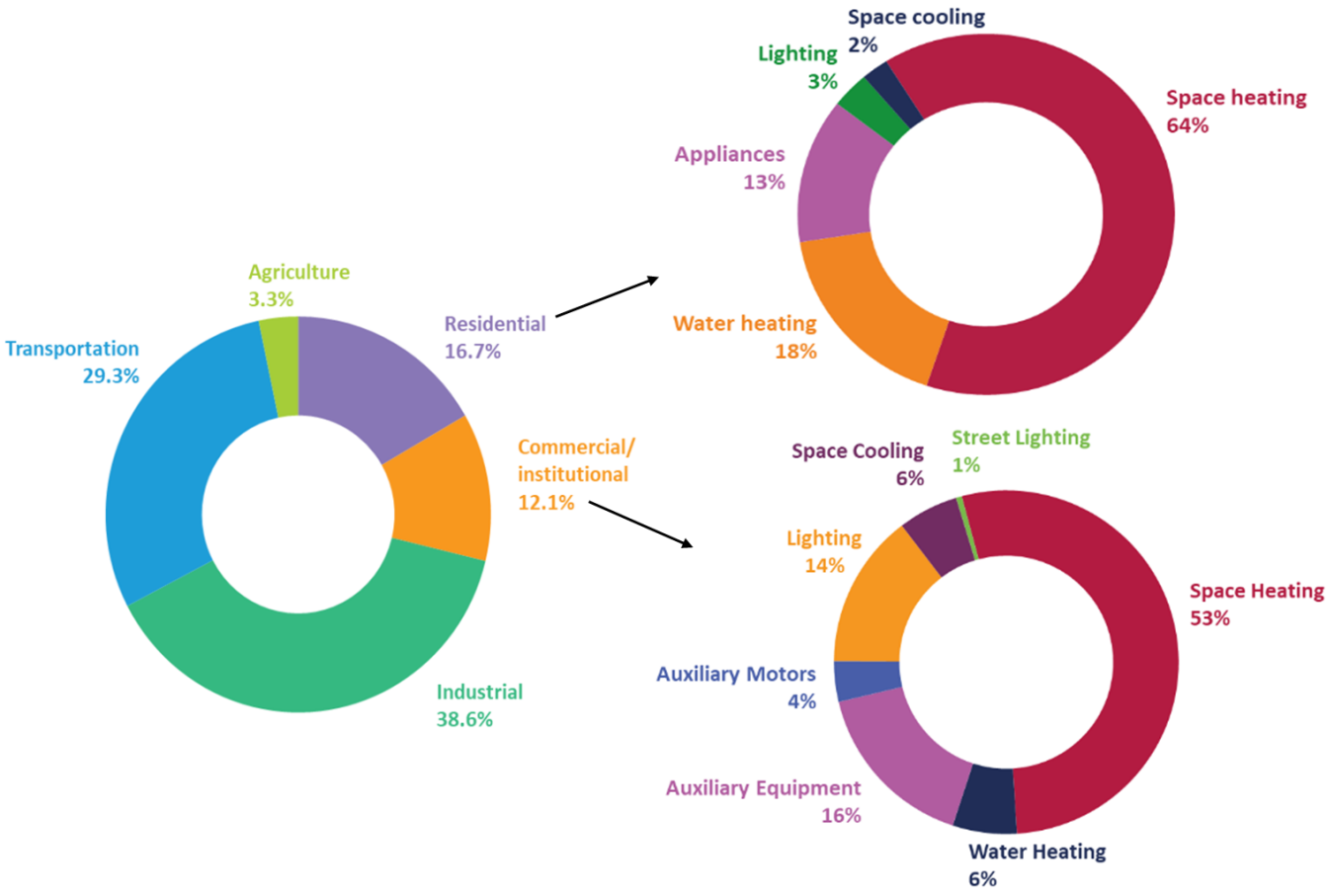

Figure 2.2. Energy use by sector 2018 [46].

2.1.2. Buildings envelopes

Active and passive strategies are two main techniques for improving building energy efficiency [48]. In active optimization strategies, the energy consumption in buildings is controlled by using mechanical or electrical devices in which fossil or renewable energy is used, such as HVAC systems and electrical lighting [49]. On the other hand, passive optimization strategies influence energy consumption in buildings by exploiting the potential of the building's envelope and

environment cost-effectively without using mechanical or electrical devices [7]. Incorporating efficient passive technologies into building envelopes can improve energy efficiency and thermal comfort and reduce the active systems' energy (downsize HVAC systems) while tackling environmental issues [50, 51]. In this framework, the energy performance of the building envelope plays a key role: indeed, the envelope is a physical barrier that separates the transient external weather and the internally conditioned space, keeping the residents comfortable, and as such, it highly impacts building energy consumption [52].

The efficiency of the building envelope depends mainly on its geometrical, physical, optical, and thermal properties, which affect indoor thermal comfort and energy consumption [53]. The thermal properties are mainly characterized by thermal insulation and thermal mass. In this research, the main focus was on thermal properties and thermal energy storage. The primary heat loss from building envelopes comes from heat transfer through the external walls, roofs, and windows. Hence, a proper design for the envelope's thermal resistance and thermal mass can improve the envelope’s energy efficiency [54].

Suitable insulation material should have low thermal conductivity to reduce the rate of heat flow into the building by conduction. At the same time, thermal mass reduces energy consumption because of the material's ability to store energy and release it later. However, the analysis, modelling, and research on the thermal mass effect on building envelopes are far more complex than the thermal resistance [55]. The likely reason is the nature of transient behaviour related to the thermal mass compared to the steady-state behaviour related to the thermal resistance [55]. In addition, the thermal resistance of an envelope is well-defined and understood with either a length-independent measure (thermal conductivity) or length-dependent measure (U-value), while the dynamic behaviour in thermal mass lacks such unified parameters [55]. Furthermore, the high

thermal mass can be a hindrance if misused, increasing energy consumption rather than decreasing it [55, 56]. As such, thoroughly considering a wide range of factors is necessary when designing the thermal mass of envelopes, such as inner and outer temperature profiles and envelope wall construction [55].

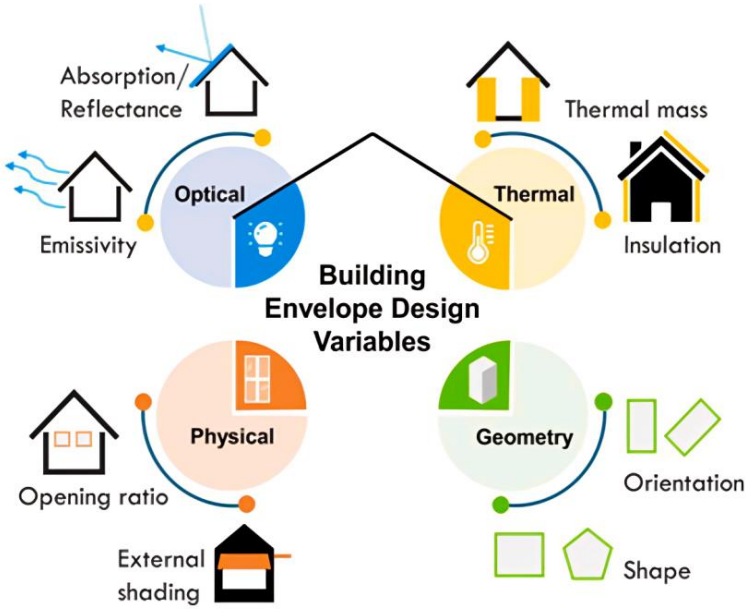

Figure 2.3. Building envelope design variables [53].

2.2. Phase change materials integration in building envelopes

2.2.1. General classifications

Thermal energy storage (TES) is considered one of the essential and effective strategies in energy-saving technologies for sustainable buildings, which can improve building energy efficiency and decrease the buildings' environmental footprint [57, 58]. For example, using TES to increase the thermal inertia of the building envelope walls can decrease energy consumption and indoor temperature fluctuations while maintaining thermal comfort [54]. Thermal energy storage systems can be classified into sensible systems (by changing the temperature of a material with high

specific heat capacity) [59], latent systems (by changing the phase of a material in a narrow temperature range) [60], and thermochemical reactions [61].

The sensible storage systems have the lowest energy density compared to the latent and thermochemical systems. Consequently, the conventional materials for sensible storage systems (i.e., brick, stone, masonry, concrete) may imply having a large size to increase the thermal mass of the building envelope efficiently enough to compensate for the limited allowable temperature ranges in the buildings [62].

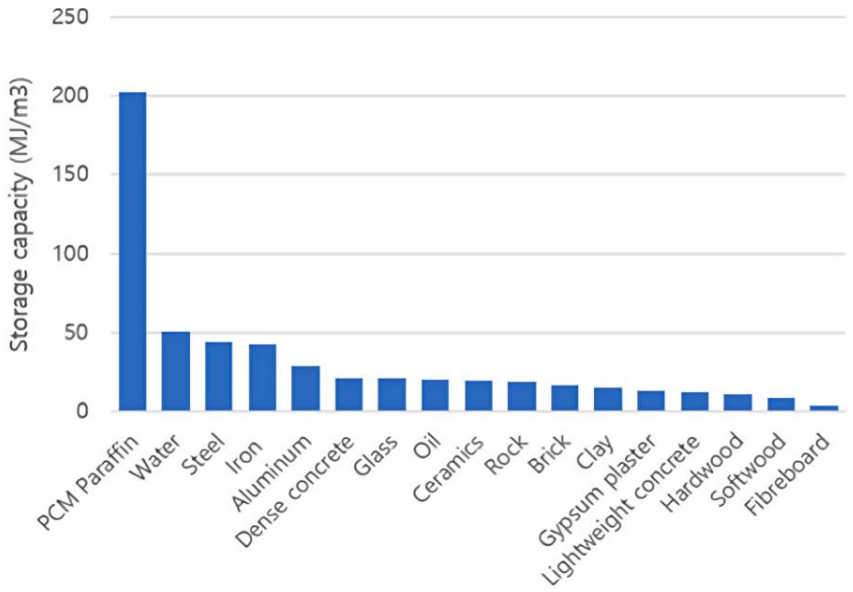

Figure 2.4. Storage capacity of materials used in building applications [63].

The latent heat storage systems with phase change materials (PCM) are capable of storing and releasing significant quantities of thermal energy per unit volume (i.e., ~5–14 times more than sensible storage materials [10]) through a change of phase from liquid to solid and back in a narrow temperature range [64-66], which makes it more suitable and practical for passive building envelope optimization techniques [61, 67]. Furthermore, the latent heat storage systems can cover various temperatures and applications by different PCM types according to the proper selection of

the phase change temperature over which the latent heat is charged/discharged. For instance, PCMs in building applications with suitable temperature ranges enable better control of indoor temperatures and significantly reduce energy demand by absorbing part of a building's heat load during the daytime while melting and discharging this stored heat during the nighttime by solidification [22, 65, 68]. Although the energy storage of most thermochemical reaction systems is denser than that of the latent heat of PCMs, the technical complexity and high cost make this storage technique not applicable or suitable for passive applications in buildings [15].

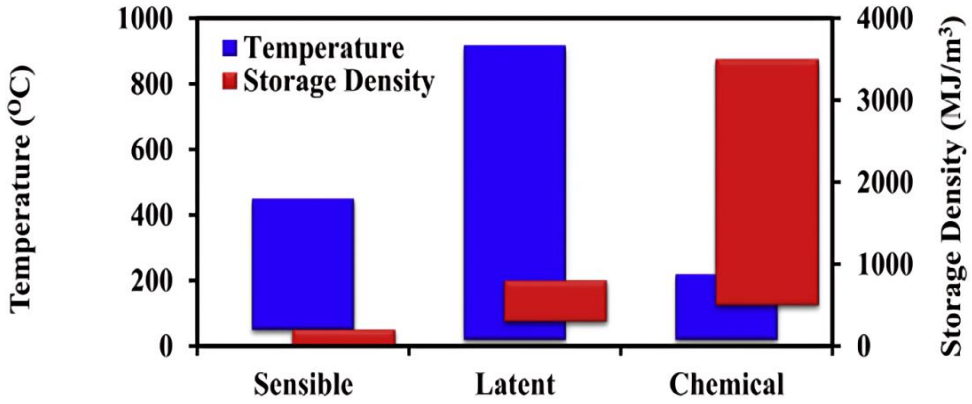

Figure 2.5. Storage capabilities of thermal energy storage systems [69].

2.2.2. PCM classifications and applicability for buildings

Phase change materials have three main categories: organic, inorganic, and eutectic compounds [70]. The selection of PCM categories related to their application in buildings should follow desirable criteria such as thermodynamic properties (high latent heat and specific heat capacity, proper phase change temperature, appropriate thermal conductivity), kinetic properties (little or no supercooling (high nucleation rate)), chemical properties (chemical stability after repeated cycles, no corrosion, no toxicity, no flammability), and economic properties (availability, cost-effectiveness, recyclability) [15, 71].

The organic PCMs have more suitable properties for PCM application in buildings, such as no or little supercooling, no phase segregation, non-corrosive, non-reactivity, no toxicity, small volume changes, good chemical stability, good reliability, no phase separation after numerous thermal cycling, recyclability, high compatibility with building materials and encapsulation materials, wide availability and cost-effectiveness [15, 70, 72-74]. However, non-paraffin PCMs show higher corrosion, flammability properties, and cost than Paraffin PCMs [75].

On the other hand, the inorganic PCMs have some limitations that hinder their broad applicability in buildings, such as problematic supercooling, phase segregation, corrosion, low thermal stability, higher toxicity, low reliability after thermal cycling, less compatibility with encapsulation materials compared to organic PCMs, and the higher cost (especially metallics) [70, 72, 73]. The properties of the eutectic PCMs are mainly derived from their constituents [76]. Although the eutectic mixture can be controlled to increase and mix the advantages and reduce the disadvantages of the final product, supercooling still exists, strong odor exists, insufficient combinations have been studied (fewer data available), and higher cost [70, 74].

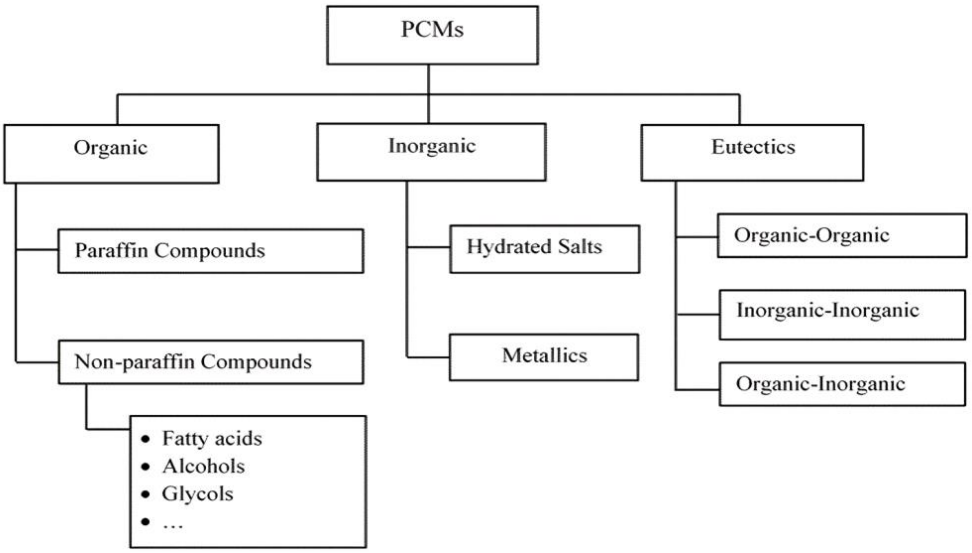

Figure 2.6. Classification of PCM [15].

However, some disadvantages of the organic PCMs need to be solved for optimum application in buildings, such as low thermal conductivity [77], high flammability (especially non-paraffins) [70, 78], and higher possibility of leakage than inorganic PCMs due to their lower density [63]. The leakage possibility and the thermal conductivity problem of PCM in passive systems can be overcome by microencapsulation, in which a very high surface area is obtained by encapsulating the PCM in a small shell, which improves the heat transfer properties (and fins or adding high conductive particles in active PCM storage systems) [77]. Flammability can be overcome mainly by adding flame retardants and microencapsulation with suitable shell materials [79, 80]. Microencapsulating the PCM, on the one hand, isolates the bulk PCM from the matrix material, which prevents or delays any possible reaction. On the other hand, a shell material with low flammability properties adds another layer of protection [78, 79]. However, this method allows direct mixing and spreading of PCM particles throughout the construction materials' thickness, which can affect the mechanical performance of the mixture by increasing the number of PCM microcapsules [81-83]. For example, a reduction is observed in compressive strength of 7% for each 5% increase in microencapsulated PCM (by weight of cement) in a self-compacting concrete mix [84]. Thus, there must be a limit to the percentage of microcapsules that can be added to the construction materials.

2.2.3. PCM integration in buildings

PCMs can be incorporated in buildings in either active or passive energy storage systems. In active storage systems, PCM can be integrated with HVAC systems or contained in heat storage containers [85]. Active PCM systems require some auxiliary equipment (mechanical or electrical) for their operation (PCM charging/discharging), which is why they are preferred when precise control of the system is needed [15]. For example, the active PCM applications allow the PCM to

charge and discharge energy on demand, which results in a more efficient control to lower energy consumption in a building, but with the penalty of extra technical complexity and higher cost [15]. In passive applications, PCMs are typically embedded into the building envelope fabrics of walls, floors, and roofs without relying on auxiliary equipment, which increases the envelope's thermal inertia and can help in a significant reduction of the size of the active system needed for indoor comfort [15, 64]. However, in passive systems, the charging/discharging process in the PCM is initially affected by temperature fluctuations in the environment (weather conditions and comfort schedules) [86].

In this respect, the performance of the PCM in passive applications is highly affected by uncontrollable external weather conditions, which is a critical factor in deciding the suitable PCM temperature required for the optimum melting/freezing process. In addition, the PCM performance varies drastically between seasons. For example, although the PCM selected for winter can operate in the phase change temperature range, which improves the thermal performance of the wall, the PCM may no longer experience phase changes in the summer season (PCMs remain in liquid state all the time), resulting in lower performance for the PCM wall compared to the traditional wall (and vice versa) [87]. Hence, using multiple PCMs with different temperatures is proposed due to the seasonality feature [88].

On the other hand, PCMs can't provide significant benefits in severe weather conditions or climates having minimum daily temperature variation [15]. The likely reason is that the PCM remains longer in the fully solid or fully liquid states and not in the partially liquid state (transition state), where the PCMs show their best performance [12, 89]. Thus, some researchers suggest that the variation in diurnal ambient temperature should exceed 10 K for effective storage in passive systems [90]. In addition, it is suggested that the PCM thermal conductivity should be high enough

to promote the heat transfer throughout the PCM to exploit the storage capacity and avoid phase segregation of the PCM (a non-uniform phase change within the PCM volume leading to the formation of coexisting solid and liquid regions) [91]. However, increasing the effective thermal conductivity of the wall reduces the thermal resistance and increases the heat flow through the wall, increasing energy consumption. Thus, careful optimization is needed in the design stage of PCM wall systems. For instance, the proper integration method of PCM can help mitigate such problems, including microencapsulation, in which the thermal resistance of a building wall can be increased without decreasing the benefit of using high thermal mass materials.

Moreover, the design of passive PCM systems needs special consideration in cold climates. Although insulation with low thermal conductivities (high thermal resistance) is the most common passive way of improving envelopes' energy performance as it can drastically decrease the energy load in buildings, the risk of moisture condensation in these walls may arise, especially in cold climates, which contributes to microbial growth inside walls and reduces the wall life [90]. The condensation phenomenon occurs in envelopes with high thermal insulation when the moist air temperature decreases to or below the dew point temperature by the walls' cold surface temperatures, resulting in moisture condensation [92]. Increasing the envelope wall's thermal mass may help mitigate the effect of condensation due to low thermal conductivities. Therefore, the thermal mass and resistance must be carefully designed when selecting building envelope materials.

Moreover, the research about the high thermal mass envelopes in hot climates likely agrees with the high thermal mass's effectiveness and benefits in reducing cooling energy consumption. However, high thermal mass in cold climates can increase heating energy consumption if the PCM is not designed and appropriately selected [55]. For example, a high thermal mass wall could mean

extra heat is needed to heat and raise the wall's temperature, which may increase the net heating energy consumption [55]. Hence, a careful design for the PCM temperature and amount is essential to eliminate or minimize any adverse effects in cold climates.

2.2.4. PCM passive integration methods

One significant barrier to expanding the use of PCMs is their relatively high initial cost [15]. Therefore, the efficient and cost-effective application of PCMs requires optimal integration into the building envelope, considering their thermal properties and the complex phase change behaviour. Many research studies investigated different techniques for the passive integration of the PCMs into building materials, such as direct methods (direct wet mixing, immersion) and indirect methods (shape stabilisation, and encapsulation) [12, 93, 94].

The direct incorporation method involves adding the PCM to the building materials, such as wallboard or concrete, during production [93]. The immersion method includes dipping a porous building material into PCM while letting the PCM permeate the pores in the material with the capillary property [64]. Although direct incorporation and immersion provide the advantages of low cost and simplicity, they have considerable drawbacks, such as easy leakage problems during the melting phase, incompatibility and chemical reactions with the base materials (affecting the hydration process), low thermal and chemical stability, and negatively affecting the mechanical properties and durability of the building material [74, 95].

The shape stabilization method includes mixing PCMs with high-density support material (porous materials or polymers) at high temperatures followed by cooling until forming the solid mixture, which has the advantage of shape stability and appropriate thermal conductivity [93]. This technique has the advantages of no need for containers, high thermal and chemical stability, and good interaction between PCM and supporting materials [61]. However, this method has some

limitations, such as the PCM absorption rate (where the nature of the support material dominates), the limit in the amount of PCM that can be contained (i.e., reduction in latent heat), leakage problem affecting the mechanical properties, more contact between the PCM and its surroundings leading sometimes to corrosion or not desirable reactions, and still needs more research to study their properties in-depth [61, 63, 96].

The encapsulation of the PCM before integrating it into the composite walls was proposed to address these limitations. For instance, containing the core PCM in compatible shell materials (with the PCM and the building material) prevents the leakage problem in the PCM liquid state, prevents any reactions between the core PCM and the matrix material, provides better thermal and chemical stability, and enhances heat transfer by increasing the surface area [74]. Consequently, encapsulation techniques (i.e., microencapsulation, macroencapsulation) are the most common methods for integrating PCMs into building envelopes [12, 65, 94], which allows efficient and cost-effective integration with construction materials [70].

The macroencapsulation technique hermetically encapsulates the PCM into a container such as tubes, panels, and spheres [12, 45, 97]. This approach provides application flexibility (the encapsulation materials, shapes, and sizes can be adjusted to meet different specific requirements [98]) and can prevent the direct mixing of PCM with the base building materials to avoid decreasing the mechanical performance [12, 97]. However, the low thermal conductivity of PCMs and the solidification at corners and edges (especially in large thicknesses) can reduce the heat transfer efficiency of the PCM [61]. The microencapsulation technology involves hermetically enclosing the PCM into small shell containers (1 µm-1 mm), further increasing the heat transfer area [12, 71]. However, the higher cost and the negative effect on mechanical properties pose a control on the amount that should be used [61].

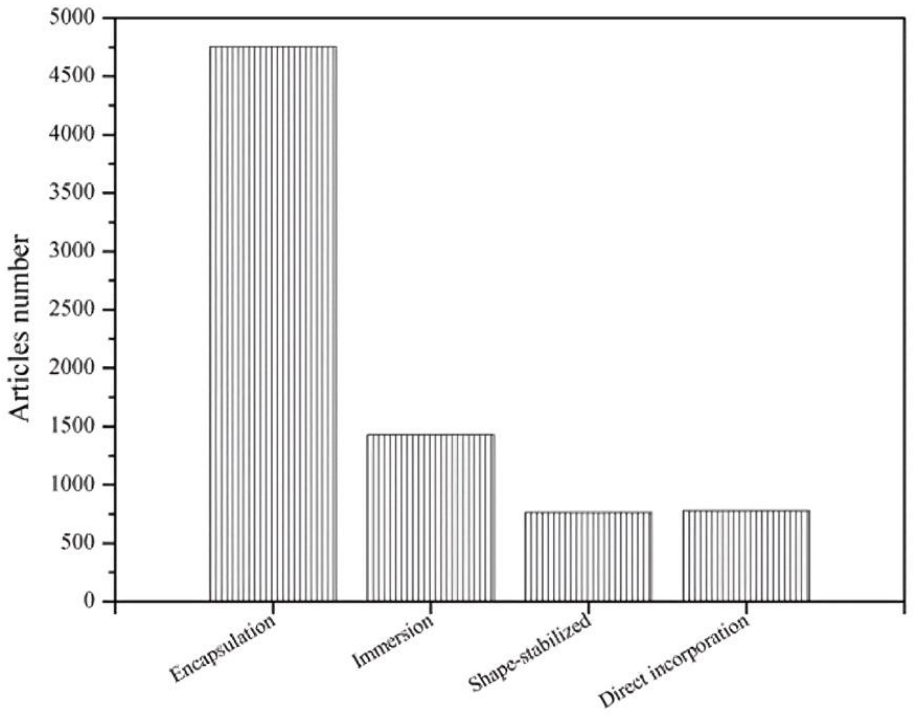

Figure 2.7. PCM incorporation techniques [12].

2.2.5. PCM modelling and hysteresis

Furthermore, PCMs are complex materials that require accurate modelling for optimal, fully effective integration [18]. In addition, previous studies concluded that a realistic numerical representation of the hysteresis phenomenon is crucial for performance analysis of PCM-enhanced envelope systems [99, 100]. For instance, the hysteresis phenomenon, which involves a delay in the start of the solidification process of the PCM, resulting in two different phase change curves for melting and freezing with different temperature ranges, is one of the most critical factors in affecting the heat transfer behavior and energy accumulation of the PCMs [16, 101]. Consequently, the hysteresis phenomenon creates additional difficulty in the modelling process since the thermal performance of the PCM is significantly affected by the history of heat loading. In addition, the incomplete (partial) phase change, which occurs when the melting process is interrupted during the phase change and followed by the freezing process (or vice versa), adds more complexity to

the hysteresis modelling process [16, 17]. Therefore, neglecting to model the hysteresis effect accurately accompanied by the partial phase change processes can give wrong predictions about the energy savings from the passive application of PCMs into the building envelopes [102].

Even though a realistic simulation of the hysteresis phenomenon is essential, only a few software tools can simulate it with different limitations and degrees of accuracy. For example, the widely used numerical simulation tools, such as ANSYS Fluent and COMSOL, by default utilise a simplified PCM model that neglects the hysteresis effect in the interrupted phase change processes, and the transition between the curves only occurs for the complete phase change cycles (the so-called Track model) [17]. Thus, the Track model behaves like a no-hysteresis case in interrupted phase change processes and accounts for the change in liquid fraction but on the same phase change curve (i.e., there is no transition between phase change curves) [103, 104]. Consequently, compared to the experimental observations, the Track model shows significant differences in PCM behaviour during hysteresis with partial phase change processes [105]. The example below shows that the Track model predicts wide fluctuations in PCM liquid fractions occurring only on the melting curve with no transition or accounting for the hysteresis.

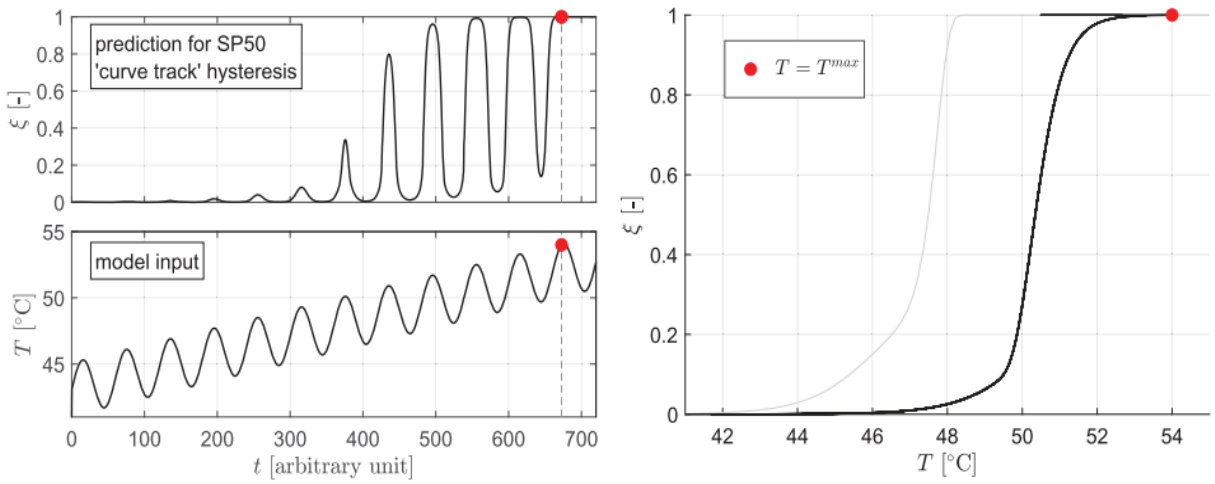

Figure 2.8. Predicted PCM performance with the Track model [17].

Furthermore, one of the widely used whole-building simulation tools, EnergyPlus, can model the hysteresis in partial phase change processes using a sensible enthalpy-temperature line approach (the so-called Switch model) to account for the transition between phase change curves [19]. The transition process in the Switch model follows a constant liquid fraction path, assuming that the PCM thermal storage remains only sensible during the transition between the phase change curves. As a result, the simulation predictions of PCM charge and discharge do not correspond to real-life behaviour. As shown in the example below, the Switch model predicts lower liquid fraction fluctuations compared to the Track model, with transitions between the melting and freezing curve to account for hysteresis but with constant liquid fractions (i.e., assuming sensible storage characteristics).

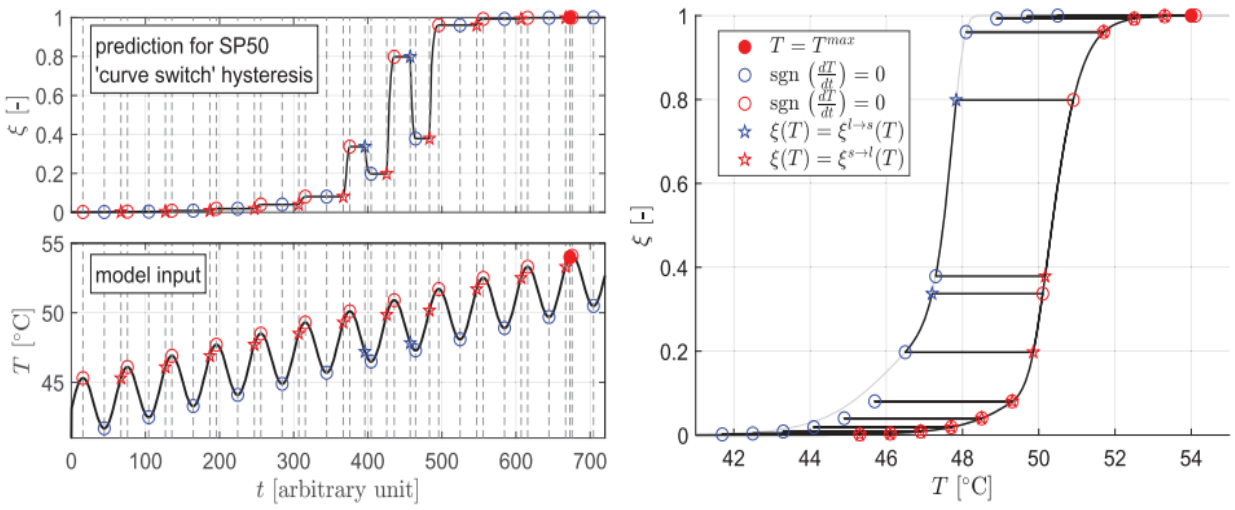

Figure 2.9. Predicted PCM performance with the Switch model [17].

A slight improvement was introduced to the Switch model by creating the transition paths using mathematical scaling of the melting and freezing curves (the so-called Scale model). However, the generated transition paths still partially follow a constant liquid fraction line, with a similar drawback as the Switch model [17, 106]. As shown in the example below, the Scale model predicts slightly wider liquid fraction fluctuations than the Switch model and is lower than that of the Track

model, as large portions of the transition paths follow a constant liquid fraction path like the Switch model. Overall, it can be concluded that those mentioned above widely used models confidence is insufficient to predict the real-life performance of PCMs in buildings since they introduce too simplified assumptions to realistically describe the PCM complex behaviour needed for accurate predictions [107].

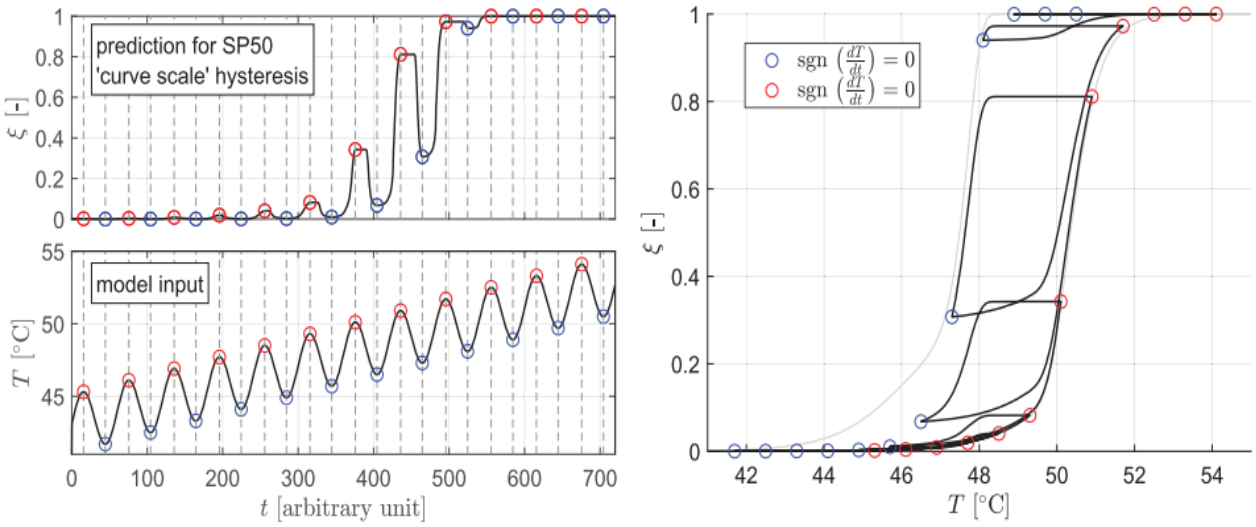

Figure 2.10. Predicted PCM performance with the Scale model [17].

2.3. Bio-composites as building materials

2.3.1. General background about hempcrete

Sustainable materials in energy-efficient constructions should provide and maintain indoor comfort with the lowest possible energy consumption (operational) and environmental footprint (embodied). Hence, the sustainability of a material can be assessed by different parameters such as embodied energy, embodied carbon emissions, circularity potential (reusability and recyclability), durability, and the ability to create comfortable indoor conditions with minimum energy consumption. Meanwhile, conventional building materials utilised for integration with PCMs (e.g., gypsum, concrete) often contain high embodied energy [24, 83]. Bio-composite

materials, typically made of mineral binder and bio-aggregate particles such as hemp or flax, can reduce the embodied energy of the built environment through cost-effective manufacturing and recycling processes [25].

In this respect, hempcrete is a promising lightweight carbon-negative bio-composite material manufactured from the inner woody core of the hemp plant mixed with a lime-based binder and water that holds the potential to considerably improve energy and indoor environmental performance and sustainability of buildings [29, 108, 109]. Typically, hempcrete composites are non-structural materials incorporated into load-bearing frames for low and medium-rise buildings to offer beneficial hygrothermal properties and enable passive indoor environment control [110-112]. Hempcrete walls can also meet building code requirements and allow simplifications of timber-frame constructions [113], especially knowing that using ordinary Portland cement mortars in these types of constructions results in the retention of moisture, hence, the deterioration of timber frames and has a more considerable ecological impact compared to hempcrete [33, 114]. In addition, applying hempcrete with timber frame walls can reduce thermal bridges due to their close values of thermal conductivities [33].

Overall, it can be stated that hempcrete has excellent potential in the suggested decarbonization strategies for buildings [44]. For example, in the embodied strategies, hempcrete is recyclable, reusable, biodegradable, and can be produced in prefabricated blocks, which is advantageous in large-scale projects. On the other hand, in operational strategies, due to its favorable thermal properties (thermal conductivity combined with specific heat capacity), hempcrete can help in efficient passive design for building envelopes and downsizing the active system needed for indoor comfort. Moreover, hempcrete is a carbon-negative material due to its carbon sequestration processes (i.e., more CO_2 is absorbed than emitted during production and use) [115]. For example,

hempcrete has a high CO_2 sequestration rate during two phases: the hemp's growing phase through photosynthesis (~1.5–2.1 $kgCO_2/kg$) and the lime binder carbonization phase over the building's life cycle, which solidifies the lime back into limestone by absorbing CO_2 [115]. Hence, it is estimated that the sequestered CO_2 by hempcrete can compensate for the embodied carbon in the production of lime and even result in negative levels of embodied carbon [116]. For example, numerous studies investigated the embodied carbon of hemp-lime composites, and all are common in reporting negative values in the range between (-0.3 and -1.0 $kgCO_2/kg$) [115-120].

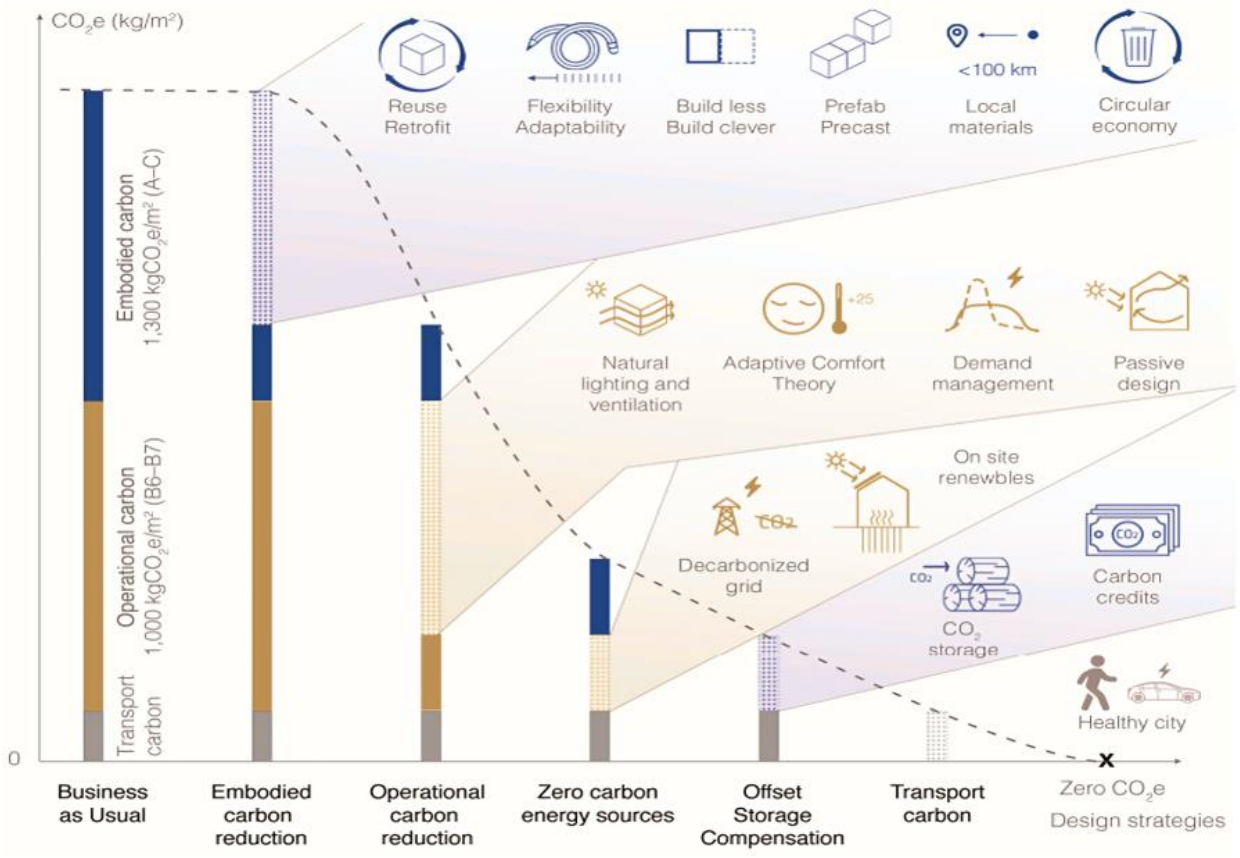

Figure 2.11. Decarbonization strategies for embodied and operational carbon are suggested for net-zero carbon buildings [44].

Nevertheless, the utilization of hempcrete in the construction industry remains low, mainly due to the high variability of hemp-lime composites and the lack of formulas that use widely available

and locally sourced ingredients. For example, hempcrete's production cost and embodied energy could be considerably higher in Canada than in Europe due to imported materials [113]. The use of innovative binders and a better understanding of the material's performance are indispensable steps for addressing hempcrete underutilization.

2.3.2. The main properties of hempcrete

2.3.2.1. Density

Hempcrete is a lightweight material with a wide density range (~200-1000) kg/m^3, which is lower compared to standard concrete (~2400 kg/m^3) because the density of hemp shives (as an aggregate) is lower than the corresponding density of the concrete aggregates [26]. Many factors affect hempcrete's density, resulting in significant density variations, such as the hemp/binder ratio, binder composition, the compaction level of the mixture, and water content [26]. Moreover, the hempcrete density directly affects the thermal conductivity [121] and the mechanical properties of the final mixture [26, 122]. Understanding the effect of these factors is essential to deciding the final density required for specific building applications (roof, wall, floor).

For example, a hemp/binder ratio of 1:1 can result in a low dry density of ~220 kg/m^3, which is suitable for loose-fill insulation applications due to its low thermal conductivity [121, 123]. In addition, a hemp/binder ratio of 1:2 can achieve a high dry density range of (531-627) kg/m^3, which can be helpful where slightly higher mechanical properties are needed [124]. In addition, the higher degree of compaction has also been proven to increase the dry density and the corresponding mechanical properties [25, 125]. Moreover, the humidity content trapped in the hempcrete samples affects the density of the samples, though to a minor degree [25]. The following sections provide further details on the effect of density on thermal and mechanical properties.

2.3.2.2. Thermal properties

Previous studies have shown that hempcrete thermal conductivity depends on factors such as sample density, binder/hemp ratio, mix, compaction level, and moisture content [25, 31, 126, 127]. In this regard, a positive linear correlation exists between hempcrete's density and thermal conductivity (i.e., increasing the density increases the thermal conductivity) [121, 124]. For example, Cerezo (2005) generated the linear correlation between the dry density and thermal conductivity of hempcrete ($k = 0.0002\rho + 0.0194$) [121]. Other researchers also reported similar trends. The direction of the compaction, compared to the heat flux direction, also has a direct effect on the measured thermal conductivity. For example, studies have shown that the perpendicular compaction direction results in higher thermal conductivity than the parallel compaction layering [128].

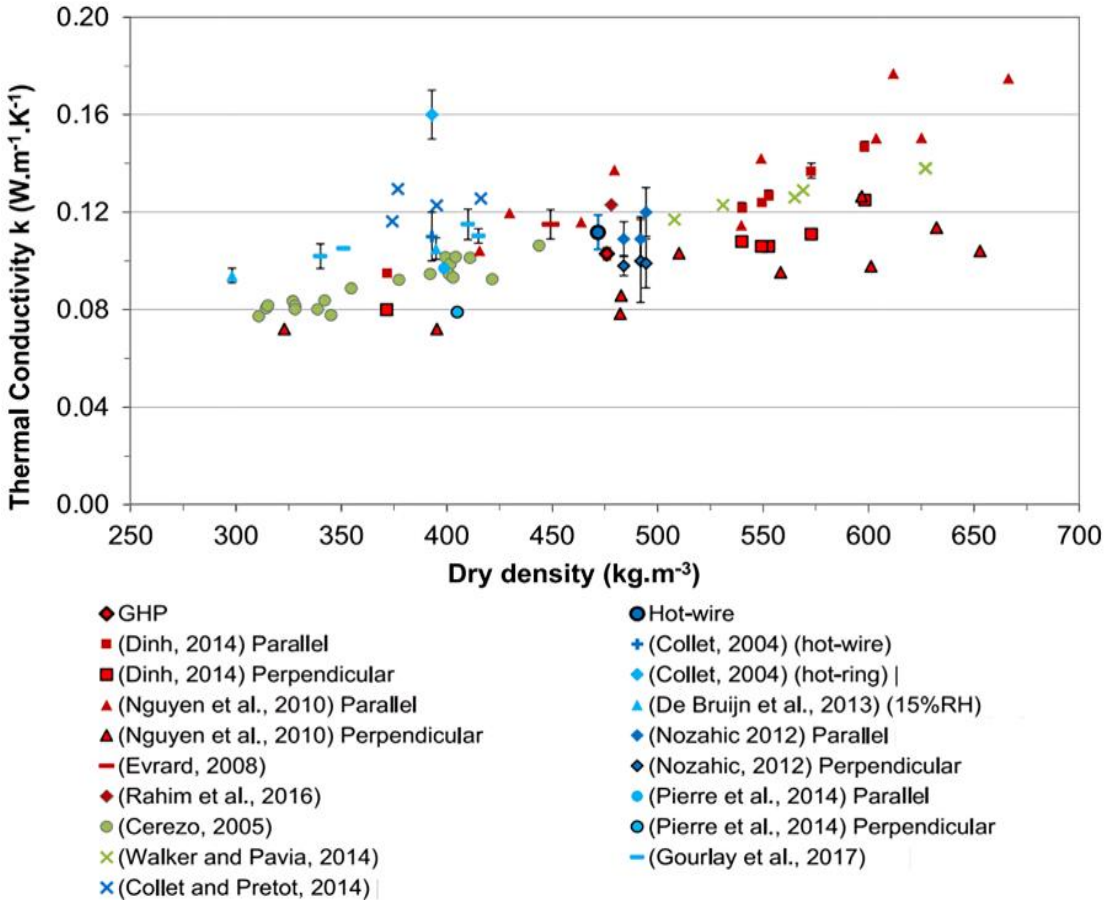

Figure 2.12. Thermal conductivity relation with dry density [129].

On the other hand, an increase in the proportion of porous hemp hurd in the hempcrete mix is desirable as it reduces the dry density and, hence, the thermal conductivity [126, 130]. However, a higher hemp amount may also lead to a lower specific heat capacity of the hempcrete mixture, lowering its ability to absorb and store thermal energy [36]. The binder amount also affects thermal conductivity because it has the highest thermal conductivity component in the hempcrete mix [121]. Thus, studies have reported thermal conductivity in the range of 0.06-0.11 W/m K for hempcrete mixtures with low and medium dry densities ranging from 200 to 400 kg/m^3, and hemp/binder ratios of 1:1, 1:1.5, and 1:2 [123, 131]. In comparison, hempcrete samples with higher dry density in the 450-800 kg/m^3 range and higher hemp/binder ratio of 1:2-1:4 had higher thermal conductivity ranging from 0.12 to 0.18 W/m K [123, 131]. Furthermore, an increase in humidity

content tends to increase the thermal conductivity of the hempcrete mixes. For example, Rahim et al. (2016) reported a rise in thermal conductivity of approximately 8% and 16% at 10°C and 40°C, respectively, due to an increase in the water content of 0.08 kg/kg from the dry state [132]. Collet & Pretot (2014) also proved that thermal conductivity can increase by around 15-20%, increasing from the dry state to the 90% RH state [110].

Hempcrete is also characterized by high specific heat capacity values, even higher than concrete and brick [133]. Thus, specific heat capacity in the 1000-1590 J/kg K range was reported for hempcrete with dry densities ranging from 381 to 627 kg/m³ and hemp to binder ratio of 1:2 [31, 124]. It is also proven that humidity levels significantly affect specific heat values. For example, it has been reported that a specific heat capacity of around 1500 J/kg K was obtained in a dry state, while a specific heat capacity of around 2900 J/kg K was obtained at 99% relative humidity [25]. The variation in specific heat capacity under different humidity conditions has an opposite effect compared to the variation in thermal conductivity [130]. For instance, high humidity conditions increase hempcrete's effective density and specific heat capacity, which is a favourable feature to increasing thermal inertia. It also increases the thermal conductivity, which may result in higher heat losses from the walls. However, studies show that the high specific heat capacity can provide a better effective thermal performance than hempcrete's thermal transmittance suggested based on the static U-value calculations [25, 29].

However, the density of hempcrete composites is much lower than that of concrete and bricks, resulting in lower volumetric heat capacity than concrete and brick [133, 134]. Thus, an improvement in the thermal mass of hempcrete composites is needed without a significant increase in thermal conductivity. As such, hempcrete integration with other innovative materials, such as PCMs, can modify its thermal energy storage properties [135].

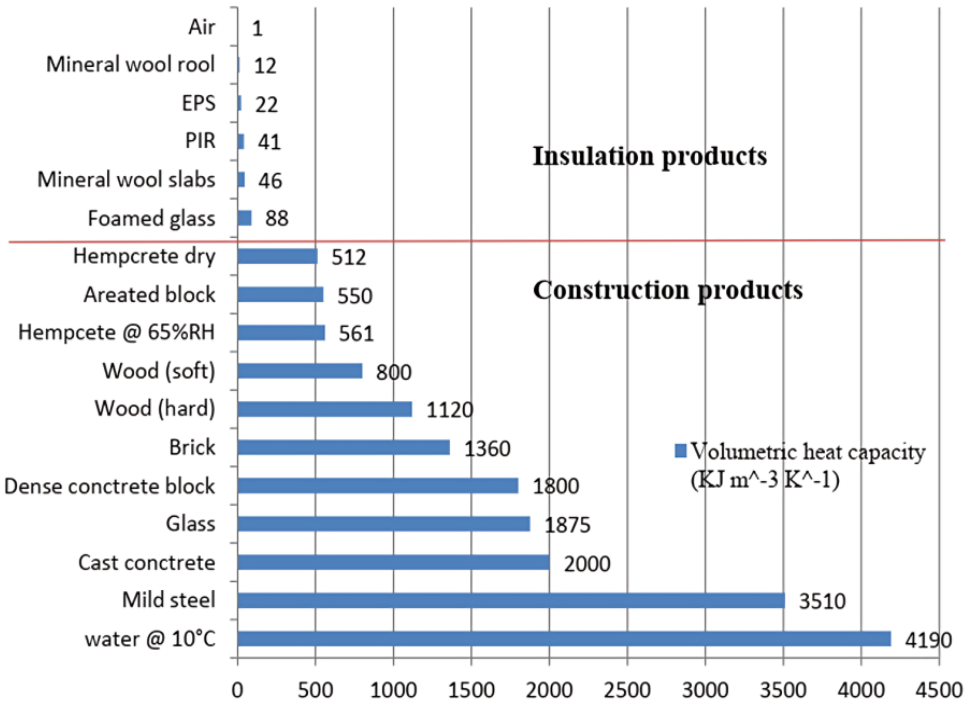

Figure 2.13. Volumetric heat capacity for hemp and other common building materials [134].

2.3.2.3. Mechanical properties

Hempcrete has lower compressive strength than concrete and can't be used as a load-bearing material. However, hempcrete still plays an essential structural role in conventional timber wall or double-stud framing as it can prevent the bending or buckling of the studs under loaded conditions [25, 136]. For example, Mukherjee and MacDougall (2013) reported that 313 kg/m^3 hempcrete infill supported 3-4 times the compressive loading of a standard timber stud wall [136].

Overall, the compressive strength of hempcrete depends on various factors such as the binder type, the hemp/binder ratio, the water/binder ratio, and the sample density [25]. The typical value of the compressive strength of hempcrete mixes is between 0.2-1.15 MPa [121, 137]. However, higher values could be obtained with either conventional cementitious binders (18 MPa) [138] or non-conventional binders such as MgO-cementitious binders (1.86-6.94 MPa) [139]. In addition, the hemp/binder ratio has a detrimental effect on the compressive strength, as such a high content of

hurd (i.e., low binder content) in the design mix reduces the compressive strength [30, 121]. For example, when Murphy et al. (2010) studied the compressive strength of hempcrete made from commercial binder (Tradical binder (TH)) and hydrated calcic lime (CL90s), it was observed that increasing the hurd content reduced the final compressive strength, although with a different rate according to the binder type [138].

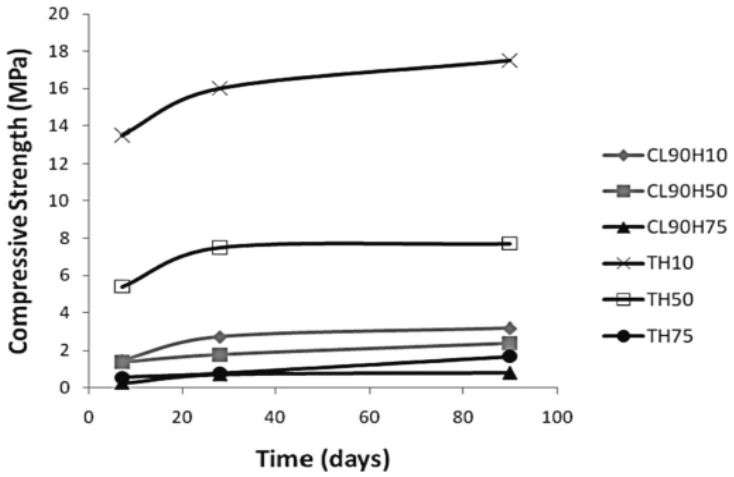

Figure 2.14. Compressive strength of hempcrete composites. (H10 = 10% hemp, H50 = 50% hemp, H75 = 75% hemp) [138].

However, an increase in the density through compaction of the hempcrete can enhance its mechanical characteristics while reducing the binder's quantity, which is the major contributor to embodied carbon [125, 137, 140]. In this respect, Dinh (2014) reported approximately 15% higher compressive strength of a 556.0 kg/m^3 hempcrete sample than a 439.7 kg/m^3 sample with a compressive strength of 0.65 ± 0.06 MPa [126]. However, the methods to increase the compressive strength of hempcrete harm the thermal conductivity. For example, the compressive strength of hempcrete can be increased by increasing the binder content (reducing hemp content) and increasing the mixture density by compaction. However, the thermal conductivity also increased, resulting in lower thermal resistance [125].

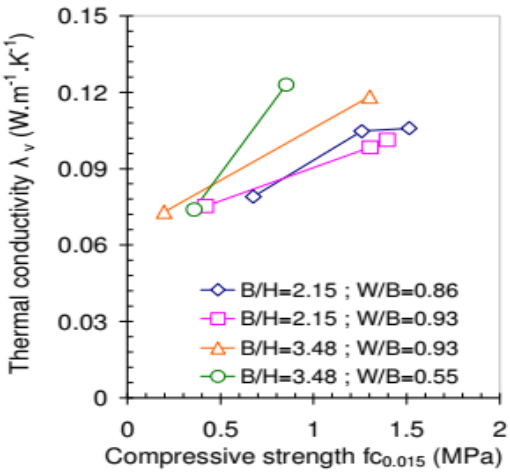

Figure 2.15. The relation between compressive strength and thermal conductivity at different compositions [125].

The typical flexural and splitting tensile strength values are in the range of 0.06-1.3 MPa and 0.02-0.15 MPa, respectively [121, 137]. Likewise, the hempcrete mixes' flexural and splitting tensile strength increased with density [137]. For instance, Elfordy et al. (2008) reported flexural strength in the range of 0.749-1.209 MPa, with a 2:1 binder-to-hemp ratio and a high-density range of 430-607 kg/m^3 [137]. A high content of hemp hurd in the design mix reduces the flexural strength of hemp-lime composites [30, 121]. In addition, Murphy et al. (2010) studied the flexural strength of hempcrete with different hemp/binder ratios and binder types and observed that the flexural strength increased with increasing the binder content (reducing hemp content). However, a further increase of binder content to 90% had no significant influence on flexural strength. In addition, they also reported that the samples with commercial binders had higher flexural strength values than those made with hydrated lime [138].

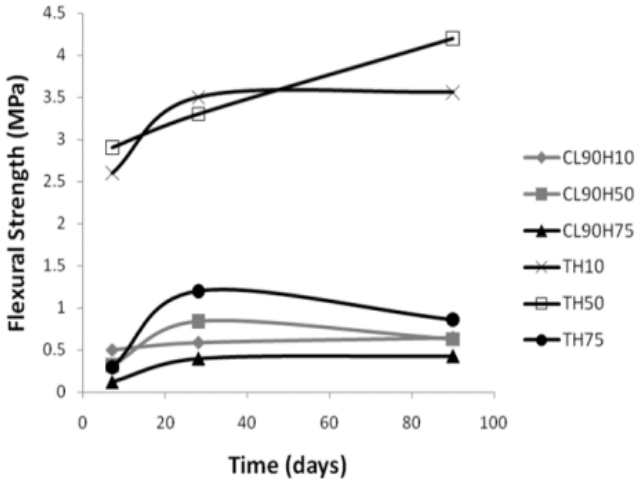

Figure 2.16. flexural strength of hempcrete composites. (H10 = 10% hemp, H50 = 50% hemp, H75 = 75% hemp) [138].

2.3.2.4. Moisture regulation

Hempcrete is characterized by its excellent ability to regulate moisture and humidity due to its high moisture diffusion coefficient and water vapor permeability of approximately $2.3x10^{-11}$ kg/(Pa.m.s) [25]. In this regard, the high levels of permeability and moisture buffering values of hempcrete can result in high performance for indoor moisture regulation by absorbing the excess water vapour during high relative humidity times, and releasing it back during the low relative humidity of the surrounding, maintaining adequate comfort for occupants at all times [33]. Therefore, hempcrete's excellent hygroscopic qualities help, in addition to humidity regulating the internal environment, also to discourage condensation on interior surfaces, which contributes to healthy indoor air quality, buffering humidity levels and restricting the growth of potentially harmful moulds, other spores, and bacteria [33].

Hempcrete also has a high moisture buffering value (MBV) of around 2-3.47 g/(m^2%RH) or higher, which is better than concrete's MBV of 0.37±0.04 g/(m^2%RH) [32]. Moisture buffering values identify the material's ability to absorb or release moisture when exposed to repeatedly

varying levels of humidity [32], and the higher this value, the higher the material's ability to regulate the ambient relative humidity passively. Moreover, the MBV values reported for hempcrete in literature are characterized as an excellent moisture regulation performance per NORDTEST protocol, compared to conventional building materials [141]. For example, Latif et al. (2015) reported a moisture buffer value (MBV) of 3.47 gm/m^2%RH with a binder-to-hemp ratio of 1.2:1 and density of 290 kg/m^3 [32], while Collet et al. (2013) reported an MBV of 2.14 gm/m^2%RH, with a binder to hemp ratio of 2:1, and density of 430 kg/m^3 [142].

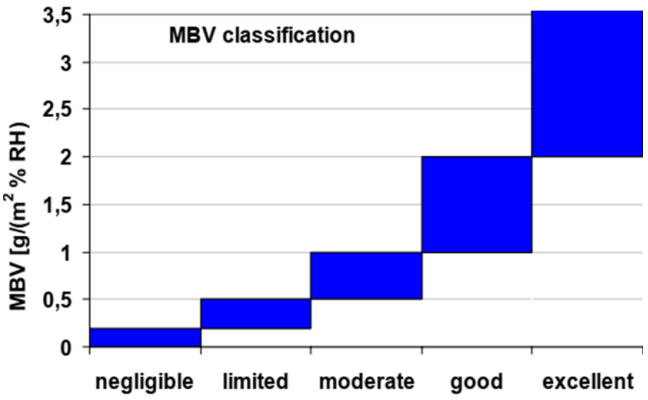

Figure 2.17. Classes of moisture buffering performance [141].

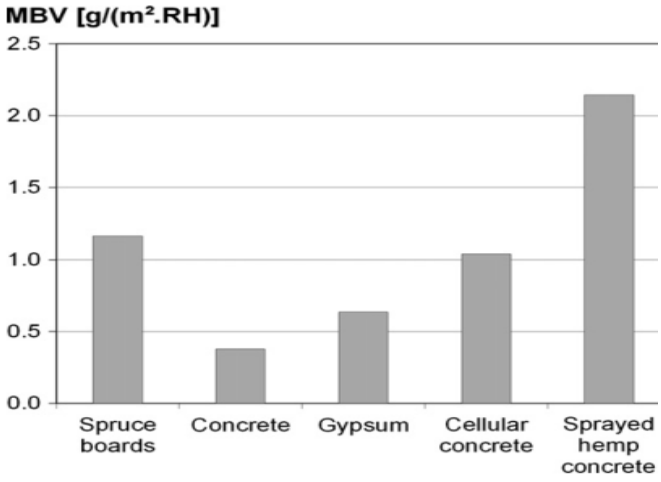

Figure 2.18. Moisture buffering values for selected building materials [141, 143].

2.4. Conclusions, research gap, and study plan

Although hempcrete is one of the promising lightweight materials that can be used in building envelopes for lower embodied and operational energy, no research has been done on its integration with energy storage materials to improve its thermal properties further. Integrating PCMs and hempcrete can result in the development of a bio-composite building material with improved thermophysical properties for the construction of sustainable buildings. To our knowledge, the only research study that focused on PCM integration with hemp-lime composites investigated its flammability [144, 145]. Therefore, this is the first study that provides the essential physical properties of hempcrete-PCM composites that govern their behaviour, including thermal conductivity, specific heat capacity, and hysteresis phenomena. Moreover, this is the first research focused on hempcrete-PCM enhanced wall assemblies' thermal storage and energy-saving capabilities.

This research also aims to develop innovative insulating hemp-lime composites made of recycled and locally sourced materials. To the best of the authors' knowledge, this is the first study that introduced recycled crushed brick as a pozzolan to hemp-lime composites to reduce their environmental impact further and improve thermal properties, which is also the same reason that this research focused on maximizing the hemp hurd ratio in the hempcrete mixtures.

Moreover, there is a gap related to accurate hysteresis modelling in interrupted phase change situations and comparing how different PCM integration methods perform under the different hysteresis models. This work aims to close the gap related to the realistic modelling of hysteresis in PCMs in four distinct ways. First, it introduces a new hysteresis simulation method named the Modified Scale (MScale) to simulate hysteresis in incomplete phase change processes. Second, it demonstrates the use of the new model in a finite volume commercial code (ANSYS Fluent) for

the first time: indeed, there is limited research on modelling PCM hysteresis accompanied by interrupted phase change processes using a finite volume technique [146]. Third, to the best of the authors' knowledge, this is the first study to investigate the hysteresis effect on two different PCM integration methods in walls, microencapsulation, and macroencapsulation, to compare the sensitivity of their thermal performance to the hysteresis models. Fourth, to investigate the impact of the microencapsulated PCM share in the hempcrete wall and the heating setpoint on the hysteresis model behaviour and the resultant thermal performance of the wall.

3. Research Methodology

3.1. Research Method Overview

Figure 3.1 shows the overview of the applied method, which consists of two phases: (1) Experimental analysis and (2) Numerical analysis. Phase one included developing and experimentally characterizing hempcrete and PCM-enhanced hempcrete composites. Phase two involved preliminary modelling of PCM-enhanced hempcrete walls, developing a hysteresis model for accurate simulation of PCMs, and numerically investigating heating setpoints effect on the performance of PCM-enhanced hempcrete wall assemblies in ANSYS Fluent. Each phase is further described on subsequent pages, while further details of the adopted methodology are provided in subsequent chapters.

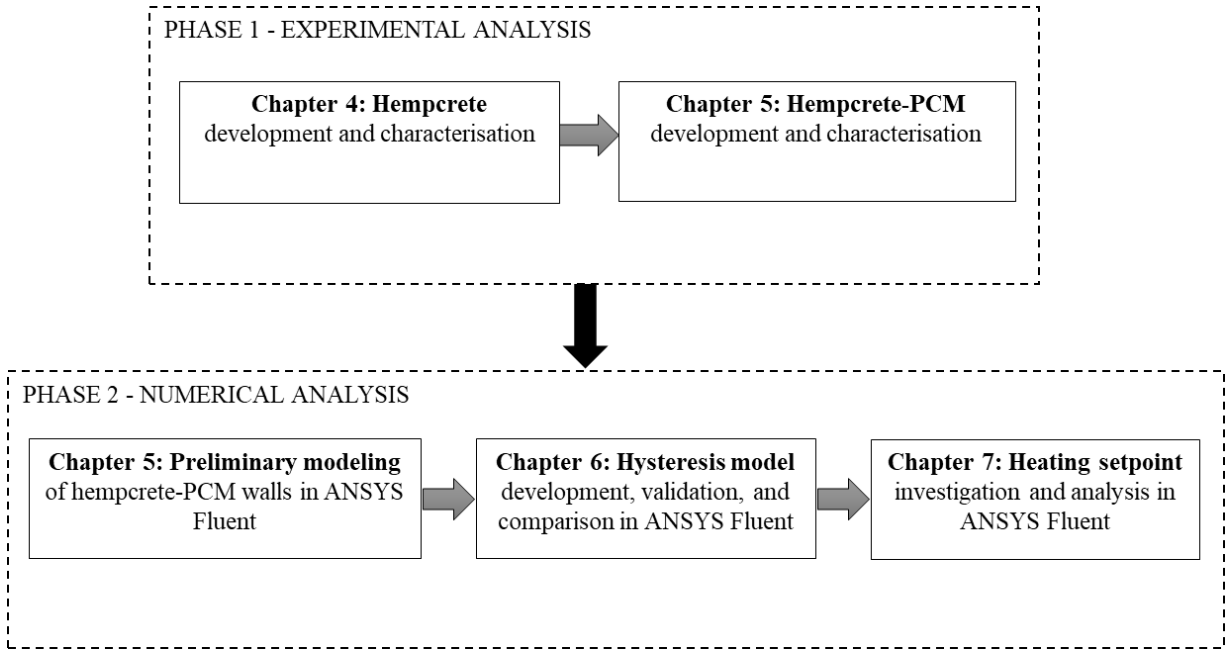

Figure 3.1. Overview of the adopted methodology.

3.2. Phase 1 (Chapter 4): Hempcrete production and characterisation

1. Hempcrete mix design development: Hemp hurd + Binder + Water

Hempcrete samples with locally sourced ingredients and suitable for wall insulation applications were created with different binder mix designs regarding the share of hydrated lime to one of two pozzolans (metakaolin or crushed brick) or a setting material (hydraulic lime), as presented in Figure 3.2.

Figure 3.2. Hempcrete ingredients of different mix designs.

2. Hempcrete characterisation: Hygrothermal and Mechanical tests

Thermal conductivity (W/m K) analysis according to ASTM C518–15 and Specific Heat Capacity (J/kg K) analysis according to ASTM C1784−14 were performed on 7 design mixes in a heat flow meter apparatus, as shown in Figure 3.3. Each mix was tested 2-3 times to ensure the reproducibility of the results.

Figure 3.3. Hempcrete samples and heat flow meter.

Moisture buffering capacity (gm/m² RH%) analysis according to the NORDTEST protocol was carried out on selected 3 design mixes in an environmental chamber, as shown in Figure 3.4. Tests were repeated 2 times to ensure reproducibility of the results.

Figure 3.4. Hempcrete samples for testing and chamber.

Compressive Strength tests (MPa) were performed on 14 design mixes and 56 cylindrical samples (four samples for each design mix) on the 90th day according to ASTM D 4832 using the INSTRON SATEC 300 DX series Universal Testing System, as shown in Figure 3.5. The approximate values for Young's modulus (MPa) were calculated from compression test results.

Figure 3.5. Hemcprete samples prepared for testing and universal testing system (UTS).

Splitting Tensile Strength tests (MPa) were Carried out on 14 design mixes and 28 cylindrical (two samples for each mix) samples on the 90th day according to ASTM C496 / C496M–17 using the INSTRON SATEC 300 DX series Universal Testing System, as shown in Figure 3.6.

Figure 3.6. Hemcprete sample and tensile test messurment uisng UTS.

3.3. Phase 1 (Chapter 5): Hempcrete-PCM production and characterisation

1. **Hempcrete-PCM mix design development**: Hemp + Binder + MPCM + Water.

Hempcrete-MPCM (HPCM) composites were created using: a) two microencapsulated PCM (MPCM) types (Nextek and Micronal DS) obtained from manufacturer (Microtek), b) four MPCM phase change temperatures (18±1 °C, 23±1 °C, 24±1 °C, 25±1 °C), and c) two MPCM concentrations in hempcrete (9% and 18% by weight). The binder mix design showed the best mechanical properties in hempcrete composed of hydrated lime (50%) and metakaolin (50%), as shown in Figure 3.7.

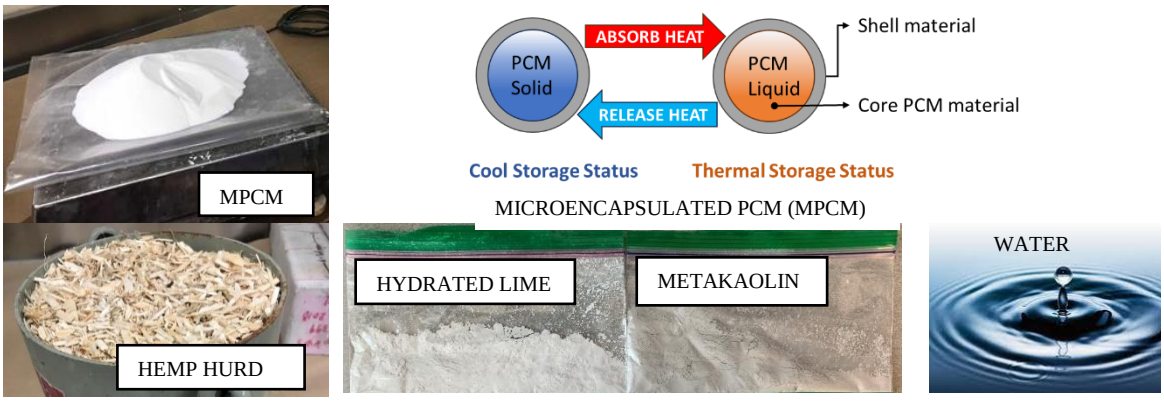

Figure 3.7. Ingredients of Hempcrete-PCM composites.

2. **Raw material characterisation:** SEM and Thermal conductivity

Scanning electron microscopy (SEM) enabled the investigation of the expected degree of MPCMs' shell damage and agglomeration, as shown in Figure 3.8 on the left. The transient line heat source technique with DECAGON KD2 Pro allowed measuring the thermal conductivity of MPCMs, as shown in Figure 3.8 on the right.

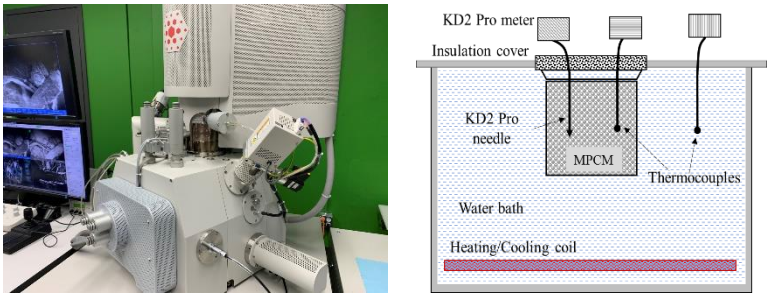

Figure 3.8. Scanning Electron Microscope: FEI Quanta 650 FEG and transient line heat source DECAGON KD2.

3. **Hempcrete-PCM characterization:** Thermal analysis

Eight HPCM samples were tested for thermal conductivity and specific heat capacity using the same standards and instruments used for hempcrete. Each mix is measured 2-3 times to ensure the reproducibility of the results.

3.4. Phase 2 (Chapter 5): Preliminary hempcrete-PCM wall modelling

The hempcrete and hempcrete-PCM (HPCM) models were developed in ANSYS Fluent to investigate the thermal performance (as shown in Figure 3.9) of 9% and 18% HPCM walls with 18 ^{0}C and 23 ^{0}C melting temperatures compared to hempcrete case. The phase change hours of hempcrete-PCM walls (at three layers inside the wall) and the thermal performance of hempcrete and hempcrete-PCM walls were analysed throughout the year.

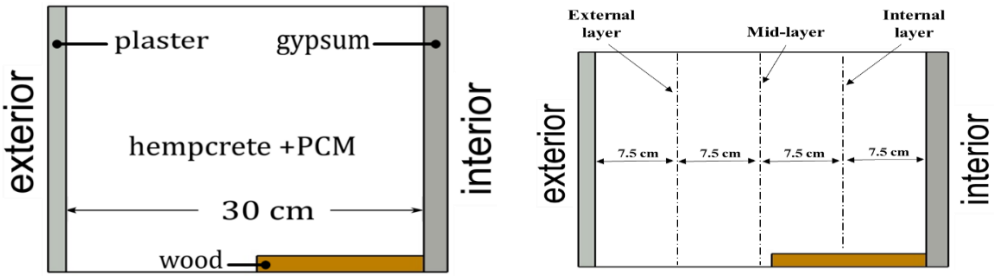

Figure 3.9. Wall geometry for numerical analysis.

3.5. Phase 2 (Chapter 6): Development of hysteresis model

A new hysteresis simulation model, Modified Scaled (MScale), which considers changing liquid fraction and transition between the melting and freezing curves to accurately capture the complex phase change phenomena observed in experimental studies, was developed in ANSYS Fluent. The MScale model's predictions were compared against experimental data and predictions of three widely used hysteresis methods, including Track, Switch, and Scale. The four models were evaluated using three test cases: (i) validation against experimental data, (ii) hysteresis model impact on the thermal performance of walls with PCM integrated via microencapsulation and panel (see Figure 3.10), and (iv) the effect of PCM percentage.

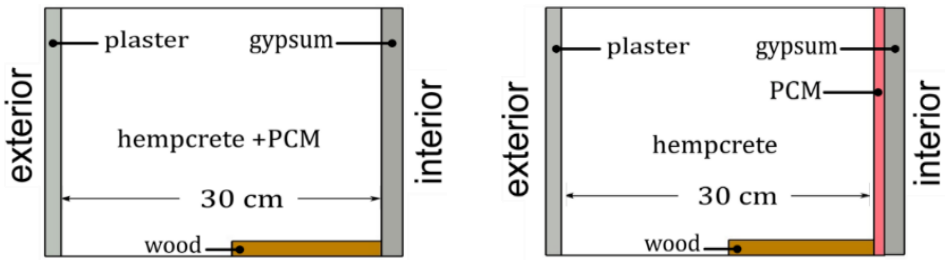

Microencapsulated Panel

Figure 3.10. Four hysteresis models and two wall designs.

3.6. Phase 2 (Chapter 7): heating setpoint analysis

The two hempcrete-PCM wall designs (Figure 3.10) were further investigated and simulated in ANSYS Fluent using three different heating setpoint schedules (SCH1, SCH2, SCH3). The wall's performances were analysed, and the predictions for the different hysteresis models were compared under the three schedules.

4. Chapter 4: Mechanical, Thermal, and Moisture Buffering Properties of Hempcrete

Hempcrete composites made of locally sourced ingredients and innovative binders with insulating properties for application in cold climates were developed and experimentally characterised regarding their mechanical, thermal, and moisture buffering properties. The results of this comprehensive experimental study were used to (1) develop hempcrete formulas from Canadian ingredients with excellent hygrothermal properties and (2) inform the selection of the hempcrete mix design for producing a new latent thermal storage material made of hempcrete and microencapsulated phase change material (PCM) for passive implementation in a building envelope. The chapter first describes the raw ingredients and composition of hempcrete samples. Then, it provides the methodology used to carry out the experimental analyses. After that, the chapter presents the results of the experiments, followed by the discussion. Finally, a summary of the findings is provided. This chapter is published in the journal article https://doi.org/10.3390/ma13215000 [111].

4.1. Material ingredients

4.1.1. Raw Materials

Local hemp producer "Plains Hemp" in Manitoba provided the hemp hurd used as aggregate in this study. The bulk density of the hurd at lab conditions (22 ◦C and 50% RH) was 110 ± 5 kg/m^3, whereas its dry density after oven drying at 105 ◦C for 24 hours was 101 ± 2 kg/m^3. Sieve analysis was performed on an oven-dried batch of 100 g, according to ASTM C136–06 [147], to determine the distribution of fine and coarse aggregates. Approximately 87% of the particles were less than 2.36 mm, whereas 10% were between 2.36 and 6.3 mm. The hydrated lime, metakaolin, and hydraulic lime used in this study complied with ASTM C207-06 [148], ASTM C618-12 [149],

and ASTM 1707-09 [150], respectively. In addition, recycled pozzolanic crushed brick was utilized.

4.1.2. Compositions of Hempcrete Samples

This study focused on maximizing the hemp hurd ratio within the hempcrete mixture to improve its thermal properties while reducing its environmental impact and price. Hence, the hemp hurd-to-binder ratio used in the hempcrete sample preparation was 1:1, with a density adequate for wall applications between 300 and 400 kg/m^3 [31, 151, 152].

The amount of water added to hemp-lime composites affects their physical properties. For instance, low water content may cause incomplete hydration and unreacted powder-form binder, reducing compressive strength [122, 153]. In contrast, high water content can result in much higher density, leading to increased thermal conductivity, issues with a setting for the lime binder, and excessively long drying times for the hempcrete [110, 126]. Therefore, we investigated different water contents that allowed the developed hempcrete mixes to be suitable for work. Table 4.1 summarizes the hempcrete design mixes with varying binders, pozzolan concentrations, and water contents.

Table 4.1. Composition of hempcrete samples.

Design mix	Name	Mix Ratio by mass Hemp/Lime/Pozzolan/Water *					
		H	L	CB	MK	NHL	Water
Hydrated Lime-Crushed Brick	LCB10	1	0.9	0.1	-	-	2.5
		1	0.9	0.1	-	-	3
	LCB20	1	0.8	0.2	-	-	2.5
		1	0.8	0.2	-	-	3
Hydrated Lime-Metakaolin	LMK20	1	0.8	-	0.2	-	2.5
		1	0.8	-	0.2	-	3
	LMK50	1	0.5	-	0.5	-	2.5
		1	0.5	-	0.5	-	3
	LMK70	1	0.3	-	0.7	-	2.5
		1	0.3	-	0.7	-	3
Hydrated Lime-Natural Hydraulic Lime	LNHL50	1	0.5	-	-	0.5	2.5
		1	0.5	-	-	0.5	3
	LNHL70	1	0.3	-	-	0.7	2.5
		1	0.3	-	-	0.7	3

*H- hemp hurd, L-hydrated lime, MK-metakaolin, NHL-natural hydraulic lime, CB- crushed brick.

4.1.3. Mixing, Moulding, and Curing

The first step in creating hempcrete samples was mixing the binders and water to create a slurry. Then, hemp hurd was added to the slurry and blended in an industrial mixer for approximately ~5 min until a uniform mixture was obtained. For the thermal properties and moisture buffering tests, rectangular wooden moulds (26 cm wide × 26 cm long × 5.5 cm high) were filled with the mixture and tamped until the desired wet density was reached. The cylindrical moulds (10 cm diameter × 20 cm long) for compression tests were prepared according to ASTM C39/C39M-12 [154]. Furthermore, for splitting tensile tests, the cylindrical moulds (15 cm diameter × 30 cm long) were produced following ASTM C496/C496M–17 [155]. Then, a one-quarter portion of the mould was filled with the mixture and tamped until the desired wet density was reached (i.e., 750-800 kg/m^3). The samples were demoulded after seven days and cured at a lab temperature of 22 ± 1 ◦C, with

RH ~50%, for another 21-28 days until they reached a constant mass. Approximately ~100 samples were tested for mechanical, thermal, and moisture buffering properties.

4.2. Experimental analyses

4.2.1. Mechanical tests

The compression and splitting tensile tests followed the ASTM D4832 [156] and ASTM C496 [155] standards, respectively. Both compressive and splitting tensile strengths were measured after 90 days. The load was applied continuously without any shock at a 5 mm/min rate and run for approximately 4-5 min per specimen. The failure mode was determined by the drop observed in the load-displacement curve after the initial increase. Four samples were tested for each design mix, and compressive strength was calculated as their average. Two samples for each design mix were tested for the splitting tensile test, and their averages were computed.

4.2.2. Thermal tests: Heat flow meter

A FOX 314 Heat Flow Meter Apparatus (HFMA) enabled measurements of the thermal conductivities of hempcrete samples. The apparatus has top and bottom plates equipped with heating and cooling systems to control the heat flux through the sample in between. Following the ASTM C518 standard for a steady-state test [157], the HFMA creates steady one-dimensional heat flux through the sample by setting both plates at constant but different temperatures with an accuracy of ± 0.03 °C. The HFMA is calibrated to convert transducers' voltage signals to heat fluxes using NIST 1450b SRM (Standard Reference Material of National Institute of Standards and Technology) [158]. As presented in Equation (4.1), the thermal conductivity is calculated by applying Fourier's Law of Heat Conduction with an accuracy of approximately ± 1% at the mean temperature of the plates, as reported by the manufacturer.

$$q'' = K\frac{\Delta T}{L} = SQ\left[\frac{\mathrm{W}}{m^2}\right] \qquad (4.1)$$

where ΔT is the temperature difference between upper and lower plates, S is the heat flow meter's calibration factor (W/(m^2 μV)), Q is its output signal (μV), L is the sample's thickness (m), and k is thermal conductivity (W/m K). The collected data from the apparatus consists of the upper and lower plate temperatures and the plates' transducer outputs, with each 512 successive data points organized in one block and averaged to get the mean plate temperatures and heat fluxes. The averaged values at one block are compared with the average values of the previous block to check for the thermal equilibrium criteria. The test at a specific setpoint is complete when a specified number of successive blocks satisfy two equilibrium criteria. First, the block average plate temperature must equal the earlier block average temperature within ± 0.2 °C. Second, the difference between the transducers' average signal outputs of two successive blocks must be within a typical value of 50 μV and 2% of the earlier block average.

The HFMA can be modified to measure the specific heat capacity of hempcrete. The dynamic test procedure described in ASTM C1784 [159] included the following process. The first step involved holding both HFMA plates at the same constant temperature until reaching a steady-state condition. Then, Equation (4.2), which assumes the transient heat conduction in the finite body for a significant time [160], allowed calculations of the specific heat capacity at each temperature setpoint.

$$C_p = \frac{k}{\rho L^2\, \pi^{-2}\left(\frac{\Delta \ln (Q_i)}{\Delta t}\right)} \qquad (4.2)$$

where L is sample thickness (m), ρ is density (kg/m^3), k is thermal conductivity (W/m K), and ($\Delta \ln Q_i/\Delta t$) is the slope of the curve of the natural logarithm of HFMA output values versus time. The uncertainty of specific heat from the dynamic test is calculated at each temperature setpoint using Equation (4.3) and is found to be approximately ± 2.5%.

$$U_{C_p} = \sqrt{\left(\frac{\partial C_p}{\partial k} U_k\right)^2 + \left(\frac{\partial C_p}{\partial \rho} U_\rho\right)^2 + \left(\frac{\partial C_p}{\partial L} U_L\right)^2 + \left(\frac{\partial C_p}{\partial (slope)} U_{Slope}\right)^2} \quad (4.3)$$

where U_k is uncertainty in conductivity (± 1%) provided by the manufacturer, U_ρ is uncertainty in density (± 1.75%), U_L is uncertainty in thickness (± 0.025 mm), U_{slope} is uncertainty in slope (± 0.4% with 95% confidence level).

4.2.3. Moisture Buffering Capacity Tests

According to the NORDTEST protocol [141], hempcrete's moisture buffering capacity measurements included sealing all specimens' sides except the upper surface (26 cm × 26 cm) exposed to humidity cycles in a climate chamber. The air temperature in the climate chamber was kept constant at 23 ± 1 ◦C, while the relative humidity (RH) was kept constant at 75 ± 2% for 8 hours and 33 ± 2% for 16 hours. Due to the importance of the initial conditions of the samples' moisture contents [161, 162], their effect was studied using two different initial states: high moisture content (75% RH) and low moisture content (33% RH). Each sample mass was measured using an electronic scale with an accuracy ± 0.01 gm to monitor the mass change during the uptake and release phases. The humidity cycles were repeated until the steady-state condition was reached, and the mass change in the cycles' uptake and release phases was less than 5% [141]. The moisture buffer value (MBV) was calculated as the average of the last three steady cycles, using Equation (4.4).

$$MBV = \frac{\Delta m}{A\ (\Delta RH\ \%)} \quad (4.4)$$

where Δm in the mass change (gm), A is the exposed surface area (m^2), and $\Delta RH\%$ is the difference between the high and low relative humidity.

4.3. Results

4.3.1. Distribution of sample density

Figure 4.1 shows the distribution of the density of all samples. The figure shows that approximately 88% of the specimens are within the 300 to 350 kg/m³ density range. The average density and standard deviation are 326 kg/m³ and 16 kg/m³ (~4.9%), respectively; the minimum is 291 kg/m³, and the maximum is 368 kg/m³. These results suggest consistency between the average densities of hempcrete samples produced in this study. Furthermore, Table 4.2 summarizes descriptive statistics of compression, tensile, and thermal samples. The samples prepared for compressive tests have the highest average density (~338 kg/m³), followed by the splitting tensile samples (~326 kg/m³) and thermal samples (~312 kg/m³). Similarly, the specimens created for the compressive tests exhibit the highest standard deviation of 15.8 kg/m^3 (~4.7%), followed by tensile specimens with a standard deviation of 7.7 kg/m^3 (~2.4%). Thermal samples share nearly similar standard deviations in density (~2.5%) for wet and dry tests.

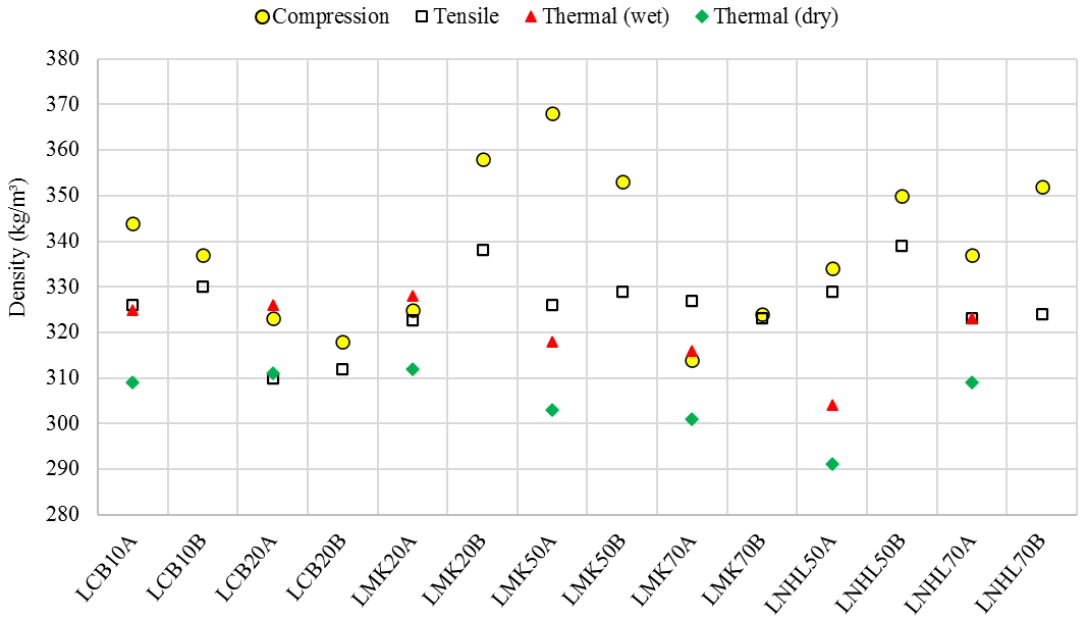

Figure 4.1. Average densities of all hempcrete samples.

Table 4.2. Descriptive statistics of samples.

Density (kg/m³)	Compression	Tensile	Thermal wet	Thermal dry
Minimum	314	310	304	291
Average	338	326	319	305
Maximum	368	339	328	312
Standard deviation	15.8	7.7	8.0	7.3

*Confidence intervals (for 95% confidence level).

4.3.2. Compression and splitting tensile results

Table 4.3 summarizes the average compressive strength, splitting tensile strength, and hempcrete samples' densities. The samples' average compressive strength is 0.33 MPa, with a standard deviation of 0.124 MPa (~38%), and it ranges from 0.15 MPa (LMK70A) to 0.57 MPa (LMK50B). Due to less variation in the samples' density for splitting tensile tests than compressive tests (see Table 4.2), tensile strength dispersion is slightly lower than compression values. Thus, all samples' average splitting tensile strength is 0.0239 MPa, with a standard deviation of 0.005062 MPa (21%), ranging from 0.016 MPa to 0.0348 MPa.

Table 4.3: Average compression strength, tensile strength, and density.

Design mix	Name		Density (kg/m³)	Compressive Strength (MPa)	Standard deviation (MPa)	Density (kg/m³)	Splitting Tensile Strength (MPa)
Hydrated Lime-Crushed Brick	LCB10	A	344	0.35	0.03	326	0.0244
		B	337	0.38	0.03	330	0.0249
	LCB20	A	323	0.20	0.02	310	0.0219
		B	318	0.24	0.02	312	0.0223
Hydrated Lime-Metakaolin	LMK20	A	325	0.21	0.02	323	0.0222
		B	358	0.33	0.05	338	0.0307
	LMK50	A	368	0.38	0.06	326	0.0181
		B	353	0.57	0.11	329	0.0219
	LMK70	A	314	0.15	0.01	327	0.0160
		B	324	0.19	0.01	323	0.0183
Hydrated Lime-Natural Hydraulic Lime	LNHL50	A	334	0.28	0.05	329	0.0307
		B	350	0.47	0.05	339	0.0348
	LNHL70	A	337	0.33	0.03	323	0.0260
		B	352	0.53	0.03	324	0.0229

*A is designated for water content (2.5). B is designated for water content (3).

Overall, an increase in hempcrete density leads to a rise in its compressive strength. These findings are consistent with the results of previous studies [125, 137]. Thus, the hempcrete samples of density ≥350 kg/m³ have a compressive strength range of (0.33-0.57 MPa), with an average of 0.46 MPa, and higher than the global average of ~39%. Meanwhile, the hempcrete samples of density <350 kg/m³ have a compressive strength range of (0.15-0.38 MPa), with an average of 0.26 MPa, and lower than the global average with ~21%, with the specimen of the lowest density LMK70A (314 kg/m³) having the lowest compressive strength of 0.15 MPa.

On the other hand, the relation between the samples' density and splitting tensile strength is less significant or observed than the density and compressive strength relation. Although the highest tensile strength of 0.0348 MPa for LNHL50B samples with the highest density of 339 kg/m³, the sample LMK70A with a density of 327 kg/m³ (not the least compacted sample) has the lowest

splitting tensile strength of 0.016 MPa, and the lowest density samples LCB20A (310 kg/m³) has a splitting tensile strength of 0.0219 MPa (close to the global average).

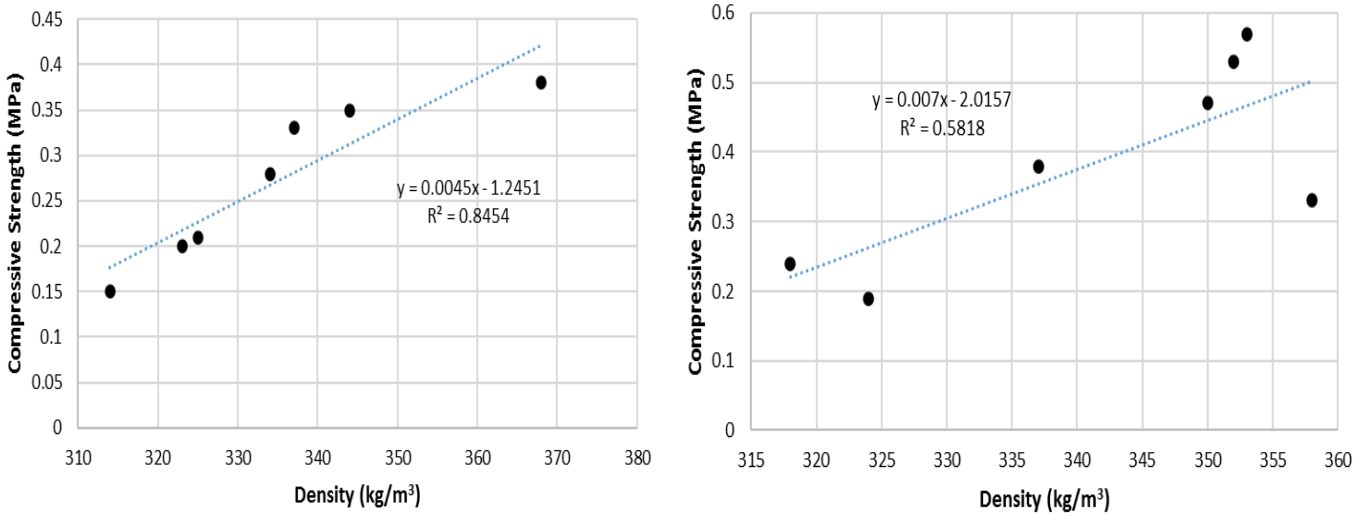

a) Water content (2.5). b) Water content (3).

Figure 4.2. Compressive strength and density for different water contents.

Figure 4.2 shows the relation between compressive strength and density at the two water contents. The figure shows that the relation is better (higher R^2) at the lower water content. For example, in the lower water content case, the compressive strength of all samples can be ranked by their densities. In contrast, in the higher water content case, the samples with the highest compressive strengths, LMK50B and LNHL70B, are not the most compacted, and the least compacted sample (LCB20B) is not the lowest compressive strength. Hence, these results suggest that water content, binder type, and content significantly impact hempcretes' mechanical properties.

Furthermore, an increase in the percent of MK and CB, above a certain amount, is shown to reduce the compressive strength of hempcrete. This effect is most pronounced in LMK samples in which compressive strength decreases by (~61-67%) with an increase in the percent of MK from 50% to 70%. Similarly, the compressive strength decreases by (~37-43%) with an increase in the percent of CB from 10% to 20%. In contrast, the compressive strength increases by (~13-18%) with an increase in the percentage of NHL from 50% to 70%. On the one hand, these results support Dinh's

(2014) findings regarding the adverse effect of an increase in MK share above 70% on the compressive strength of hempcrete [126]. On the other hand, Eires et al. (2006) stated that 75% of metakaolin and 25% of lime were the best binder mix [163]. However, they also reported that this design mix requires higher curing temperatures to increase strength gain. In addition, an increase in the percent share of MK, CB, and NHL hurts the tensile strength of hempcrete. For example, an increase in the percentage of MK from 50% to 70% results in ~12-16% decrease in hempcrete tensile strength. An increase in NHL from 50% to 70% decreases the tensile strength by approximately ~16-34%, whereas an increase in the crushed brick from 10% to 20% exhibits the lowest decrease in the tensile strength of only ~10%.

Additionally, the increase in the water content increases the compressive strength even of the samples with lower densities. For example, the sample LCB20A with 323 kg/m³ density has a compressive strength of 0.20 MPa, while the sample LCB20B with 318 kg/m³ density has a higher compressive strength of 0.24 MPa, with the same trend can be observed in LMK50 and LCB10 samples. On the other hand, the design mixes with smaller water content show inferior compressive and tensile strengths compared with the higher water content specimens. These results echo Walker and Pavia's (2014) observations about the hemp's high suction ability that undermined the binder's hydration and adversely affected the strength of hemp-lime composites [122]. The LMK70 samples show the most unreacted binder and the lowest compressive and splitting tensile strengths. Meanwhile, the sample LNHL50A shows an average compressive strength of only 0.28 MPa and approximately 68% higher (0.47 MPa) for the LNHL50B with higher water content.

Similarly, the LNHL70A sample exhibits an average compressive strength of 0.33 MPa, around 38% lower than the LNHL70B sample with higher water content. Likewise, increasing water content increases the tensile strength of the samples. For example, the highest tensile strength

sample, LNHL50, showed a ~13% increase in strength with increased water content. The lowest tensile strength sample, LMK70, showed a ~14% increase in strength with increased water content.

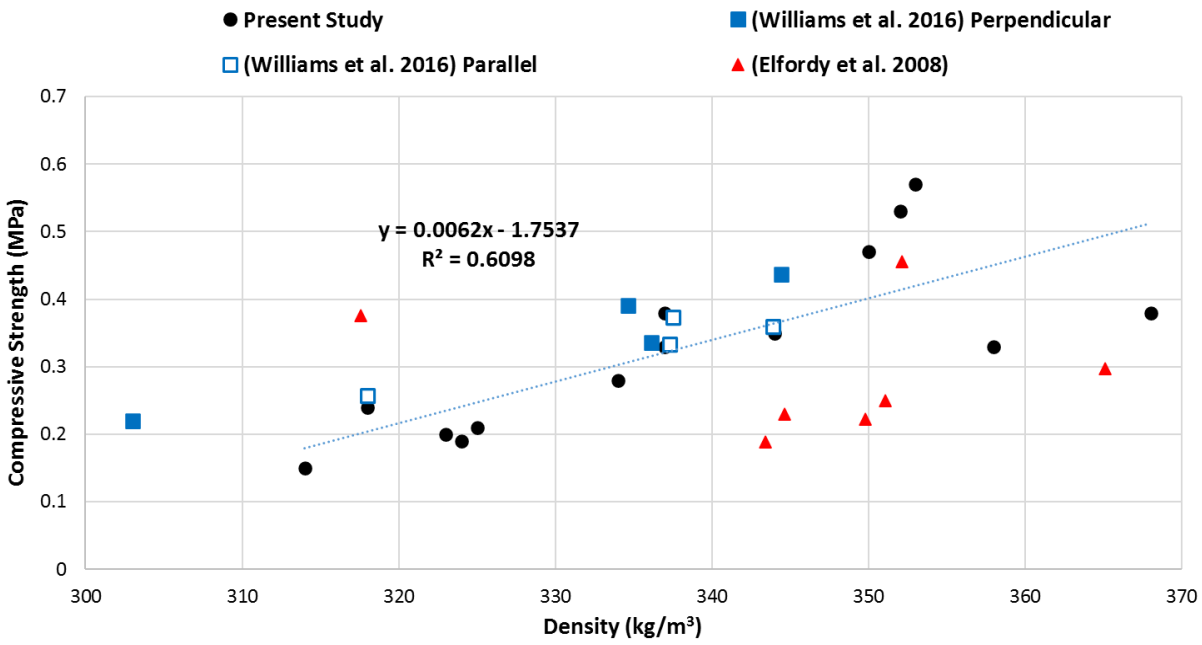

Figure 4.3. Compressive strength and density, with other studies.

Figure 4.3 compares the density and compressive strength among the developed samples against previous studies with similar hempcrete densities [128, 137]. The results show a relatively good agreement between the present study and the values reported in the literature for samples in the same range of densities, even though a different binder-to-hemp ratio was used. In this regard, Elfordy et al. (2008) [137] and Williams et al. (2017) [128] used a 2:1 and 2.25:1 binder-to-hemp ratio, respectively. Hence, maximizing the hemp ratio in this study was compensated by the compaction level enough to produce final densities in the required range. This result further agrees with the reported observation that increasing compaction increases the density and the compressive strength and may allow reducing the binder amount [125, 138]. Also, it is essential to note that some studies differentiate between testing in perpendicular (⊥) and parallel (∥) directions to the direction of compaction. In this respect, Williams et al. (2017) reported comparable compressive

strengths of the similarly dense samples between the two methods (the perpendicular showed a very slight increase above the parallel) [128]. Hence, although the compaction and testing directions were designed to present the worst-case scenario for mechanical properties (parallel) in this research, the ranges obtained still agree with the reported values. In addition, many other studies reported compressive strengths and density ranges that agree and intersect with values in Table 4.3, such as Walker et al. 2014 (0.29-0.39 MPa / 360-400 kg/m^3) [122], Cérézo 2005 (0.25-1.15 MPa / 250-600 kg/m^3) [121], and Hirst et al. 2010 (0.2-1.2 MPa / 220-342 kg/m^3) [164].

4.3.3. Thermal properties results

The thermal tests were performed on all hempcrete design mixes, with only one water content (3). Table 4.4 presents the thermal properties of dry and wet hempcrete samples, including their density, thermal conductivity, specific heat capacity, and thermal diffusivity. The wet conditions represent the lab conditions (22±2^{o}C, 50±5% RH), while the dry conditions were obtained by oven-drying the samples at 60-70 ^{o}C, until the change in the mass is less than 1%. The wet hempcrete samples have higher density, thermal conductivity, and specific heat capacity than their dry counterparts due to the higher moisture content. Thus, the wet density ranges from 304 kg/m^3 to 328 kg/m^3, and the average is 320 kg/m^3, with a standard deviation of 7.7 kg/m^3 (~2.4%). The dry density is approximately 4.7% lower, ranging from 291 kg/m^3 to 312 kg/m^3 with an average of 305 kg/m^3, with a standard deviation of 6.9 kg/m^3 (~2.3%). The thermal conductivities of wet and dry samples vary from 0.0907 to 0.0981 W/m K, and from 0.0868 to 0.0937 W/m K, with averages of 0.09488 W/m K and 0.09069 W/m K, respectively. Furthermore, the specific heat capacities of wet and dry samples range from 1398 to 1557 J/kg K and from 1250 to 1421 J/kg K, with averages of 1504 J/kg K and 1360 J/kg K, respectively. These results agree with the range of specific heat capacity reported in the literature, between 1000 J/kg K and 1560 J/kg K [31, 165].

Table 4.4: Thermal properties of the hempcrete samples.

Sample	State	Density (kg/m^3)	Thermal conductivity (W/m K)	Specific heat capacity (J/kg K)	Thermal diffusivity (m^2/s) x 10^{-7}
LCB10	wet	325	0.0962	1504	1.968
	dry	309	0.0921	1350	2.209
LCB20	wet	326	0.0943	1398	2.069
	dry	311	0.0902	1250	2.321
LMK20	wet	328	0.0981	1530	1.955
	dry	312	0.0937	1385	2.169
LMK50	wet	318	0.0955	1523	1.972
	dry	303	0.0910	1379	2.178
LMK70	wet	316	0.0941	1498	1.988
	dry	301	0.0898	1352	2.206
LNHL50	wet	304	0.0907	1520	1.962
	dry	291	0.0868	1383	2.156
LNHL70	wet	323	0.0952	1557	1.893
	dry	309	0.0912	1421	2.076

Therefore, the wet samples' thermal diffusivity is lower by ~11% compared to their dry counterparts. In this respect, the thermal diffusivity of the wet samples ranges from 1.893 to 2.069 (m^2/s) x 10^{-7}, whereas dry specimens range from 2.076 to 2.321 (m^2/s) x 10^{-7}, with averages of 1.973 (m^2/s) x 10^{-7} and 2.188 (m^2/s) x 10^{-7}, respectively. These findings indicate that, in the wet state, the total increase in heat storage (ρ*cp) is higher than the increase in thermal conductivity in wet samples compared to their dry counterparts. Thus, the wet state's thermal diffusivity is lower than the dry hempcrete samples. Our results are slightly higher than the range of thermal diffusivity values reported in the literature, between 0.98 to 1.48 (m^2/s) x 10^{-7} [31, 152]. A possible explanation might be those studies' higher density range to calculate the thermal diffusivity (480-1076 kg/m^3).

The results in Table 4.4 also indicate that LCB samples have the lowest thermal conductivity for their density, the lowest specific heat capacity, and the highest thermal diffusivity. For example, the average density, thermal conductivity, specific heat capacity, and thermal diffusivity of all LCB hempcrete samples (wet and dry) are approximately 318 kg/m^3, 0.0932 W/m K, 1376 J/kg K, and 2.142 (m^2/s) x 10^{-7}, respectively. In comparison, the LMK samples have a slightly lower

average density (~313 kg/m³) but higher thermal conductivity (~0.937 W/m K) and specific heat capacity (~1444 J/kg K), with lower thermal diffusivity (2.078 (m^2/s) x 10^{-7}). The LNHL samples have the lowest average density of approximately 307 kg/m³ and, therefore, the lowest thermal conductivity of 0.091 W/m K, with the highest average specific heat capacity of 1470 J/kg K and the lowest thermal diffusivity of 2.020 (m^2/s) x 10^{-7}.

Figure 4.4 illustrates the relation between thermal conductivity and density in the dry and wet states for all design mixes. Similar to previous studies [121, 128], the dry and wet samples show a positive linear relationship between the samples' conductivities and densities with high R^2 values of 0.88. Thus, the LNHL50 samples with the lowest dry and wet densities of 291 and 304 kg/m³ have the lowest thermal conductivity of approximately 0.087 and 0.0907 W/m K, respectively. In contrast, the LMK20 samples with the highest dry and wet densities of 312 and 328 kg/m³ have the highest thermal conductivity of approximately 0.0937 and 0.0981 W/m K, respectively.

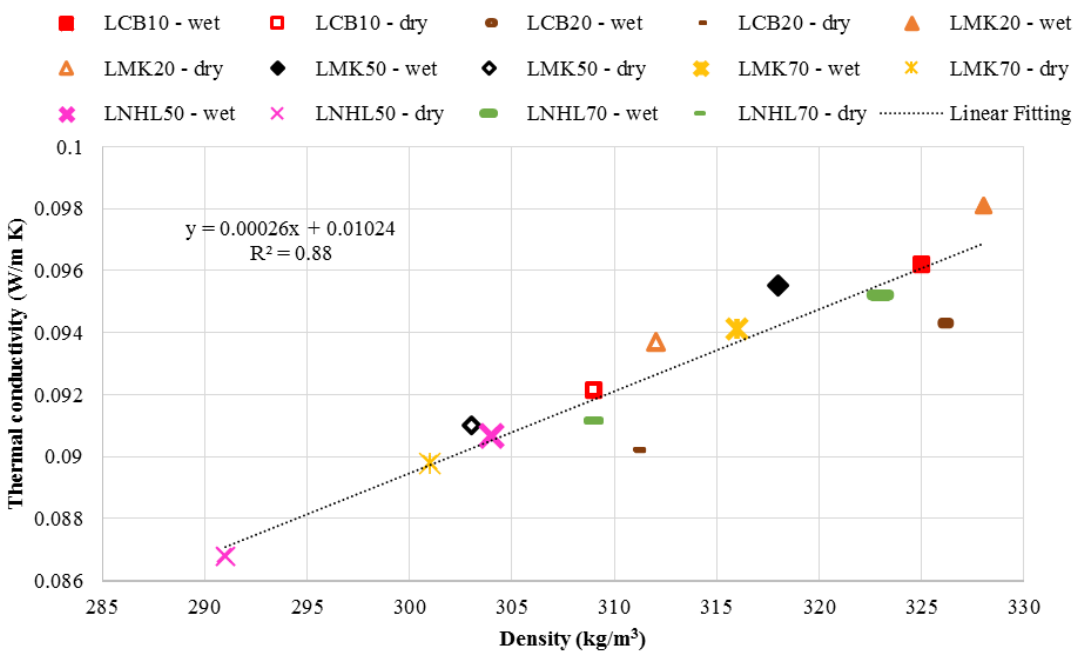

Figure 4.4. Thermal conductivity as a function of density.

Figure 4.5 also compares the experimental thermal conductivities of hempcrete samples against the results of previous studies. The results show that the thermal conductivities and their increase with the rise in density are comparable to the values reported by previous studies for the specimens with similar densities. Furthermore, some studies differentiate between testing in perpendicular (⊥) and parallel (∥) directions (i.e., heat flux direction) to the compaction of the samples. In this respect, Williams et al. (2017) [128] and Nguyen et al. (2010) [166] reported higher thermal conductivity of the similarly dense samples tested in a perpendicular than parallel direction (see Figure 4.5). Moreover, Nguyen et al. (2010) [166] reported a higher difference between the parallel and perpendicular conductivities than Williams et al. (2017) [128]. The likely reason is the higher density range of the samples in the first study compared with that of the second study. In this research, the compaction and testing directions (i.e., perpendicular or parallel) represent the worst-case scenario for the thermal properties. In this respect, the HFMA created heat flux perpendicular to the compaction direction across the samples. Thus, this study's results match experiments conducted in the perpendicular direction and show a larger difference with those performed in parallel orientation.

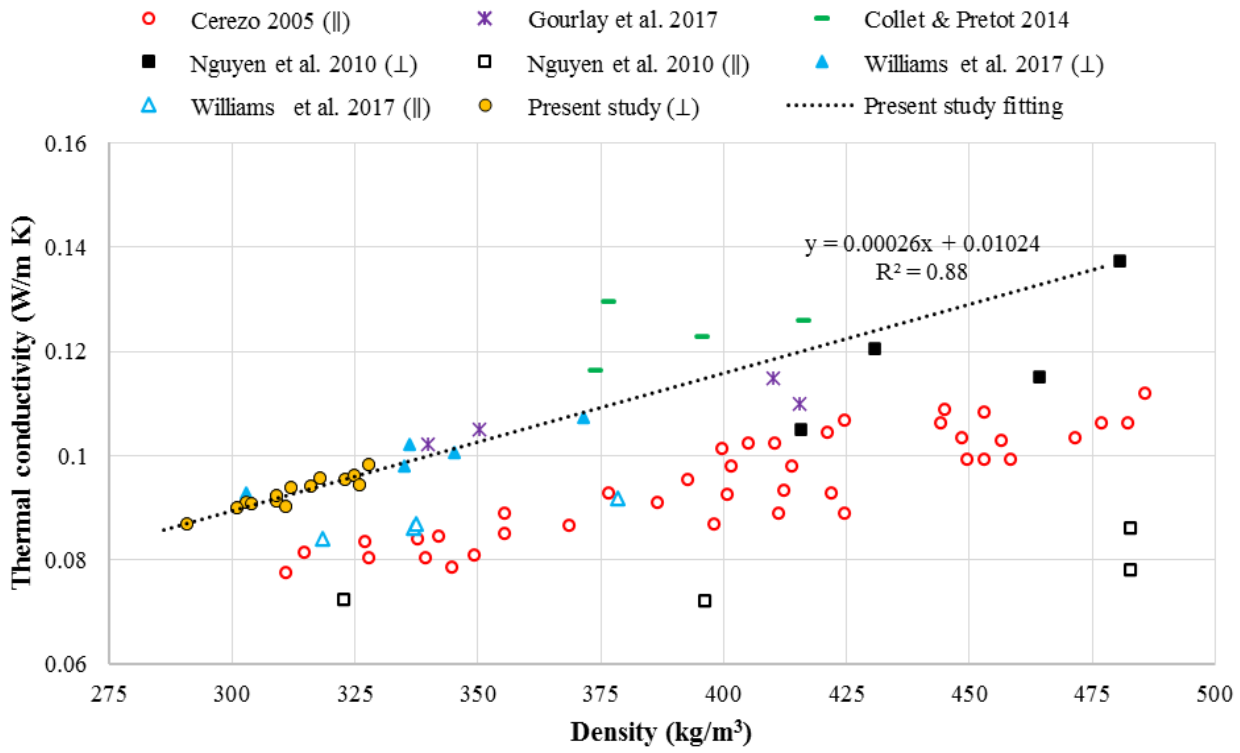

Figure 4.5. Thermal conductivity comparison with other studies.

4.3.4. Moisture buffering results

The moisture buffering tests were performed on selected hempcrete samples from each design mix, LMK50, LNHL50, and LCB10, with a higher water content (3). Figure 4.6 compares moisture buffering values (MBV) for each cycle's uptake and release phases until the steady state, with two initial high and low moisture conditions. As shown, for the high moisture initial condition, the MBV for the release phase starts with a higher value (2.4-2.6 gm/m^2 RH%) than the uptake phase (1.3-1.7 gm/m^2 RH%). The hempcrete samples tend to lose the high moisture content obtained from the initial condition more than absorbing more moisture. However, after the initial moisture content decreases, the MBV for the uptake phase increases again.

In contrast, the MBV for the release phase slightly decreases until both reach the steady state starting from the fourth cycle with less than a 5% difference between MBV for uptake and release. For the low moisture initial condition case, the MBV for the uptake phase starts with a higher value

(3-4 gm/m^2 RH%) than that of the release phase (2-2.8 gm/m^2 RH%). The hempcrete samples can absorb more moisture due to the low initial moisture content. The MBV for the uptake phase decreases again, and the MBV for the release phase slightly increases until both reach steady-state starting from the fourth cycle with a difference of less than 5% between MBV for uptake and release.

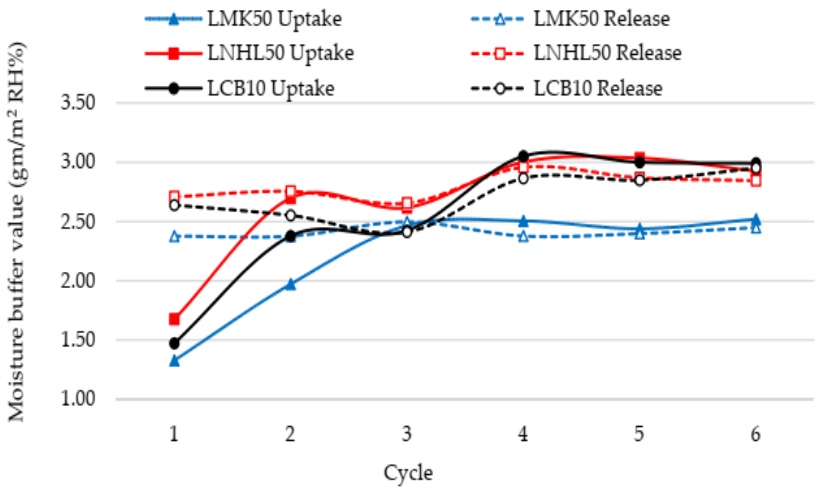

a) high moisture initial condition.

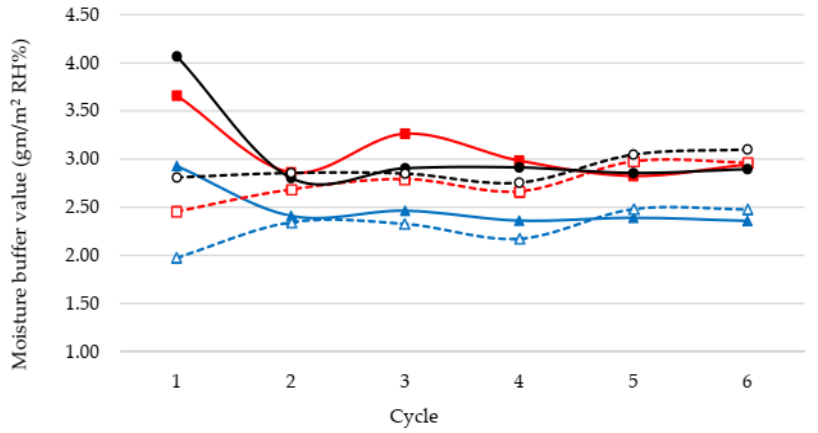

b) low moisture initial condition.

Figure 4.6. Moisture buffer value with cycles with different initial conditions: (a) high moisture content initial condition, (b) low moisture content initial condition.

The three design mixes express different moisture buffering behaviours. For example, the LNHL50 with the high initial moisture condition starts with 14% and 26% higher MBV compared to LCB10 and LMK50 in the uptake phase and 2.6% and 13.8% higher in the release phase,

respectively. Furthermore, the starting MBV values of the LCB10 with low initial conditions are 11.2% and 39% higher than those of LNHL50 and LMK50 counterparts in the uptake phase. Similarly, in the release phase, the starting MBV values of the LCB10 are 14% and 42% higher than those of LNHL50 and LMK50, respectively. Moreover, the LCB10 shows approximately 1.2% higher steady-state MBV than LNHL50 and 18% higher than LMK50.

Figure 4.7 shows the percentage mass change relative to the initial mass during the test for the selected samples subjected to the humidity cycles. All specimens show the same mass change profile with a gradual increase or decrease, depending on the initial condition, until they reach a steady state starting from the fourth cycle. Moreover, the LCB10 has the highest mass gain and release in the uptake and release portions of the cycle, respectively, regardless of the initial condition. The LNHL50 and LMK50 samples show comparable rates of mass gain and release.

Figure 4.8 presents the average steady-state MBV values of the hempcrete samples. The average steady-state MBV for all hempcrete samples of 2.78 gm/m^2 RH%, with a standard deviation of 0.24 gm/m^2 RH% (8.6%), falls in the range reported in the literature. For example, Collet et al. (2013) reported an MBV of 2.14 gm/m^2 %RH, with a binder-to-hemp ratio of 2:1 and density of 430 kg/m^3 [142], while Latif et al. (2015) reported MBV of 3.47 gm/m^2 %RH with a binder to hemp ratio of 1.2:1, and density of 290 kg/m^3 [32]. The findings suggest that the initial moisture content condition does not significantly affect each design mix's final steady-state average MBV (i.e., the difference is less than 1%).

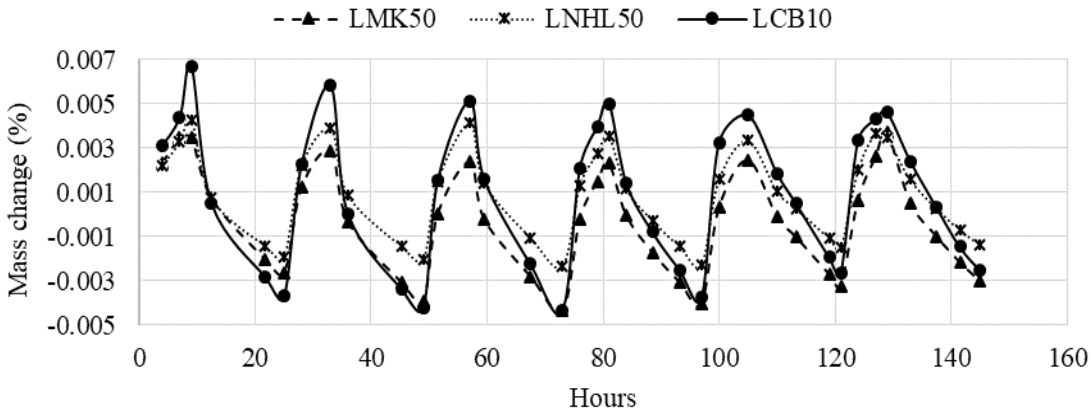

(a)

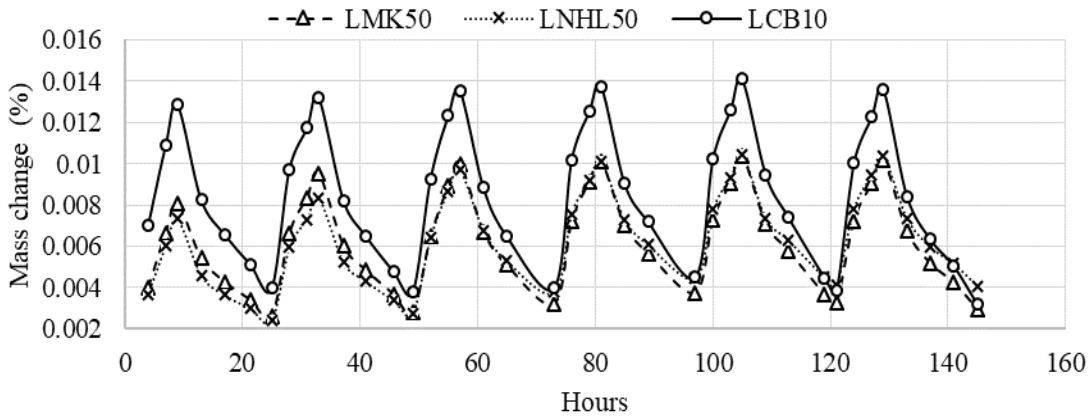

(b)

Figure 4.7. Typical steady cycle with different boundary conditions: **(a)** high moisture content initial condition, **(b)** low moisture content initial condition.

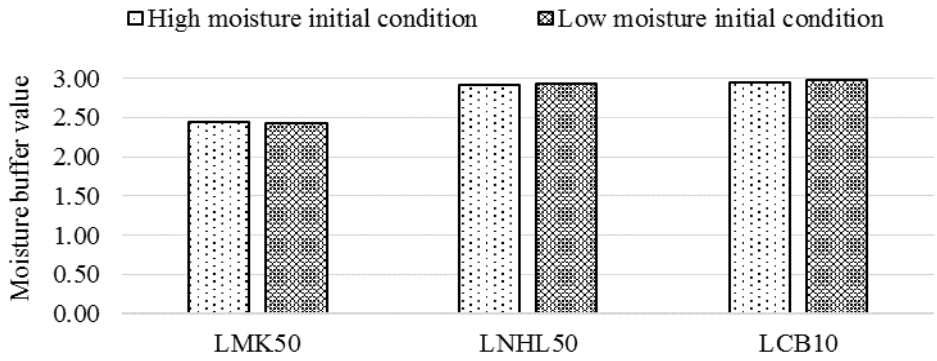

Figure 4.8. Average steady-state moisture buffer value (MBV).

4.4. Discussion

The findings suggest that hempcrete mixes with a 1:1 binder to hemp hurd ratio and 300-400 kg/m³ density have mechanical and hygrothermal properties suitable for infill wall applications. For instance, the compressive strengths ranging from 0.15 to 0.57 MPa are comparable to those reported by the previous studies that used a higher binder to hurd ratios (i.e., 2:1 and 2.25:1) [128, 137]. Similarly, thermal conductivity and specific heat capacity values in the range of 0.087-0.098 W/m K and 1250 to 1557 J/kg K correspond to the values reported by the studies that developed hempcrete samples with similar densities [31, 124, 128, 165]. Furthermore, the average steady-state MBV for all hempcrete samples of 2.78 gm/m² RH indicates excellent moisture storage capabilities. The splitting tensile strength ranging from 0.016 to 0.0348 MPa is the only measured parameter that is comparatively lower than the results of the previous studies. The likely reasons are the lower density range and the binder to this study's hemp hurd ratio. In addition, hempcrete composites made from hydrated lime have significantly lower tensile strength than composites made from commercial binder composites [25, 167].

The hempcrete's density is a vital design parameter due to its significant effects on the material's mechanical and thermal properties. For instance, on the one hand, hempcrete samples of approximately 340 kg/m^3 and above have 45% to 75% higher compressive and tensile strengths than those with lower density (i.e., 300-330 kg/m³). On the other hand, the low-density hempcrete samples (i.e., 290-310 kg/m³) have 8-13% lower thermal conductivity than those in the range of 320-336 kg/m³. Furthermore, as illustrated in Figure 4.9, putting the thermal conductivity and compressive strength on the same graph, the compressive strength shows a higher rate of change (slope) with density than the thermal conductivity. In other words, decreasing hempcrete's density to reduce thermal conductivity leads to a higher compressive strength reduction in the samples.

These findings indicate that the specific application should determine the density of the hempcrete composites.

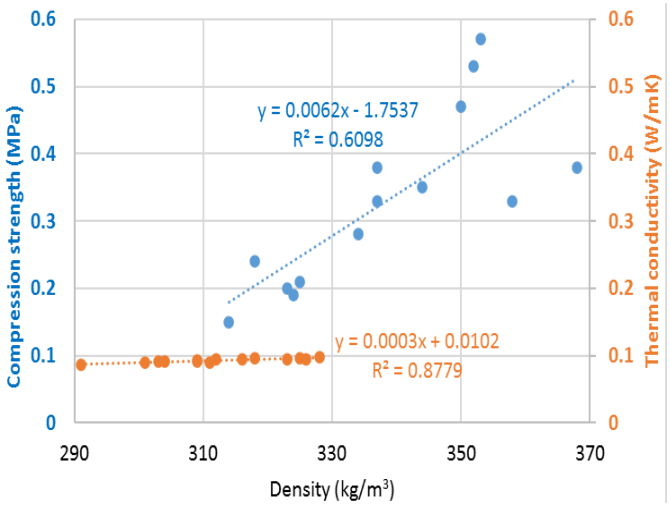

Figure 4.9. Thermal conductivity as a function of compressive strength.

The results also indicate that binder mix design and water content impact hempcrete's thermal and mechanical properties. For example, an increase in the percent share of MK and CB reduces thermal conductivity and specific heat capacity. In contrast, increasing NHL percentage increases the conductivity and specific heat capacity. In addition, an increase in the percent share of pozzolans above a certain amount can harm the mechanical properties of hempcrete, particularly when combined with reduced water content (i.e., 2.5:1 water to hemp ratio). This hindering effect is most significant when metakaolin is increased above 50%, followed by crushed brick above 10%. In small amounts, recycled crushed brick is an excellent alternative to conventional pozzolans in creating hempcrete composites with favorable thermal, moisture, and reasonable mechanical properties.

4.5. Summary

The thermal and mechanical properties of hempcrete depend on its density. Hence, the large-scale utilization of hemp-lime composites in the construction industry requires using manufactured

blocks, wall panels, or spraying techniques to construct consistent code-complying envelope systems. The higher content of hemp hurd combined with an application-orientated level and direction of compaction can lead to the development of products suitable for infill wall utilizations. While all the developed design mixes have mechanical and hygrothermal properties suitable for infill wall applications, locally sourced pozzolans such as metakaolin and recycled crushed brick showed excellent mechanical, thermal, and moisture buffering properties compared to hydraulic lime typically used in hempcrete mixes. For example, a hempcrete with 50% metakaolin had the highest compressive strength of 0.57 MPa, while the hempcrete samples with 10% crushed brick had the lowest thermal conductivity considering their density and the highest moisture buffer capacity. The water content is an essential design parameter due to its significant impact on the mechanical and thermal properties of the hempcrete samples. This study indicates that a smaller amount of water (i.e., $\leq$2.5 kg) leads to some specimens' inferior mechanical properties due to incomplete hydration caused by the high suction ability of the hemp hurd.

5. Chapter 5: Thermal, microstructural, and numerical analysis of hempcrete-microencapsulated phase change material composites

The hempcrete-PCM (HPCM) samples were produced by adding 9% and 18% of four microencapsulated PCM (MPCM) types with different phase change temperatures ranging from 18 ^{0}C to 25 ^{0}C (±1^{0}C) to hempcrete formula with 50% metakaolin as a pozzolan in the binder mix design (LMK50 sample). An in-depth understanding of the performance of the newly developed HPCM composites required the following separate but interrelated analyses. First, the microstructural characterization enabled insights into the parameters that affect the performance of the new bio-composite materials. Second, the thermal conductivity measurements of MPCM samples allowed an understanding of their impact on the thermophysical properties of HPCM samples. Finally, the numerical analysis of the hypothetical hempcrete and HPCM wall sections provided a further comprehension of the impact of MPCM integration into hempcrete on the wall's thermal performance throughout the year. This chapter first describes the ingredients and processes used to develop HPCM samples and provides the adopted method to characterise and numerically analyse them. Then, it presents and discusses the most critical results and findings related to experiments (microstructural and thermal tests) and finite volume simulation of HPCM wall assemblies. Finally, a summary is provided. This chapter is published in a journal article https://doi.org/10.1016/j.applthermaleng.2020.115520 [135].

5.1. Sample development

5.1.1. Raw materials

The hemp aggregate for hempcrete-PCM samples came from the same source as the one for hempcrete, 'Plains Hemp' in Manitoba, Canada. Likewise, hydrated lime is bought from a local supplier, whereas metakaolin is from the company 'WhiteMud Resources' in Saskatchewan,

Canada. Two microencapsulated PCM (MPCM) products, Micronal and Nextek from the company Microtek [168], with four different temperatures (18 °C, 23 °C, 24 °C, and 25 °C) are mixed with the hemp hurd, binder mix design, and water. Nextek and Micronal are microcapsules filled with Paraffin wax in the core and wrapped in a polymer shell. Nextek MPCMs, 18 °C and 24 °C, are encapsulated with robust patented Melamine-based capsules with higher thermal stability, while Micronal MPCMs, 23 °C and 25 °C, are encapsulated with Acrylic-based capsule walls [168]. Table 5.1 summarizes the main physical properties of the MPCMs used by the manufacturer.

Table 5.1. Thermal properties of MPCMs.

PCM types	Nextek 18D	Nextek 24D	Micronal DS 5040X	Micronal DS 5038X
Phase change (melting)	18±1 °C	24±1 °C	23±1 °C	25±1 °C
Phase change (solidification)	18±1 °C	24±1 °C	22±1 °C	24±1 °C
Particle Size	15-30 µm	15-30 µm	1-5 µm (50-300 µm agglomerated)	1-5 µm (50-300 µm agglomerated)
Bulk Density	~300-400 kg/m^3	~300-400 kg/m^3	~300-400 kg/m^3	~300-400 kg/m^3
Heat of Fusion	≥190 J/g	≥170 J/g	≥95 J/g	≥97 J/g

5.1.2. Composition of HPCM samples

This research continues maximizing the hemp hurd ratio within the hempcrete mixture to improve its thermal properties while reducing its carbon footprint and price. Hence, the same 1:1 hemp-to-binder ratio by weight with a density of around 300-400 kg/m³ as in the hempcrete mix design was used for HPCM samples. The binders' ratio was 50% hydrated lime and 50% metakaolin by weight (LMK50). This binder mix design has been selected to develop HPCM composites for the following reasons. The design mix (LMK50) provided the highest strength in this respect. Furthermore, metakaolin is commercially produced in Canada and worldwide, making the hempcrete and HPCM formulas applicable, transferable, and reproducible globally. As such, the

adopted methodology can positively impact hempcrete's and HPCM's commercialisation and productibility.

In contrast, while hempcrete samples with crushed brick as a pozzolan exhibited excellent thermal moisture properties and comparable mechanical performance with lower environmental impact, recycled crushed brick is not massively produced. Also, crushed brick pozzolan is a recycled product of bricks originating from different demolished buildings and sites. Thus, its physical and chemical properties may vary significantly depending on the source, adding additional variability to the hempcrete mix design and the analysis of hempcrete-PCM composites. Therefore, using recycled crushed brick as a pozzolan in hempcrete mixes would require additional extensive experimental tests and data to generate consistent, standardized procedures for its utilization in hempcrete composites, which is out of the scope of this research. This research focuses mainly on hempcrete-PCM integration and its performance as wall infills.

Due to the MPCM's high price and negatively impacting the mechanical and fire resistance properties [50], approximately 9% and 18% of each MPCM were added to the hempcrete sample. Therefore, this study analysed one hempcrete and eight HPCM samples. Table 5.2 summarizes the composition of the hempcrete and HPCM samples.

Table 5.2. Composition of hempcrete and HPCMs samples.

Name	Hemp: Binder: Water: MPCM ratio (by weight)			
	Hemp	*Binder*	*Water*	*MPCM*
Hempcrete	1	1	3	-
9%HPCM	1	1	3	0.5
18%HPCM	1	1	3	1.1

5.1.3. Mixing, moulding, and curing

The preparation and casting of HPCM samples included a procedure similar to that followed for hempcrete (see Section 4.1.3). Hence, the first step involved mixing binders with MPCMs and water to create the slurry. Next, hemp hurd was added to the slurry and mixed until a uniform mixture was produced. The mixture was then placed in a one-quarter portion at a time of rectangular moulds (20 cm wide × 20 cm long × 5.5 cm high) and tamped until reaching the desired wet density. The samples were de-moulded after seven days and cured at room temperature of 22±1 ^{o}C, with RH ~50%, for another 21 to 28 days until they reached a constant mass.

5.2. Experimental analyses

5.2.1. SEM analysis

Scanning electron microscopy (SEM) enabled the investigation of the samples' microstructure nature and any observed MPCMs' shell damage or agglomeration within HPCM samples. A Quanta 650 FEG scanning electron microscope was used to create high-resolution imaging. High-vacuum imaging mode with an Everhart Thornley Detector (ETD) was utilized for the MPCM specimen coated with a 15 nm thick coating of Gold-Palladium coating (60% Gold: 40% Pd alloy). A low-vacuum imaging mode with a Large Field Detector (LFD) was used for HPCM samples. Micrographs were created at accelerating voltages of 10 kV and 15 kV, respectively, and variable working distances from 11.4 mm to 12 mm.

5.2.2. Transient line heat source testing

Thermal conductivities of MPCMs were obtained using the transient line heat source technique, which passes a current through a long thin line immersed in a semi-infinite medium. The rate of increase in the probe temperature indicates how conductive the material is. A water bath with a temperature precision of ± 0.01 °C allowed control of the temperature of the fully immersed glass

beaker filled with MPCM. A “DP97 Tempmaster” digital thermometer connected to two thermocouples was used to detect the temperature difference between the water bath and the MPCM sample. Thermocouples were calibrated using pre-calibrated oceanographic thermocouple software: “Seaterm V2” with a precision of ± 0.001 °C. The calibrated thermocouples set to the required temperature are placed alongside the KD2 Pro needle (KS-1 needle) inside the water bath chamber. For every temperature setpoint, the thermal conductivity of the MPCM is recorded directly from the KD2 Pro meter with an accuracy of ± 5%.

5.2.3. Thermal tests

The thermal tests of the HPCM samples included thermal conductivity measurements (W/m K) and specific heat capacity (J/ kg K). These tests have been performed according to the same standards and procedures used for hempcrete samples (see Section 4.2.2 for more information).

5.3. Numerical simulation

Numerical simulations allowed the extension of the experimental results to compare the performance of timber-frame walls made of hempcrete and HPCM infills with 9% and 18% of MPCMs. Figure 5.1 illustrates the wall model developed in ANSYS Design Modeler. The HFMA experiments presented in Sections (4.3.3 & 5.4.3) produced the effective thermophysical properties of hempcrete and HPCMs (i.e., thermal conductivity and specific heat capacity). Furthermore, Table 5.3 summarizes the thermophysical properties of studs, gypsum, and cement lime plaster obtained from the WUFI software library. For simplicity at this analysis stage, melting curves are only selected for modelling (i.e., no hysteresis). The composites HPCM18 and HPCM23 are only used in this model because their phase change ranges fall within the thermal comfort range and the selected space-conditioning schedule.

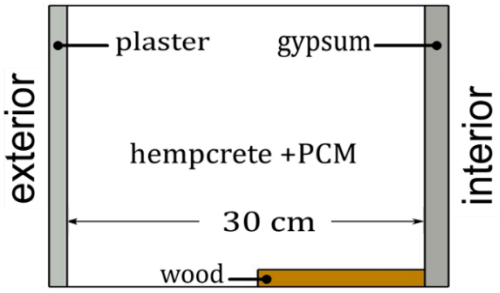

Figure 5.1. Wall geometry for numerical analysis.

Table 5.3. Thickness and thermophysical properties of the simulated materials.

	Studs	Gypsum	Cement lime plaster
Thickness (cm)	3.8 x 14	2	1.5
Density (kg/m^3)	650	675	1900
Conductivity (W/m K)	0.0734+0.0002T*	0.1434+0.0002T*	0.7434+0.0002T*
Specific heat (J/kg K)	1400	850	850

*Temperature in Kelvin.

Numerical analysis is carried out using a finite volume method (FVM) within ANSYS Fluent software. The model solves the time-dependent governing energy equation that describes heat transfer with phase change, as shown in Equation (5.1).

$$\rho \frac{\partial h}{\partial t} = \nabla . (k \nabla T), \text{ where } h = \int C_p \, dT \qquad (5.1)$$

Where ρ is the density (kg/m^3), t is time (seconds), C_p is specific heat capacity (J/kg K), k is thermal conductivity (W/m K), T is temperature (K), and h is the enthalpy (J/kg).

Figure 5.2 illustrates the mesh independence check for sample 18HPCM18 (the highest storage capacity) in winter (January) and summer (July). Three different numbers of elements were compared: coarse mesh (723518), medium mesh (1146750), and fine mesh (1920000). As shown, all mesh sizes show excellent temperature agreement and good energy agreement. Nevertheless, because of the better energy consumption agreement between the medium and fine mesh in July, the medium mesh is used in this study.

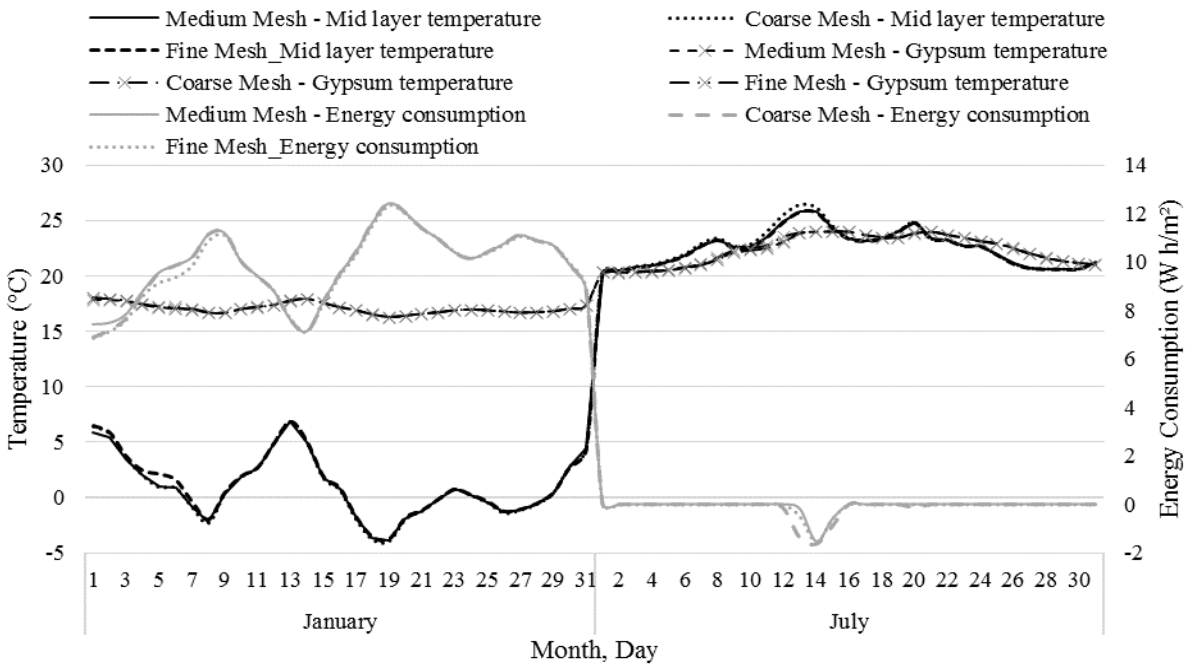

Figure 5.2. Mesh independence check for case 18HPCM18 in January and July.

Table 5.4 presents the internal and external boundary conditions used in this modelling. External boundary conditions applied at the cement lime plaster layer include the solar heat flux (q_{solar}), external air temperature (T_{ext}), and external heat transfer coefficient (h_{ext}). The Canadian Weather for Energy Calculations file, composed of hourly weather data records selected from a 30-year database for Winnipeg, and the building modeling tool EnergyPlus, were used to generate data of solar flux, external air temperature, and wind speed (V) for a south wall orientation. The plaster layer's solar absorptivity (α) is assumed to be 0.6, and the external heat transfer coefficient is calculated using Liu and Harris (2015) model [169] as it is suitable for low-rise buildings [170]. Internal boundary conditions applied at the gypsum board are the internal heat transfer coefficient (h_{in}) and the internal room schedule (T_{room}). The internal heat transfer coefficient is calculated using Awbi and Hatton's (1999) model [171], where D_h is the hydraulic diameter calculated for a 3 m × 2.75 m wall.

Table 5.4. External and internal boundary conditions.

Surface	Boundary conditions	Equation
Plaster layer	External air temperature = Weather file Solar radiation = Weather file External heat transfer coefficient = 5.67V+ 3.25	$q_{ext} = \alpha q_{solar} + h_{ext}(T_{ext}-T_{wall})$ α (solar absorptivity) assumed 0.6.
Gypsum layer	Internal heat transfer coefficient = $\frac{1.823}{D_h^{0.121}}\ \Delta T^{0.293}$ Internal air temperature = User-defined function for room schedule: Heating T< 20 °C Cooling T> 24 °C Unconditioned 20 °C < T< 24 °C	$q_{int} = h_{in}(T_{room}-T_{wall})$ D_h = (4 Area)/Perimeter, $\Delta T=\lvert T_{room}-T_{wall}\rvert$.

A user-defined function is created to implement the space-conditioning schedule presented in Table 5.4 and take the effect of heat gains and losses through the wall on the internal wall temperature (T_{wall}). The space-conditioning schedule applies a dead band (i.e., unconditioned state) between 20 °C and 24 °C. The heating starts when the temperature falls below 20 °C, whereas the cooling begins when the temperature rises above 24 °C. It is important to note that the heating and cooling setpoints are fixed for the entire day at this stage for simplicity (i.e., no difference between active and dormant hours). It is also important to note that the developed model applies symmetry boundary conditions at the stud and cavity centerlines, and it does not consider the interfaces and corners between walls, solar gains through windows, internal loads, and radiation exchange between interior surfaces.

5.4. Results

5.4.1. Microstructural characterization

Figure 5.3 presents the microstructure of the two MPCM products (Nextek MPCM (Figure 5.3a), and Micronal MPCM (Figure 5.3b)) and two HPCM samples (Nextek HPCM (Figure 5.3c), and Micronal HPCM (Figure 5.3d)). As illustrated, Nextek microcapsules range in size from approximately 3μm to 30 μm, and they tend to retain their spherical shape with nearly no signs of shell fracture or observable agglomeration. Compared to Nextek, Micronal exhibits higher signs

of degradation and agglomeration of small micro-particles that bond together to form a macro capsule with a size of approximately 50 µm. These findings support the manufacturer's reports about the more robust nature of the Nextek shell. The observed shell degradation indicates that high shear forces during the mixing, moulding, and tamping stages of HPCM production may cause a capsule fracture, especially of Micronal MPCMs. Capsule damage can lead to the escape of the MPCMs' core during melting, thus negatively affecting the HPCMs' heat storage quality and mechanical strength [172, 173].

Therefore, for creating the HPCM Micronal samples, a slower process for each step is necessary to avoid any destruction that may occur for the capsules and to create a uniform distribution for the capsules, especially knowing that, in the numerical model, it was made the assumption of spatial homogeneity of the MPCMs within HPCM samples at the macro-scale level. Figure 5.3 illustrates intact and well-dispersed MPCM particles within the hempcrete specimen of both HPCM samples, Nextek HPCM–c and Micronal HPCM–d, with no signs of capsule damage or observable agglomeration. Nevertheless, it is worth noting that due to the small sample sizes involved in the SEM analysis, a level of uncertainty exists regarding the assumption about the uniform distribution, especially of Micronal MPCMs within hempcrete.

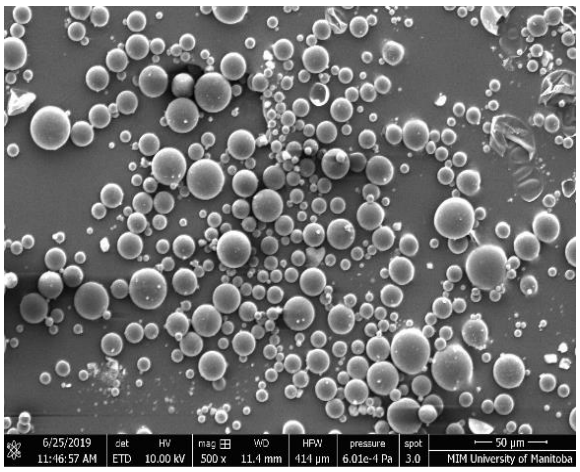

a) Nextek MPCM

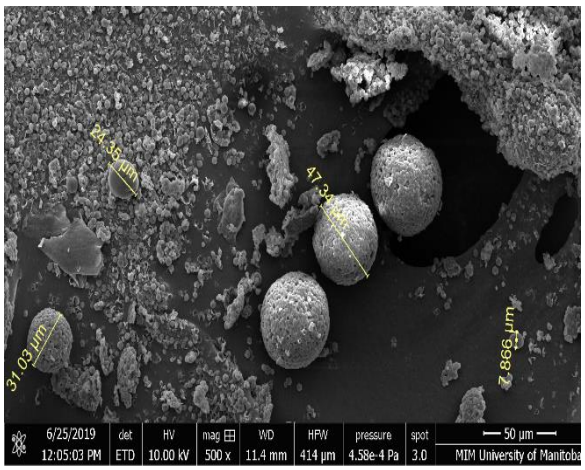

b) Micronal MPCM

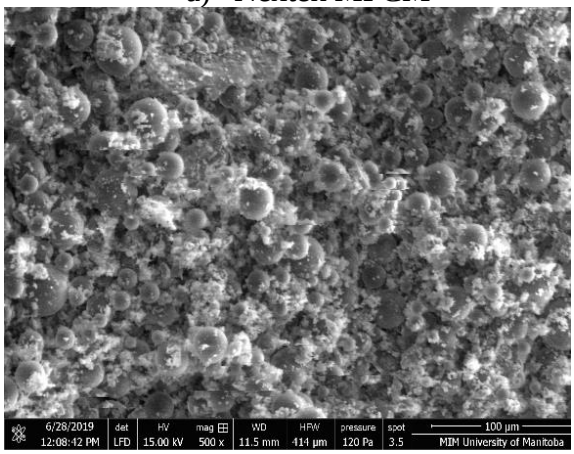

c) Nextek HPCM

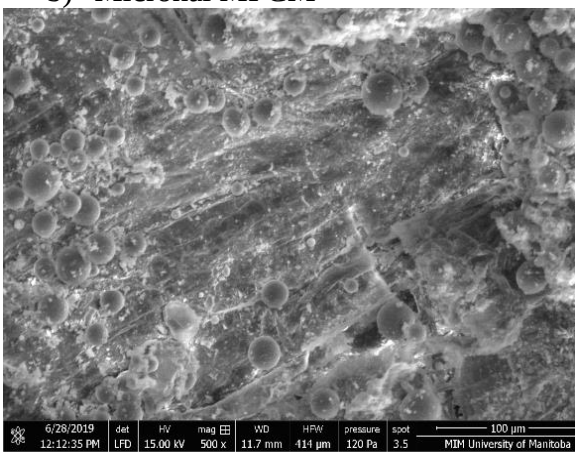

d) Micronal HPCM

Figure 5.3. The microstructure of MPCMs and HPCMs.

5.4.2. MPCM thermal conductivity

The thermal conductivity of MPCM samples was measured by KD2 pro meter at different temperatures covering solid and liquid regions. Figure 5.4 compares the thermal conductivity measurements of four MPCM samples (i.e., MPCM18, MPCM24, MPCM23, and MPCM25), and Table 5.5 summarizes the average thermal conductivities and standard deviations in solid and liquid regions of the four MPCM samples. Overall, there is a significant difference between the thermal conductivity curves and phase change periods of the MPCM samples, especially between the two product brands, Micronal (MPCM23 and MPCM25) and Nextek (MPCM18 and MPCM24). For instance, the Nextek MPCMs have lower thermal conductivity profiles than the

Micronal MPCMs in solid and liquid regions. Thus, as illustrated in Figure 5.4, at peak melting temperature, MPCM25 has the highest thermal conductivity of 0.161 W/m K, followed by MPCM23 with 0.128 W/m K. Thermal conductivities of the MPCM18 and MPCM24 are approximately 56% and 61%, respectively, lower compared to the maximum thermal conductivity of MPCM25.

In addition, MPCM23 has the highest average thermal conductivity of 0.117 W/m K in the solid region, followed by MPCM25 with 0.115 W/m K, while MPCM23 has a lower thermal conductivity (0.071 W/m K) in the liquid region than MPCM25 (0.077 W/m K). Thermal conductivities of the MPCM18 and MPCM24 are approximately 39% and 46%, respectively, lower compared to the maximum thermal conductivity in the solid region and lower by 20% and 42% compared to the maximum thermal conductivity in the liquid region. The standard deviation values are higher in the solid region than the liquid region in Micronal products, while Nextek samples have a higher standard deviation in the liquid region than the solid region.

Moreover, MPCM23 and MPCM25 have a broader phase change temperature range of ~1.5 °C compared to ~0.5 °C of MPCM18 and MPCM24. The figure shows that all samples have a higher thermal conductivity in the solid than the liquid region, especially MPCM23, and MPCM25, in which thermal conductivities dropped by approximately 45% and 52%, respectively, when transitioning from the solid to the liquid phase. Meanwhile, the percentage drop in thermal conductivity due to phase transition from solid to liquid of MPCM18 and MPCM24 is only 14% and 21%, respectively. The possible reasons for differences in the thermal conductivities of the MPCM samples include different shell types, shell-to-PCM ratios, and encapsulation techniques and efficiencies of the two MPCM brands.

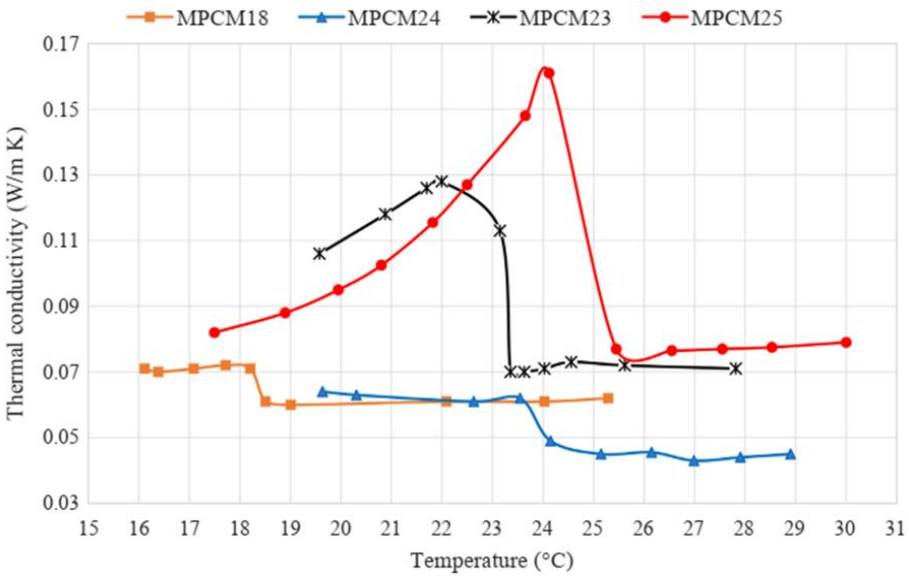

Figure 5.4. Thermal conductivity of the investigated MPCMs.

Table 5.5. Average thermal conductivities and standard deviations in solid and liquid regions of the MPCM samples.

Product		Solid region		Liquid region	
		Average conductivity (W/m K)	Standard deviation	Average conductivity (W/m K)	Standard deviation
Nextek	MPCM18	0.071	0.00063 (0.89%)	0.061	0.00063 (1.03%)
	MPCM24	0.063	0.00111 (1.76%)	0.045	0.00186 (4.13%)
Micronal	MPCM23	0.117	0.00816 (6.97%)	0.071	0.00107 (1.51%)
	MPCM25	0.115	0.02675 (23.3%)	0.077	0.00086 (1.12%)

5.4.3. HPCM thermophysical properties

5.4.3.1. Thermal conductivity results

Figure 5.5 presents and compares the results of the steady-state tests of the hempcrete and eight HPCM samples, including 9HPCM18 (9% of MPCM18^{0}C), 18HPCM18 (18% of MPCM18^{0}C), 9HPCM24 (9% of MPCM24^{0}C), 18HPCM24 (18% of MPCM24^{0}C), 9HPCM23 (9% of MPCM23^{0}C), 18HPCM23 (18% of MPCM23^{0}C), 9HPCM25 (9% of MPCM25^{0}C), and 18HPCM25 (18% of MPCM25^{0}C). Incorporating MPCM in the hempcrete mixture introduces

two interrelated effects on thermal conductivity. On the one hand, the addition of MPCMs decreases the thermal conductivity of HPCM samples because of the lower thermal conductivity of MPCMs compared to hempcrete (except MPCM23 and MPCM25 in the solid region).

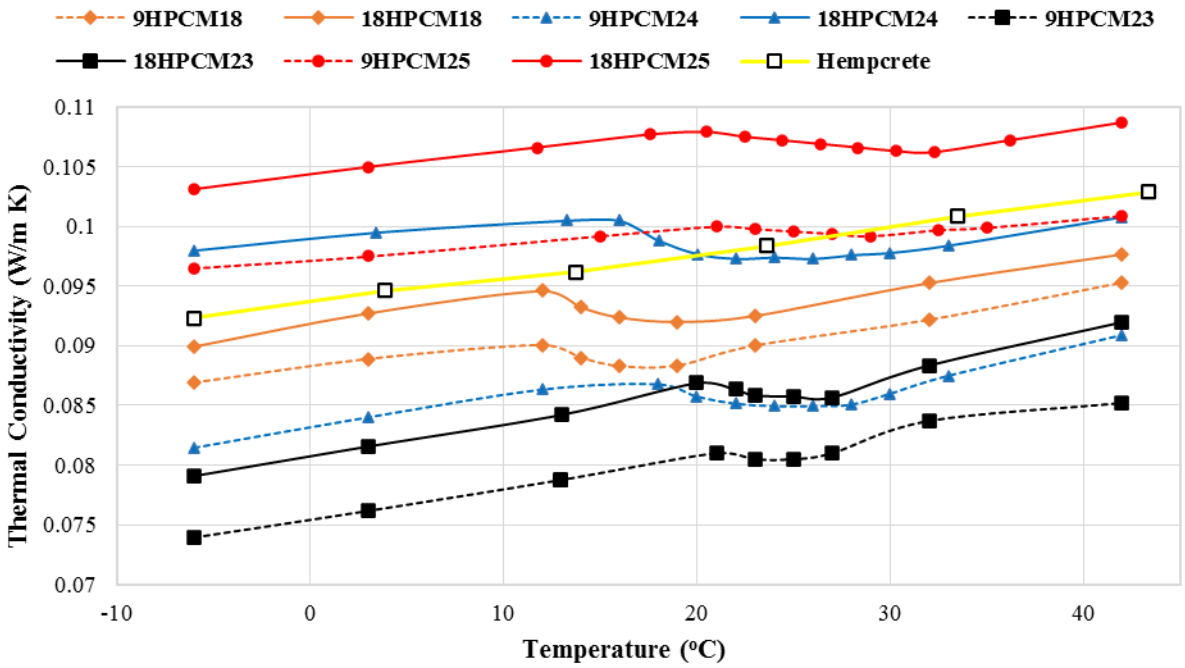

Figure 5.5. Thermal conductivity of HPCM samples compared to hempcrete.

On the other hand, MPCMs change hempcrete's density according to MPCMs density and percentage. Previous studies (and in Chapter 4) reported that the thermal conductivity is linearly proportional to the sample's density for hempcrete mixes. In this respect, Figure 5.6 illustrates the relation between the averaged thermal conductivity and density for HPCM samples (the standard deviation for all samples between 1.2%-3.5%). It can be observed that there is almost a linear relationship between the samples' conductivities and densities. Thus, 9HPCM23 has the lowest thermal conductivity of approximately 0.084 W/m K because of its lowest density of 300 kg/m^3. In contrast, 18HPCM25 has a maximum thermal conductivity of approximately 0.112 W/m K because of its highest density of 412 kg/m^3. However, the rate of increase for the thermal conductivity with density is slightly lower in HPCM than in hempcrete (Section 4.3.3), as shown

from the fitting equations (i.e., the slope). It is also important to note that Figure 5.5 shows that the conductivity percentage drop in all HPCM samples due to transitioning from solid to liquid regions is negligible compared to the MPCMs. For example, the 18HPCM18 and 18HPCM24, which show the highest decrease, have only 2.7% and 3.2% conductivity drops due to transition, respectively.

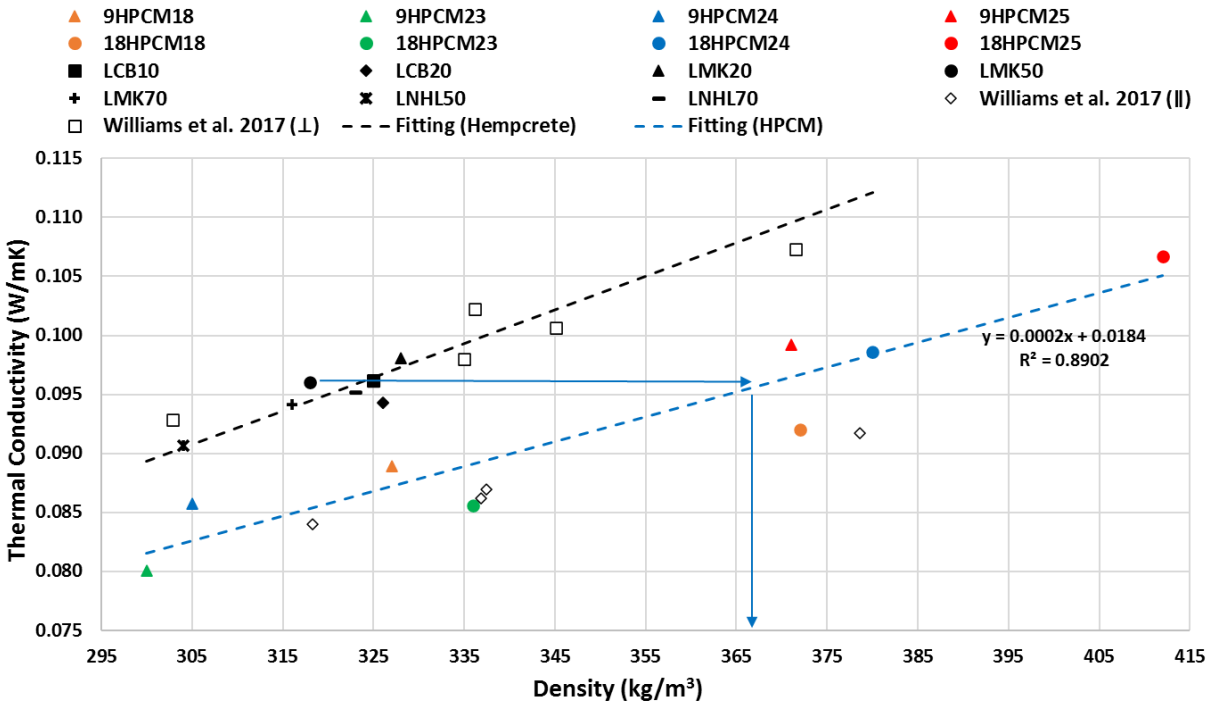

Figure 5.6. Thermal conductivity and density in solid and liquid regions of HPCM samples.

Furthermore, for some HPCM samples, the effect of lower MPCM conductivity outweighs the impact of increased density. For example, 9HPCM18, 18HPCM18, and 18HPCM23 have approximately 3%, 17%, and 6% higher densities than hempcrete (318 kg/m^3) and, on average, 9%, 4.5% and 11%, respectively, lower thermal conductivities. However, a further increase in the density of the HPCM sample, such as 18HPCM25 with a density of 412 kg/m^3, would eventually result in higher thermal conductivity than hempcrete. Consequently, an increase in the percentage of MPCM from 9% to 18% didn't reduce thermal conductivity but increased the samples' density and, therefore, the thermal conductivity. This could have a dual impact on the performance of the

wall because, on the one hand, it would increase its storage capacity and, on the other hand, lower its thermal resistance to heat flow.

Figure 5.6 also compares the HPCM samples' average thermal conductivity against the hempcrete samples presented in Chapter 4. The trending line of the thermal conductivity of HPCM samples shows that HPCM composites have lower thermal conductivities (by 11% on average) than hempcrete samples in the same density range, as compared with the fitted model developed in Chapter 4. The figure also shows that for the sample (LMK50), the corresponding HPCM sample that has the same conductivity has a density of ~367 kg/m^3, which is higher than that of the sample LMK50 (318 kg/m^3) by ~15.4%. In other words, adding MPCM to hempcrete increases the storage capacity in all cases and affects the thermal conductivity according to the HPCM resultant density compared to the base hempcrete density. Thus, the density of the HPCM samples should be controlled so that the thermal conductivity would be the same as the base hempcrete sample (in the worst-case scenario).

Figure 5.6 also compares with Williams et al.'s (2017) results for perpendicular and parallel testing of thermal conductivity [128]. In this research, all HPCM samples were created and tested using a perpendicular method, the same as hempcrete. The figure shows that the thermal conductivity of HPCM samples is lower than the perpendicular results of Williams et al. (2017), which is nearly similar to the hempcrete results but still higher than the parallel results. These findings indicate a potential to further decrease the thermal conductivity of HPCM samples by controlling the compacting process orientation.

5.4.3.2. Specific heat capacity results

Figure 5.7 presents the curves of the specific heat capacity of the hempcrete and HPCM samples measured by the HFMA dynamic procedure. The increase in the amount of MPCMs increased the

specific heat capacity of hempcrete but with variations between the HPCM samples. Thus, 18HPCM18 has the most significant specific heat capacity (10590 J/kg K), approximately seven times higher than the hempcrete sample (~1523 J/kg K), followed by 18HPCM24 (8426 J/kg K), 18HPCM25 (7457 J/kg K), and 18HPCM23 (2605 J/kg K) samples.

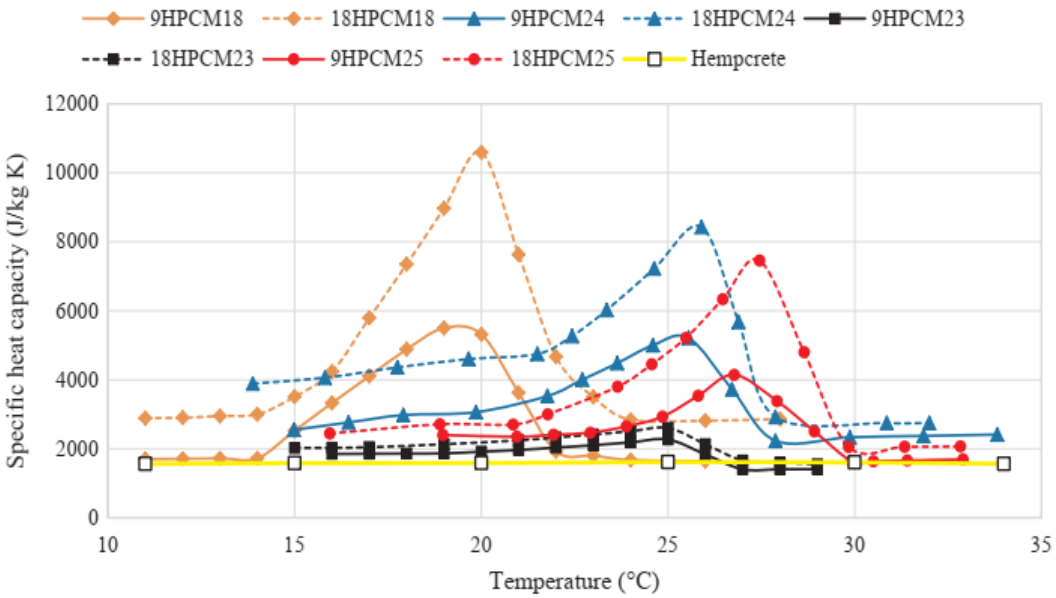

Figure 5.7. Specific heat capacity for HPCM samples compared to hempcrete.

To better understand the difference in specific heat values of HPCM samples, we calculated the encapsulation efficiency of the MPCMs according to Equation (5.2) [174]:

$$E = \frac{\Delta H_{MPCM,m} + \Delta H_{MPCM,f}}{\Delta H_{PCM,m} + \Delta H_{PCM,f}} \qquad (5.2)$$

Where $\Delta H_{MPCM,m}$ and $\Delta H_{MPCM,f}$ are enthalpies of the melting and freezing of MPCM, respectively, and $\Delta H_{PCM,m}$, and $\Delta H_{PCM,f}$ are enthalpies of the melting and freezing of pure PCM, respectively. Assuming equal melting and freezing enthalpies in both MPCM and PCM and using the manufacturer data from Microtek (MPCM) and PureTemp (PCM), the calculated approximate encapsulation efficiency values are presented in Table 5.6. The differences in encapsulation efficiencies between the HPCM samples explain the differences in specific heat profiles. Thus, HPCM18 has the highest specific heat capacity and maximum encapsulation efficiency of 98.9%,

followed by HPCM24, with an encapsulation efficiency of 82.1%, and HPCM25, with an encapsulation efficiency of 52.4%. The specific heat capacity of HPCM23 did not significantly benefit from an increase in MPCMs, and the likely reason is its lowest encapsulation efficiency of only 47.3%. These results also suggest that the amount of MPCMs can be reduced using high encapsulation efficiency products to achieve the desired increase in storage capacity without negatively affecting cost and mechanical properties.

Table 5.6: Encapsulation efficiency of MPCMs.

Melting temperature (°C)	MPCM phase change enthalpy (kJ/kg)	PCM phase change enthalpy (kJ/kg)	E (%)
18	190	192	98.9
24	170	207	82.1
23	95	201	47.3
25	98	187	52.4

Figure 5.8 presents the hysteresis effect on the specific heat capacity in the HPCM samples. As illustrated, the specific heat capacity profiles have a hysteresis effect of approximately 4–8 °C and a broad phase change range of roughly 6–10 °C, whereas an increase in the percentage share of MPCM from 9% to 18% results in a hysteresis increase of approximately 0.7–2.2 °C. The delay of heat transfer to MPCMs during the phase change process caused by the combined effect of several factors, including MPCMs shell thickness, air gaps, different capsule sizes, and mixing of capsules in the hempcrete with other materials (i.e., binders, hemp hurd) is the likely reason for the pronounced hysteresis effect in all HPCM samples [175, 176].

Nevertheless, the results presented herein lead to the following conclusions. First, HPCM18 and HPCM24 samples with Nextek products have more pronounced hysteresis than HPCM23 and HPCM25 samples with Micronal products. In this regard, the most significant hysteresis is the sample 18HPCM18, which has the highest specific heat capacity and contains MPCM18 with the highest heat of fusion. Next is sample 18HPCM24, which has the second-highest specific heat

capacity and incorporates MPCM24 with the second-highest heat of fusion. In third place is sample 18HPCM25, which has the third-highest specific heat capacity and contains MPCM25 with the third-highest heat of fusion. In contrast, the most negligible hysteresis effect shows the sample 9HPCM23, which has the lowest specific heat capacity, and MPCM23, with the most moderate heat of fusion.

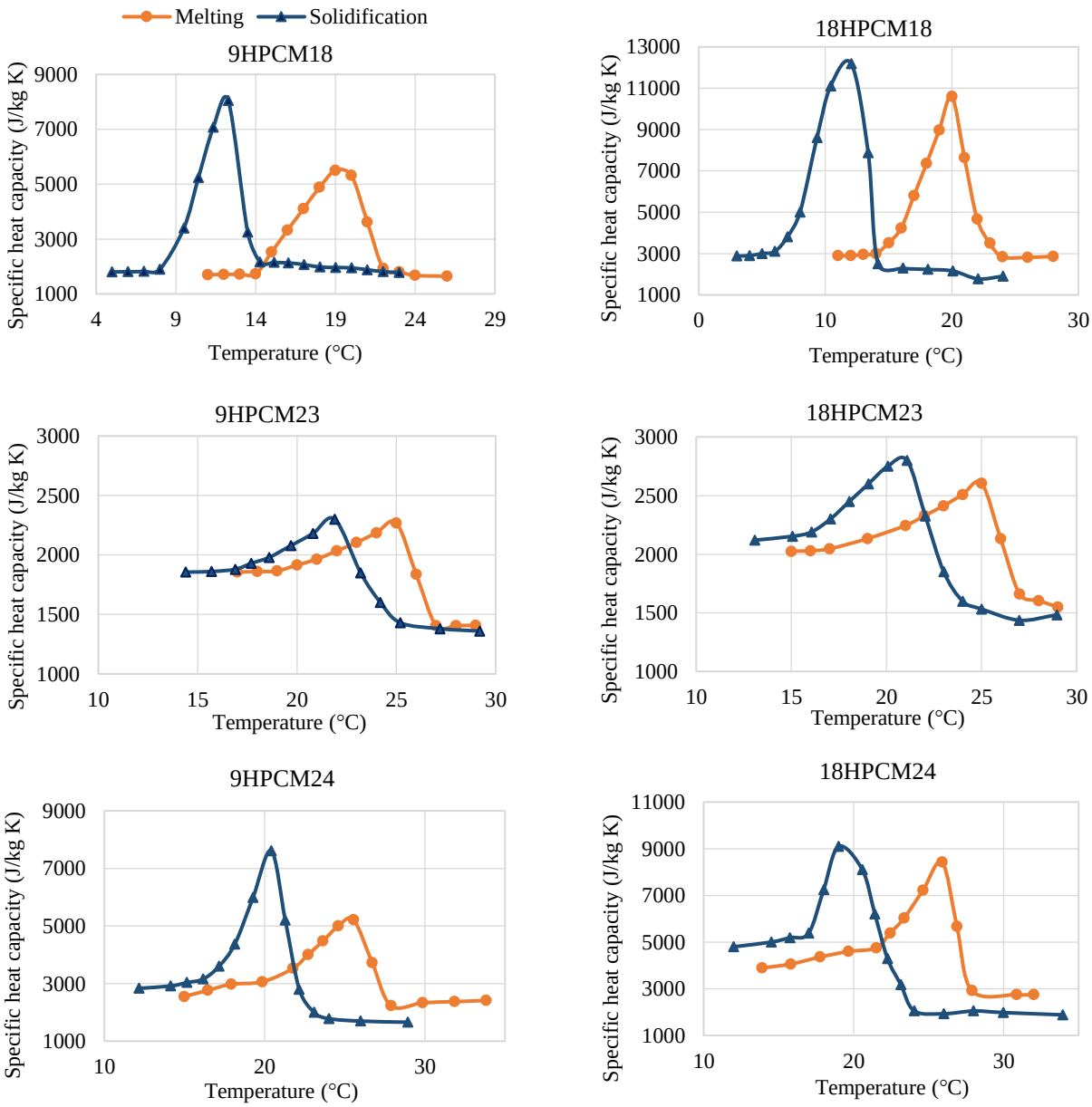

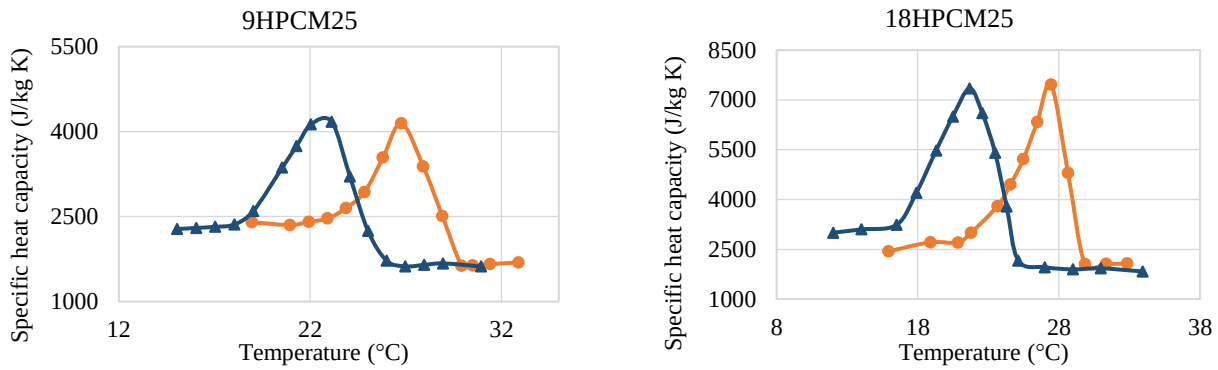

Figure 5.8. Specific heat curves of HPCM samples with a hysteresis effect.

5.4.4. Numerical analysis

The phase change performance of PCMs is highly dependent on their state. For instance, PCM in the phase change region indicates storage/release of energy and functioning of the PCM rather than being in a fully liquid/solid state [89]. For a general understanding of the impact of MPCMs integration into the hempcrete wall, the number of phase change hours throughout the year is calculated and presented at three different wall layers. In this regard, Figure 5.9 shows the annual number of hours when the average temperature is within the phase change range of HPCM18 and HPCM23 at distances (7.5 cm, 15 cm, 22.5 cm) from the gypsum-HPCM interface. As illustrated, the annual number of phase change hours differs between the three layers, with a declining trend from the inner to the outer layer of all HPCM samples, particularly pronounced in HPCM18 samples. For example, the decline in the annual phase change hours between the internal and external layer is 46% for 9HPCM18 and 44% for 18HPCM18, whereas it is only around 18% for 9HPCM23 and 18HPCM23. Furthermore, there is a high positive linear correlation ($R^2 \approx 0.95$–0.98, depending on the sample) between the annual number of phase change hours and the layer's position within the wall. The results also suggest that HPCM18 walls had two to three times higher annual phase change hours than HPCM23 walls (depending on the layer position and MPCM percentage).

Figure 5.9 also suggests that an increase in the percentage share of MPCM18 from 9% to 18% increases the number of phase change hours for 18HPCM18 at the three layers, whereas this effect does not occur in 18HPCM23. The possible reason is the 50% lower phase change enthalpy and encapsulation efficiency of MPCM23 compared to MPCM18 (see Table 5.6).

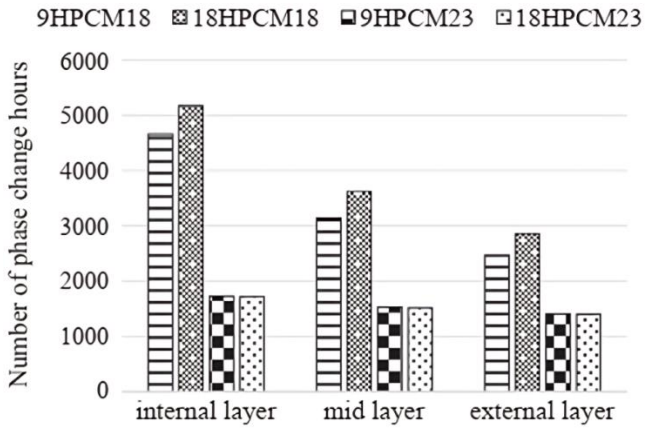

Figure 5.9. Annual phase change hours of HPCM walls

Table 5.7 summarizes the annual heating, cooling, and total energy consumptions, with the corresponding percentage savings. Overall, all HPCM walls reduce energy consumption compared to the hempcrete wall. The improved storage capacity of HPCM walls, coupled with their lower thermal conductivity compared to the hempcrete wall, are the reasons for the overall better thermal performance of HPCM walls than the hempcrete wall. The findings also show that HPCM23 walls generate considerably higher energy savings than HPCM18. In this regard, the 9HPCM23 wall achieves the most considerable total energy savings of approximately 16%, whereas the 18HPCM18 wall has the lowest total energy savings of roughly 5%. Considering that HPCM18 walls have a higher number of phase change hours than HPCM23 walls, approximately 12% and 15% lower thermal conductivity of 9HPCM23 wall compared to 9HPCM18 and 18HPCM18 walls, respectively, is the likely explanation for these results.

Moreover, an increase in the MPCM percentage share from 9% to 18% hinders the thermal performance of HPCM walls by mainly increasing their cooling energy consumption and, to a lesser degree, their heating energy consumption. Thus, cooling energy savings are approximately 7% lower for 18HPCM23 than the 9HPCM23 wall, whereas this difference is almost 14% for HPCM18 walls. Also, 18HPCM23 and 18HPCM18 walls achieve about 4% and 2% lower heating energy savings than their 9% counterparts. Table 5.7 also shows that HPCM23 and 9HPCM18 walls deliver between 55% and 60% higher cooling than heating energy savings. Winnipeg's winters are long and extremely cold, with average outdoor air temperatures ranging from - 5 °C to - 20 °C. In contrast, summers are short and warm, with average outdoor air temperatures ranging from 5 °C to 25 °C. As a result, the total cooling energy savings are only a fraction of the heating energy savings.

Table 5.7. Comparison of the annual energy consumption for HPCM walls.

	Consumption (W h/m²)			Percentage savings (%)		
	Heating	Cooling	Total	Heating	Cooling	Total
Hempcrete	39289.48	481.65	39771.14	-	-	-
9HPCM18	36713.24	411.51	37124.75	6.56	14.56	6.65
18HPCM18	37408.15	477.32	37885.47	4.79	0.90	4.74
9HPCM23	33123.90	308.46	33432.35	15.69	35.96	15.94
18HPCM23	34803.56	341.82	35145.38	11.42	29.03	11.63

Figure 5.10 compares the monthly heating and cooling energy consumptions of HPCM and hempcrete walls to enable a better understanding of their thermal performance throughout the year. Winnipeg experiences relatively low evening and night temperatures, averaging approximately 15 °C during the three warmest summer months. Therefore, all wall types require heating throughout the year, whereas they mostly need cooling during the warmest months, July and August. The results also illustrate the difference in the monthly performance of HPCM walls. Thus, an increase in the percentage share of MPCMs from 9% to 18% has the most adverse effect on heating energy

consumption during the winter months (i.e., December to March), and this negative impact declines during the shoulder seasons.

On the other hand, 18HPCM18 reduces the heating energy consumption during the summer months (i.e., June to September) and eliminates it during July and August. Regarding the cooling, 18HPCM walls perform better in July than 9HPCM walls, but vice versa in August. Thus, in July, 18HPCM18 and 18HPCM23 achieve cooling energy savings of almost 70% and 50%, respectively, whereas 9HPCM18 and 9HPCM23 generate savings of approximately 21% and 35%, respectively. In August, 9HPCM23 achieved the most substantial cooling energy savings of roughly 36%, whereas savings associated with 18HPCM23 are half as much. Moreover, 18HPCM18 is the only HPCM wall type with approximately 27% higher cooling energy consumption than the hempcrete wall during August. Additionally, Figure 5.11 indicates that all HPCM walls increase the number of zero-consumption hours compared to the hempcrete wall. Primarily, HPCM18 wall types increased the number of zero-consumption hours between 69 and 195 from June to September compared to the hempcrete wall.

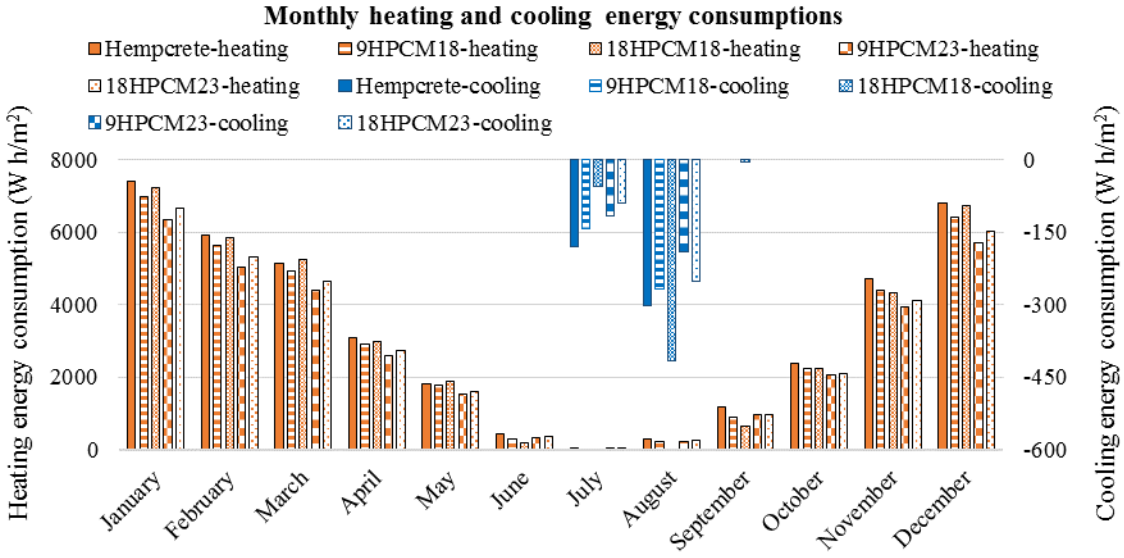

Figure 5.10. Comparison of the total monthly heating and cooling energy consumption.

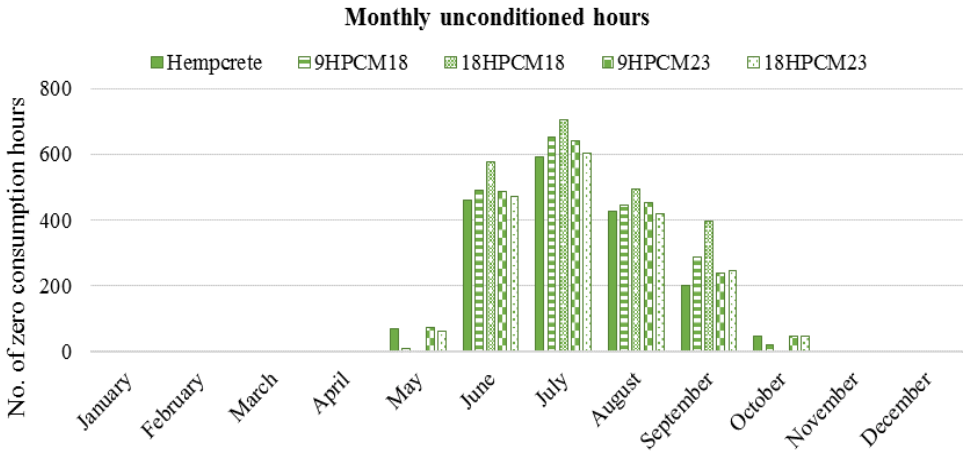

Figure 5.11. Comparison of monthly zero consumption hours.

5.5. Summary

The microstructural analysis indicates that new Nextek products exhibit better shell integrity and less agglomeration than the previous Micronal, leading to more robust MPCM samples. In addition, the Nextek products have lower thermal conductivity and better encapsulation efficiency than the Micronal products. Incorporating MPCMs into a hempcrete mixture produced a new latent material with different thermal properties and behavior. Thus, the developed HPCM formulas have superior heat storage potential than hempcrete. Especially Nextek products MPCM18 and MPCM24 had approximately 45% higher encapsulation efficiency than Micronal products MPCM23 and MPCM25. There is a strong relation between the thermal conductivity and density of the HPCM samples, which suggests that achieving the desired density and conductivity requires precise control of the tamping process and ingredient amounts.

The numerical analysis showed promising savings in heating and cooling, ranging from approximately 5% to 16% and 1% to 36%, respectively. The numerical analysis provided a generalized comparison between the different simulated walls regarding the phase change hours and energy consumption. In addition, it is vital to mention that HPCM simulation in ANSYS Fluent was done with melting curves, only neglecting the hysteresis phenomena at this stage. Hence,

better modelling should include the hysteresis phenomena and a detailed comparison of energy consumption and phase change characteristics are provided in the following steps. Considering that hysteresis's impact on the thermal performance of PCM-enhanced building envelope components might increase in the case of MPCM share increase or different PCM integration methods, such as macroencapsulation (pouches), there is a need for improvement of the method for modeling the hysteresis effect.

6. Chapter 6: Hysteresis model predictions of thermal performance of hempcrete-based walls with phase change materials

A new hysteresis model, Modified Scale (MScale), was developed and integrated into ANSYS Fluent to overcome the idealizations assumed in the existing PCM simulation methods and produce realistic and accurate predictions. In this respect, MScale enables the more realistic modelling of incomplete phase change processes than the methods currently embedded in software capable of PCM simulation, such as ANSYS Fluent, EnergyPlus, and TRNSYS. Thus, by introducing a new liquid fraction reference path, the MScale allows for changing the liquid fraction during partial phase change with a different rate than in the Track model and allows a transition to a different phase change curve without idealization that the liquid fraction is constant as in the Switch and Scale models. The MScale model is validated and compared against the Track, Switch, and Scale models. The performance of the four hysteresis models is presented and compared on wall assemblies with the two most often PCM integration approaches, microencapsulation and macroencapsulation (pouches). Further analyses were performed regarding the impact of the increase in microencapsulated PCM percentage on variation in hysteresis models' predictions. The chapter opens with the adopted methodology, presents and discusses the results, and finishes with a summary. This chapter is published in the journal article https://doi.org/10.1016/j.jobe.2023.108362 [102].

6.1. Hysteresis effect and modelling

6.1.1. Governing equations

Numerical analysis was carried out using a finite volume method within ANSYS Fluent to solve the energy equation that describes heat transfer with phase change. A source term (S_E) is added to

simulate the latent energy in PCM with hysteresis effect and can be described as a function of the liquid fraction, as shown by the following Equations.

$$\rho C_{P,s} \frac{\partial T}{\partial t} = \nabla \cdot (k \nabla T) + S_E \qquad (6.1)$$

$$S_E = -\rho \frac{\partial h_l}{\partial t} = -\rho L \frac{\partial \beta}{\partial t} \qquad (6.2)$$

Where ρ is the material density, k is the thermal conductivity, $C_{P,s}$ is the sensible specific heat capacity, S_E is the source term, L is the total latent energy of the PCM, β is the PCM liquid fraction, and h_l is the specific latent enthalpy due to phase change ($h_l = \beta L$). The model is completed by specifying the functional variation of the liquid fraction with temperature during the melting and freezing processes. A hysteresis model provides a method for determining the liquid fraction based on enthalpy variation with temperature for both the melting and freezing paths.

6.1.2. Hysteresis models

6.1.2.1. Generic Hysteresis Behaviour

Figure 6.1 shows the typical liquid fraction profiles for the PCM for complete phase change cycles. The melting process follows path 1-2-3-4, whereas the freezing process follows path 4-5-6-1.

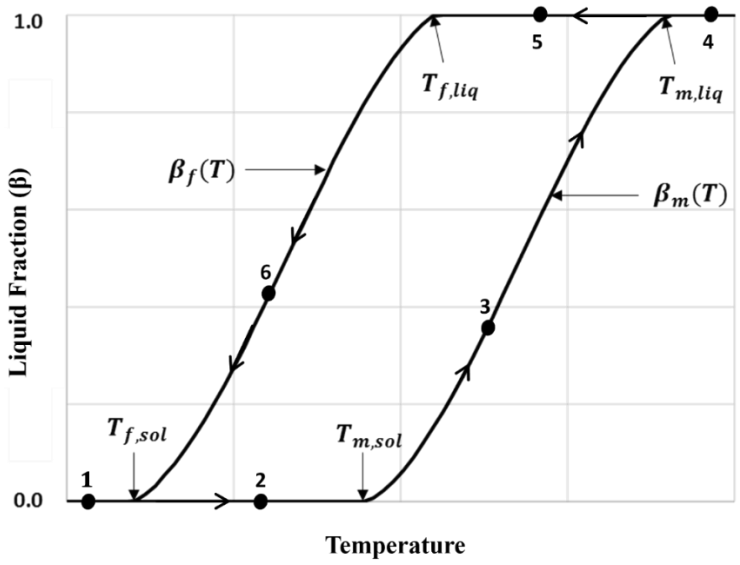

Figure 6.1. Typical behaviour (liquid fraction vs. temperature) for a PCM showing complete melting and freezing phase change cycles with hysteresis.

The temperature change with time determines whether the process is on the melting or freezing curve, as shown in Equations ((6.3) and ((6.4):

$$\beta(T) = \beta_m(T), \quad h(T) = h_m(T), \quad \text{if } \frac{dT}{dt} \geq 0 \text{ (Path 1-2-3-4)} \qquad (6.3)$$

$$\beta(T) = \beta_f(T), \quad h(T) = h_f(T), \quad \text{if } \frac{dT}{dt} < 0 \text{ (Path 4-5-6-1)} \qquad (6.4)$$

Where $\beta_m(T)$ and $h_m(T)$ are the liquid fraction and enthalpy profiles of the melting curve, $\beta_f(T)$, and $h_f(T)$ are the liquid fraction and enthalpy profiles of the freezing curve.

In realistic applications involving PCM integration in the building envelope materials, the PCMs may experience incomplete melting and freezing cycles because the random weather conditions often result in partial charging or discharging of the PCM [16, 106]. Hence, the hysteresis model should account for the latent energy and the hysteresis effect accompanied by incomplete phase change processes. Three established hysteresis models were introduced by [177] and are referred to as the Switch model [17], the Scale model [103], and the Track model [103]. Those three models and the new model (MScale) are described below.

6.1.2.2. The Track Model

In the Track model [103, 104], no transition occurs between melting and freezing curves in the interrupted phase change. Hence, if the heating process on the melting curve is stopped within the phase change range and followed by a cooling process, the cooling process follows the same melting curve with no transition to the freezing curve, as shown in Figure 6.2. In addition, if the freezing process on the freezing curve is stopped within the phase change range and followed by a heating process, the heating process follows the same freezing curve with no transition to the melting curve. Thus, the main drawback of the Track model is that, in interrupted phase change processes, the Track model behaves like a no-hysteresis case, and the transition between the curves only occurs for complete phase change cycles. In a partial phase change process, the Track model accounts for the change in liquid fraction but on the same phase change curve (i.e., no transition between curves).

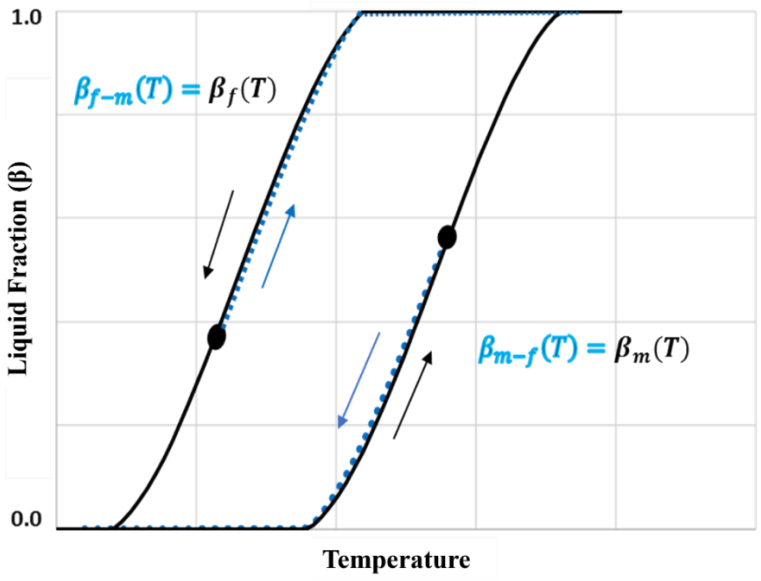

Figure 6.2. Illustration for the Track model. $\beta_{m-f}(T)$ is the path followed for freezing after interrupted melting and $\beta_{f-m}(T)$ is the path followed for melting after interrupted freezing.

6.1.2.3. The Switch Model

In the Switch model [177, 178], a transition occurs between melting and freezing curves in interrupted phase change processes following a constant liquid fraction line. Hence, if the heating process on the melting curve is stopped within the phase change range and followed by a cooling process, the cooling process follows a constant liquid fraction line until it hits the freezing curve, and then cooling continues with lowering liquid fraction on the freezing curve, as shown in Figure 6.3. In addition, if the freezing process on the freezing curve is stopped within the phase change range and followed by a heating process, the heating process follows a constant liquid fraction line until it hits the melting curve, and then heating continues with an increasing liquid fraction on the melting curve, as shown in Figure 6.3. The transition with a constant liquid fraction line assumes that the PCM thermal storage remains only sensible during the transition process between the curves.

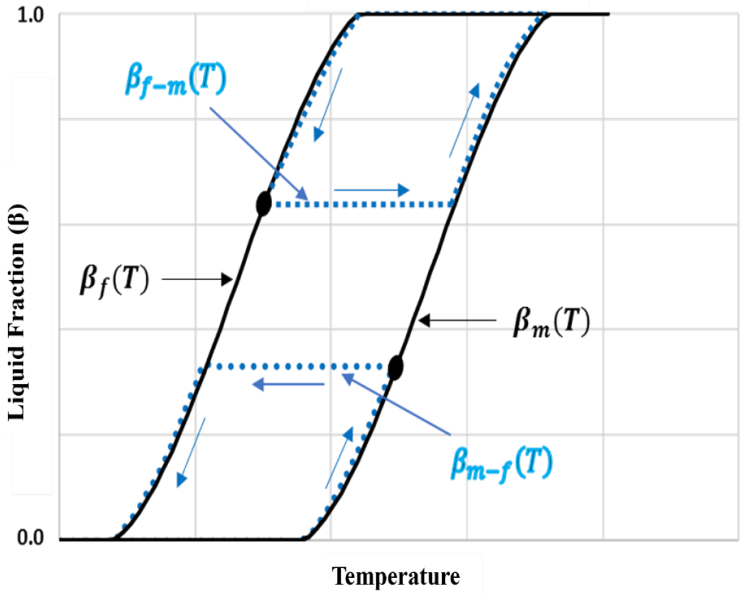

Figure 6.3. Illustration for the Switch model. $\beta_{m-f}(T)$ is the path followed for freezing after interrupted melting and $\beta_{f-m}(T)$ is the path followed for melting after interrupted freezing.

6.1.2.4. The Scale Model

Previous studies [17, 106] slightly improved the Switch model by generating the transition paths by mathematically scaling the melting and freezing curves (i.e., the curves of complete phase change processes). However, the resultant transition paths still had a portion following a constant liquid fraction line, having the identical drawback and limitation as the Switch model, as shown in Figure 6.4.

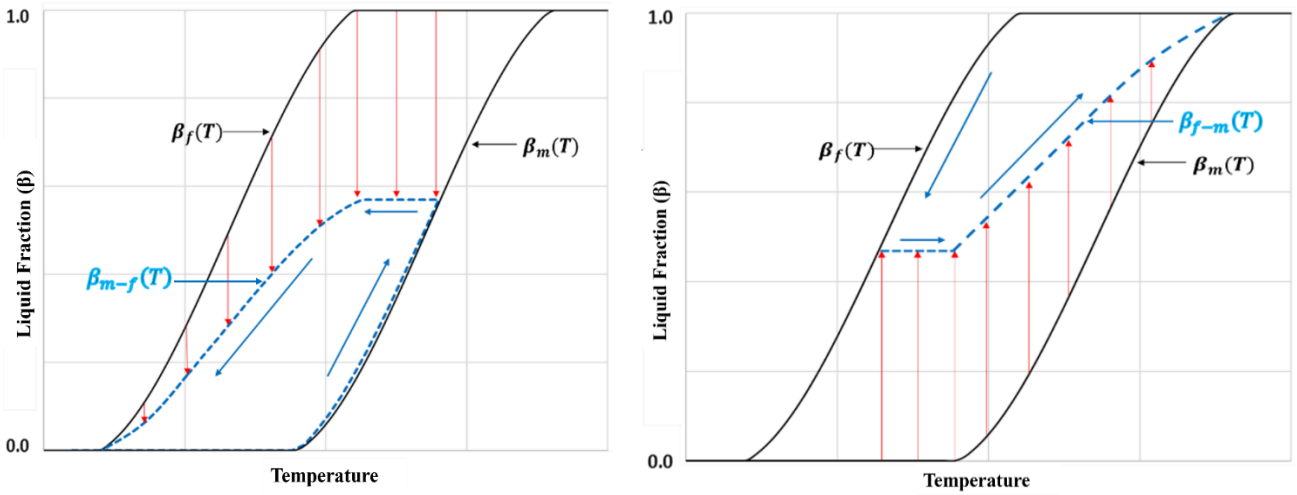

a) transition from melting to freezing.

b) transition from freezing to melting

Figure 6.4. Illustration for the Scale model: (a) transition from melting to freezing, (b) transition from freezing to melting. $\beta_{m-f}(T)$ is the path followed for freezing after interrupted melting and $\beta_{f-m}(T)$ is the path followed for melting after interrupted freezing.

6.1.2.5. The MScale Model

Considering the limitations of the three existing hysteresis models, an improved model should allow changing liquid fraction and transition between the melting and freezing curves to accurately capture the complex phase change phenomena observed in experimental studies [105, 176, 178, 179]. The new Modified Scale hysteresis model uses the mathematical scaling technique presented in [17], allowing for a transition between melting and freezing curves in interrupted phase change processes (unlike the Track model). In addition, the transition process does not follow a constant

liquid fraction line (unlike the Switch and Scale models). The innovative feature of this model is the use of a middle hysteresis curve ($\beta_{hyst}(T)$) to create the transition curves, as shown in Figure 6.5. The use of ($\beta_{hyst}(T)$) eliminates the assumption of constant liquid fraction in the Switch and Scale models, and the assumption that the liquid fraction changes with no regard for the hysteresis effect in the Track model. The following Equations generate the liquid fraction for the interrupted phase change paths in Figure 6.5:

$$\beta_{m-f}(T) = \frac{\beta_m(T_o)}{\beta_{hyst}(T_o)}\beta_{hyst}(T), \tag{6.5}$$

$$\beta_{f-m}(T) = 1 - \frac{1-\beta_f(T_o)}{1-\beta_{hyst}(T_o)}(1-\beta_{hyst}(T)), \tag{6.6}$$

Where T_o is the initial temperature at the point of the interruption from heating to cooling (and vice versa), $\beta_m(T_o)$ is the liquid fraction at T_o on the melting curve, $\beta_f(T_o)$ is the liquid fraction at T_o on the freezing curve, $\beta_{m\text{-}f}(T)$ is the liquid fraction profile for the transition from melting to the freezing process, $\beta_{f\text{-}m}(T)$ is the liquid fraction profile for the transition from freezing to melting process, and $\beta_{hyst}(T_o)$ is the liquid fraction at T_o on the middle hysteresis curve, as shown in Figure 6.5.

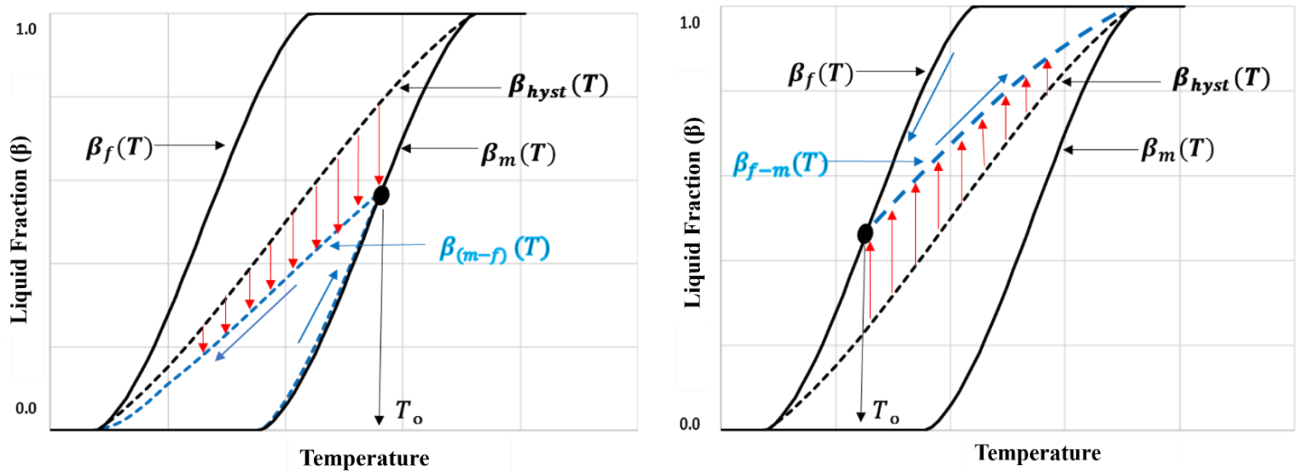

a) transition from melting to freezing. b) transition from freezing to melting.

Figure 6.5. Illustration for the Modified Scale hysteresis model in incomplete phase change processes: (a) transition from melting to freezing, (b) transition from freezing to melting.

6.1.2.6. Example of the hysteresis model behaviour

An example of the transition methods in the four hysteresis models in interrupted phase change is presented in Figure 6.6. The flowcharts for all models are shown in Appendix C, and the liquid fraction was calculated by applying the test temperature profile shown in Figure 6.6a to demonstrate the different behaviours of the four hysteresis models. The PCM used for this test was a microencapsulated PCM product (Nextek 18D), which has ~18°C phase change temperature, 15-30 µm particle size, 300-400 kg/m^3 bulk density, and ≥190 J/g heat of fusion [168]. Table 6.1 provides the effective enthalpy equations of hempcrete material infill with 9% MPCM obtained from previous experimental research (Chapter 5). The enthalpy profiles are obtained by integrating the specific heat profiles, with the melting and freezing curves assumed to be identical to the average curve profile between them (Section (5.4.3)).

Table 6.1. Temperatures (T_{sol}, T_{liq}) and enthalpy equations for the H-Micro composite.

	T_{sol} (°C/K)	T_{liq} (°C/K)	$h(T)$ (J/kg), (T in kelvin)
Melting curve	14/287	23/296	(-46.1) T^3 + (40320.5) T^2 - (11748844.5) T + 1140743636.8
Freezing curve	7/280	16/289	(-46.1) T^3 + (39352.3) T^2 - (11191134.3) T + 1060449018.1
Middle hysteresis curve	7/280	23/296	(-8.2) T^3 + (7090.03) T^2 - (2038553.4) T + 195088425

*The amount of hysteresis = 7°C.

For this MPCM, the input test temperature profile in Figure 6a contains two interrupted phase change points (Points 2 and 3). The liquid fraction was calculated using the following Equations:

$$\beta = 0, \qquad T \leq T_{sol} \qquad (6.7)$$

$$\beta = 1, \qquad T \geq T_{liq} \qquad (6.8)$$

$$\beta(T) = \frac{h(T) - h_{Tsol}}{h_{Tliq} - h_{Tsol}}, \qquad T_{liq} > T > T_{sol} \qquad (6.9)$$

Where T_{sol} is the solidus temperature (at β=0), T_{liq} is the liquidus temperature (at β=1), h_{Tsol} is the enthalpy at T_{sol}, h_{Tliq} is the enthalpy at T_{liq}, and $h(T)$ is the enthalpy as a function of the

temperature inside the phase change range (between *Tsol* and T_{liq}). The resulting liquid fraction variations for the hysteresis models are presented in Figure 6.6b and Figure 6.6c.

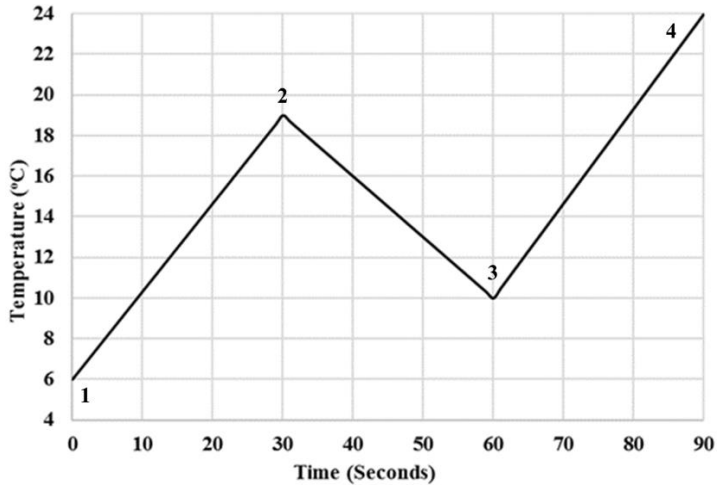

a) Input test temperature profile.

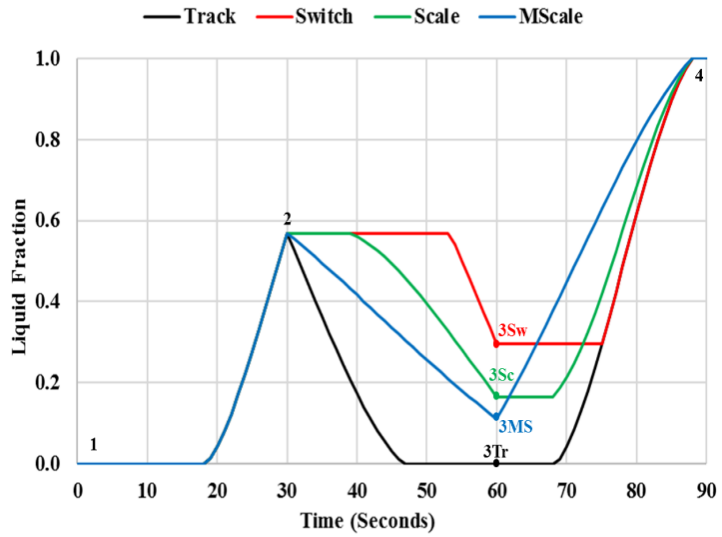

b) Liquid fraction variation with time.

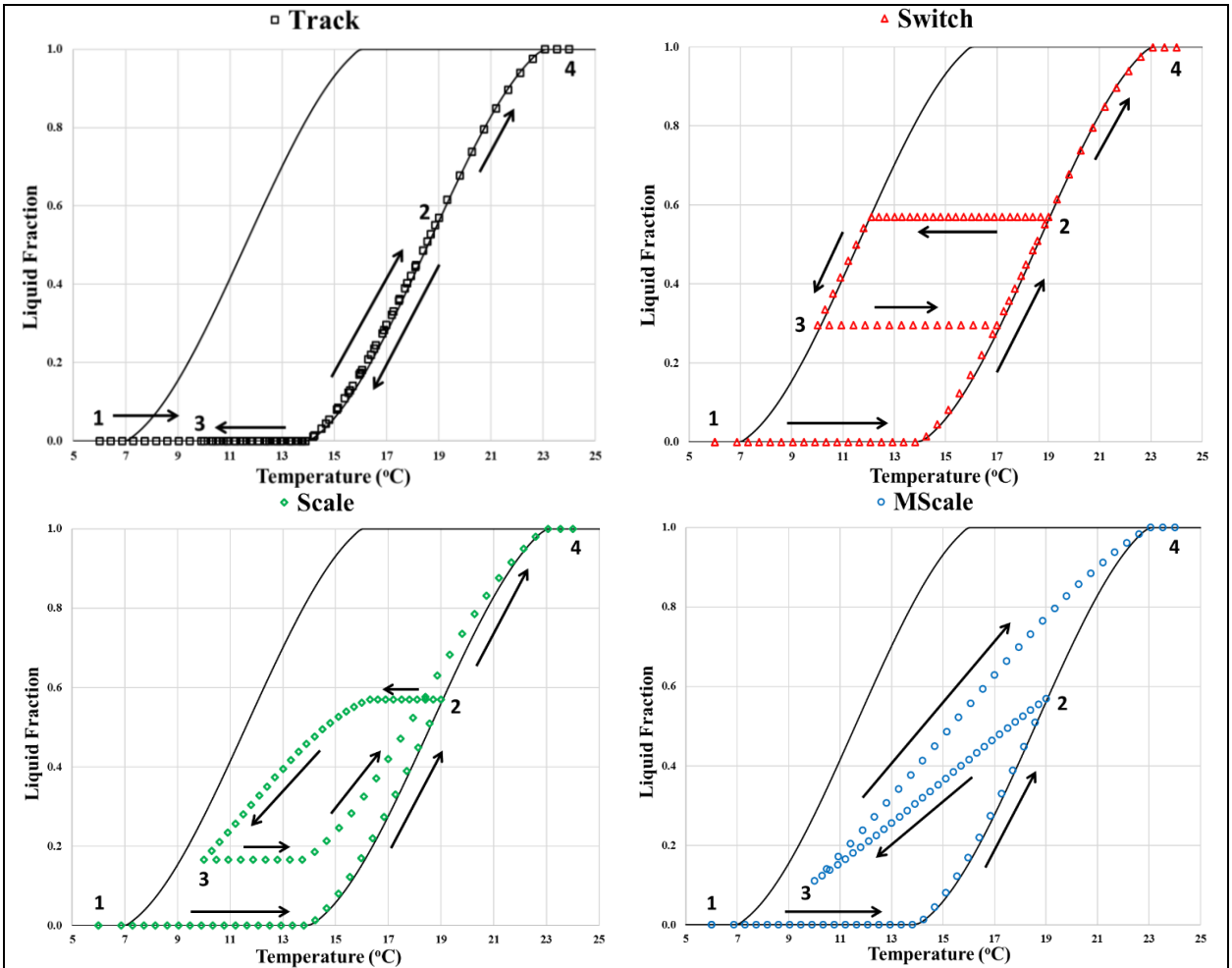

c) Liquid fraction versus temperature paths for the four hysteresis models.

Figure 6.6. Comparison between the hysteresis models.

Figure 6.6c shows that, at Point 2, the Track model follows the same melting curve for the cooling process with no account for the hysteresis effect, which results in the fastest time to reach zero liquid fraction and the lowest liquid fraction at Point 3, as shown in Figure 6.6b. At Point 2, the Switch model allows the transition from the melting to the freezing curve by following a constant liquid fraction path, and the liquid fraction decreases again only after reaching the freezing curve, resulting in the highest liquid fraction at Point 3. The Scale model allows the transition from the melting to freezing curve with a constant liquid fraction path (like the Switch model) until reaching the liquidus temperature of the freezing curve, then follows a transition path by scaling the freezing

curve, resulting in slightly lower liquid fraction values than the Switch model but higher than the Track model. The MScale model follows a transition path between the Scale and Track models from Point 2 to Point 3, after which it becomes the highest liquid fraction in its path towards Point 4. The MScale model allows the curve transition to account for the hysteresis effect by changing the liquid fraction.

6.1.3. Numerical Solution Method

The numerical solution of the governing equation for temperature using a finite volume method was obtained using commercial CFD software ANSYS Fluent (Release 19.2). User-defined functions (UDF) were created to implement the source term in Equation (6.2) for the four hysteresis models with the algorithms given in the flow charts in Appendix C. This study used the Least Squares Cell-Based Gradient Evaluation method to calculate solution variable gradients and a second-order transient approach. The discretized temperature equations' computations were performed with 200 iterations per time step. Calculations were carried out using double precision, and solutions at a time step typically had a root mean square of the normalized residual less than 1×10^{-6}.

6.1.4. Test case definitions

Three test cases are investigated in this section:

1) Test case 1: Comparison and validation of hysteresis models against experimental results.

2) Test case 2: The effect of hysteresis models (Track, Switch, Scale, MScale) on the thermal performance of hempcrete walls integrated with Panel PCM layer (H-Panel wall) and microencapsulated PCM (H-Micro wall).

3) Test case 3: The effect of PCM percentage on the performance of the hysteresis models in the H-Micro wall.

6.1.4.1. Test Case 1: Validation of the hysteresis models

Confidence in the numerical modelling of PCM hysteresis requires validation against experimental results. In this regard, the hysteresis models are compared with the experimental results presented in [105], in which researchers applied a temperature step change for both heating and cooling modes on a PCM product and measured the temperature change of the PCM to observe the hysteresis behaviour in interrupted phase change processes [105]. The domain in Figure 6.7, with the material properties in Table 6.2, was used for this test case. Adiabatic boundary conditions were assumed at the left and right boundaries.

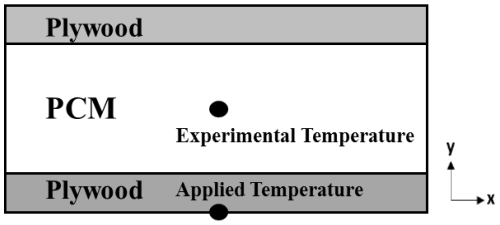

Figure 6.7. PCM-equipped wall model.

Table 6.2. Layers properties.

	Thickness (m)	Thermal conductivity (W/m K)	Density (kg/m³)	Energy storage features
PCM effective properties	0.017	0.042	223	The average latent heat ~ 151 (J/g) The average hysteresis ~ 6.5 (°C)
Plywood wall boards	0.006	0.084	850	Specific heat capacity = 1.25 (J/kg K)

At the start of the computation, the domain temperature was uniformly set at 5.5°C for the interrupted heating test and 26°C for the interrupted cooling test. A suitable temperature trend, presented later in Section 6.2.1, was applied uniformly to the outer surface of the plywood layers. The MScale hysteresis model was used to examine the grid dependence. The grid was selected by varying the mesh size from 5 to 20 nodes in the *x* direction and from 4 to 18 nodes in the *y* direction. An acceptably small change of 0.12 K in the center temperature from the next finest mesh was obtained with a 10 by 9 (N_x by N_y) mesh. Furthermore, a difference of 0.1 K for the center

temperature was found when using one or two minutes as a time step, so the time step size was set as two minutes. Repeating these tests using the other hysteresis models yielded even smaller differences.

6.1.4.2. Test Case 2: Comparison of hysteresis models in two integration methods

Numerical simulations compared the performance of the four hysteresis models applied to two hempcrete wall assemblies enhanced with PCM using the two most widely integrating methods: microencapsulation and macroencapsulation. Figure 6.8 illustrates the cross sections of the two walls developed in ANSYS Design Modeler, including 1) a wall with 30 cm of hempcrete infill with microencapsulated PCM (H- Micro) and 2) a wall with 30 cm of hempcrete infill and a panel of 1 cm PCM (H-Panel) placed on the internal side. The properties of the common building materials, such as gypsum, wood (3.8 cm x 14 cm), and cement lime plaster, are obtained from the WUFI software library (see Table 5.3). The thermal properties of the panel PCM (PureTemp 18) and the differential scanning calorimetry (DSC) curves are obtained from the manufacturer (PureTemp). The commercial PCM (PureTemp 18) is a thermally stable product, with ~18 ^{o}C phase change temperature and 192 J/g heat storage capacity [180]. Our experimental study (Chapters 4 & 5) obtained the effective thermal properties of hempcrete and H-Micro infills. The hempcrete material consisted of hemp hurd, binder (50% hydrated lime and 50% metakaolin by weight), and water at the ratio of 1:1:3 by weight [111]. Because of the high cost of microencapsulated phase change material, its negative impact on the mechanical properties, and its hindering effect on energy savings when used in higher percentages, the PCM percentage was limited to ~9% by weight in both wall types.

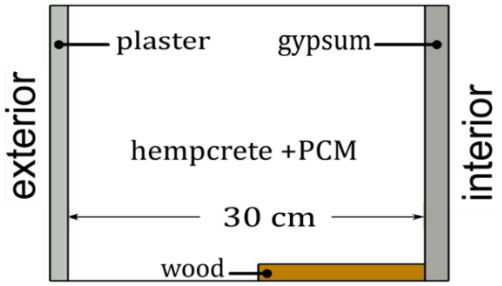

a) **H-Micro** (hempcrete + microencapsulated PCM)

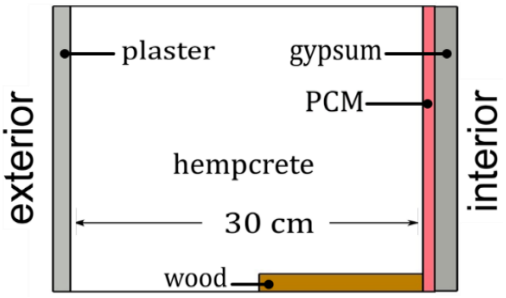

b) **H-Panel** (hempcrete + PCM panel layer)

Figure 6.8. Wall geometry and design configurations.

Convection conditions were specified on both vertical (interior and exterior) surfaces. Symmetry boundary conditions were applied at the stud and cavity centerlines. The model does not consider the interfaces and corners between walls, solar gains through windows, internal loads, and radiation exchange between interior surfaces. Table 5.4 provides the details of the boundary conditions. The two walls were simulated for weather conditions (external boundary conditions) in Winnipeg, Canada. Winnipeg experiences temperature differences between summer and winter of more than 60 °C. Winters are long and extremely cold, with average outdoor air temperatures ranging from −5 °C to −20 °C, and summers are short and warm, with average outdoor air temperatures ranging from 5 °C to 25 °C. The city also has relatively low evening and night temperatures, averaging approximately 15 °C during the three warmest summer months. As a result, the predominant energy use in buildings is heating. Therefore, this study investigated the performance of the two walls for January as the coldest month (the worst-case scenario) and the highest energy consumption month. The inner schedule applies a heating setpoint of 20 ^{o}C, fixed for the entire day at this stage for simplicity (i.e., no difference between active and dormant hours). Figure 6.9 shows the weather boundary conditions for January. The data regarding solar irradiance, outdoor temperature, and wind speed were collected from the Canadian Weather for Energy Calculations file, composed of hourly weather data records selected from a 30-year database for

Winnipeg, and then elaborated through the building modelling tool EnergyPlus to generate suitable values for a south wall orientation. The external and internal convective heat transfer coefficients were calculated using the Liu and Harris (2015) model [169] and the Awbi and Hatton (1999) model [171].

The initial condition for the computations corresponds to the steady-state solution determined using the boundary conditions for the start of January with no solar flux: the exterior and interior surface temperatures were 13 °C and 20 °C, respectively, while the convection heat transfer coefficients are 17.5 W/m^2K (outer side) and 3 W/m^2K (inner side). The total energy use resulting from the simulations with 723518, 1146750, and 1920000 nodes were compared, and a difference of 0.03% was found between the results using medium and fine grids. Several different time steps (5, 15, and 30 minutes) were also tested, and a difference of 0.04% in the total heating energy consumption was found between the results using the two smaller time steps. These comparisons used the MScale model; no higher differences were found using the other hysteresis models. Therefore, the model used a grid of 1146750 elements and a time step size of 15 minutes with 200 iterations per time step.

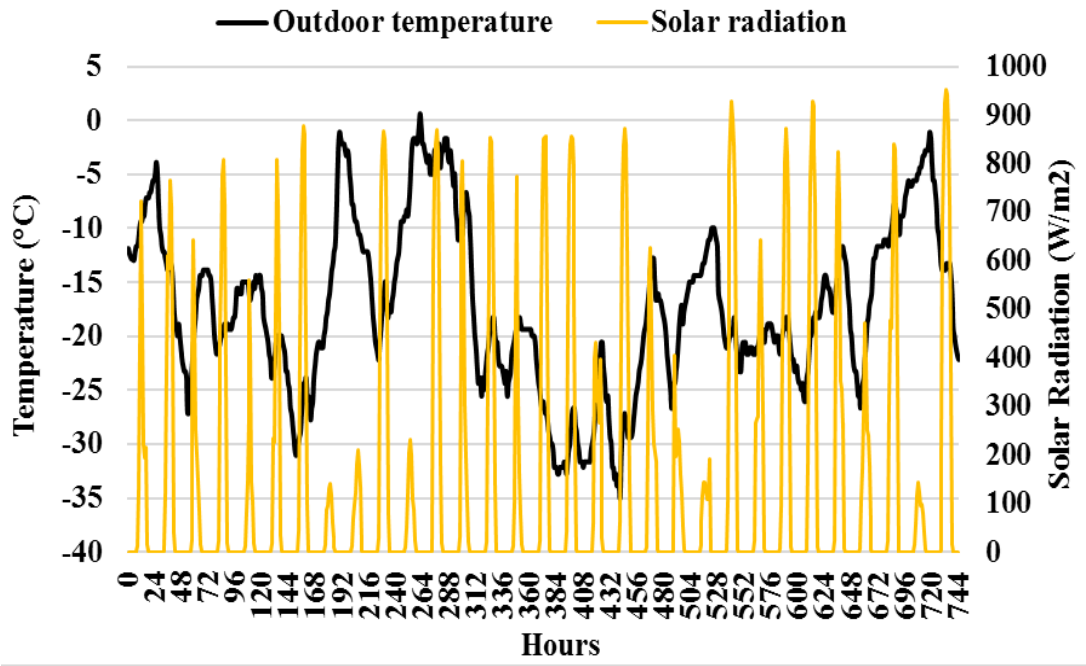

a) solar radiation and outdoor temperature.

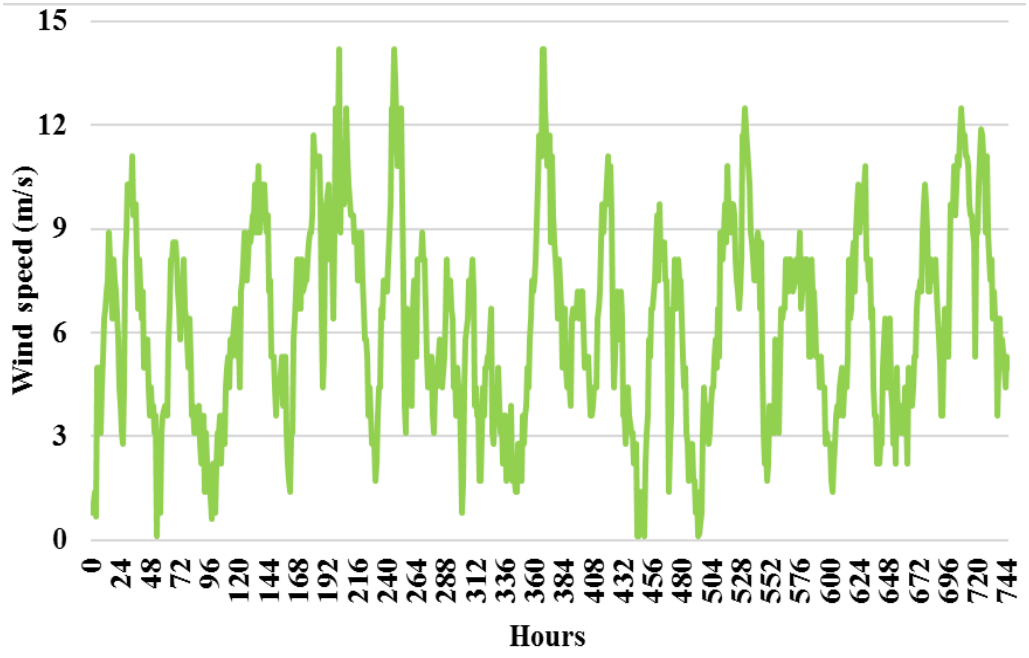

b) wind speed.

Figure 6.9. Weather boundary conditions in January: a) solar radiation and outdoor temperature; b) wind speed.

6.1.4.3. Test Case 3: Effect of microencapsulated PCM percentage

In this test case, numerical modelling is performed to investigate the sensitivity of the four hysteresis models regarding the increase of microencapsulated PCM from 9% to 27% and 45% in the H-Micro walls. The density, thermal conductivity, and sensible specific heat capacity are assumed to be equivalent to H-Micro 9%, with only the latent heat assumed to change. Although these assumptions bring a certain idealization, they allowed us to investigate the impact of the increase in latent heat on the hysteresis behaviour. The temperature ranges and hysteresis amount are assumed to be the same as H-Micro 9%. The resultant effective enthalpy equations for H-Micro 27% and H-Micro 45% are presented in Table 6.3, whereas the enthalpy equations of H-Micro 9% are presented in Table 6.1.

Table 6.3. Enthalpy equations for the H-Micro composites.

Sample	Curve	*h(T)* (J/kg), (T in kelvin)
H-Micro 27%	Melting curve	$(-138.3)\ T^3 + (120961.7)\ T^2 - (35250133.6)\ T + 3423213710.3$
	Freezing curve	$(-138.3)\ T^3 + (118056.9)\ T^2 - (33577002.9)\ T + 3182329854.3$
	Middle curve	$(-24.6)\ T^3 + (21270.1)\ T^2 - (6119260.3)\ T + 586248075.0$
H-Micro 45%	Melting curve	$(-230.5)\ T^3 + (201602.8)\ T^2 - (58751422.7)\ T + 5705683783.9$
	Freezing curve	$(-230.5)\ T^3 + (196761.6)\ T^2 - (55962871.6)\ T + 5304210690.5$
	Middle curve	$(-41.0)\ T^3 + (35450.2)\ T^2 - (10199967.2)\ T + 977407725.0$

6.2. Results

6.2.1. Test Case 1: Validation of the hysteresis models

Figure 6.10 shows a very good agreement between the measured experimental temperatures and those predicted with the MScale model. The results illustrate that, after the interruption in the heating/cooling process, the temperature rate of change (dT/dt) is high in the Switch model, which can be attributed to the constant liquid fraction and the sensible behaviour in the transition between the melting and freezing curves (i.e., the amount of energy required to change the temperature is relatively low). However, the temperature rate of change becomes low again after the transition is

complete to the other phase change curve, and the liquid fraction changes due to the latent behaviour of the PCM (i.e., the amount of energy required to change the temperature is relatively high). The Scale model follows the same behaviour as the Switch model but with a slightly shorter constant liquid fraction path. In contrast, the Track model exhibits a lower rate of temperature change after the interruption in the heating/cooling process due to the latent behaviour of the PCM and the changing liquid fraction while being on the same phase change curve (no transition). Then, the temperature rate of change increases again when the liquid fraction becomes zero, and there is no further phase change. The MScale model shows the closest temperature profile compared to the experimental results. The actual temperature change rate for the experimental and MScale cases is between the Switch/Scale and Track models.

In the interrupted heating case, the maximum difference in the temperature values between the experimental results and the MScale model is approximately 1 K, compared to 2 K in the Track model, 3.6 K in the Switch model, and 3.1 K in the Scale model. Instead, in the interrupted cooling case, the approximate maximum differences in the temperature values between the experimental results and the MScale model are 1 K, compared to 4.5 K in the Track model, 2.1 K in the Switch model, and 1.6 K in the Scale model. Table 6.4 shows the root mean square difference (RMSD) and the normalised root mean square difference (CV(RMSD) between the hysteresis models and the experimental case. In the interrupted heating case, the MScale model shows lower (RMSD) values than the Track, Switch, and Scale models by approximately 21%, 53%, and 45%, respectively. In the interrupted cooling case, the MScale model shows lower (RMSD) values than the Track, Switch, and Scale models by nearly 77%, 53%, and 34%, respectively.

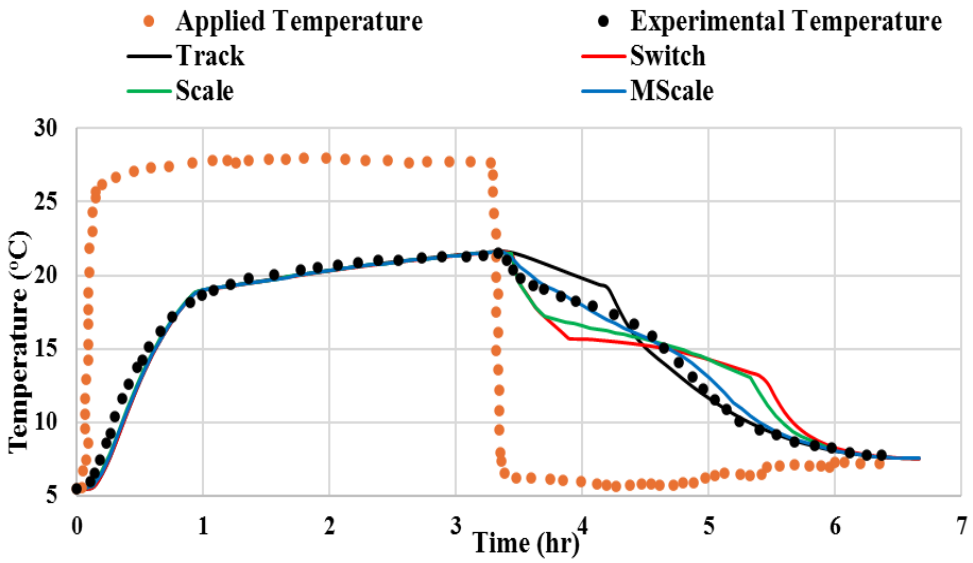

a) Interrupted heating.

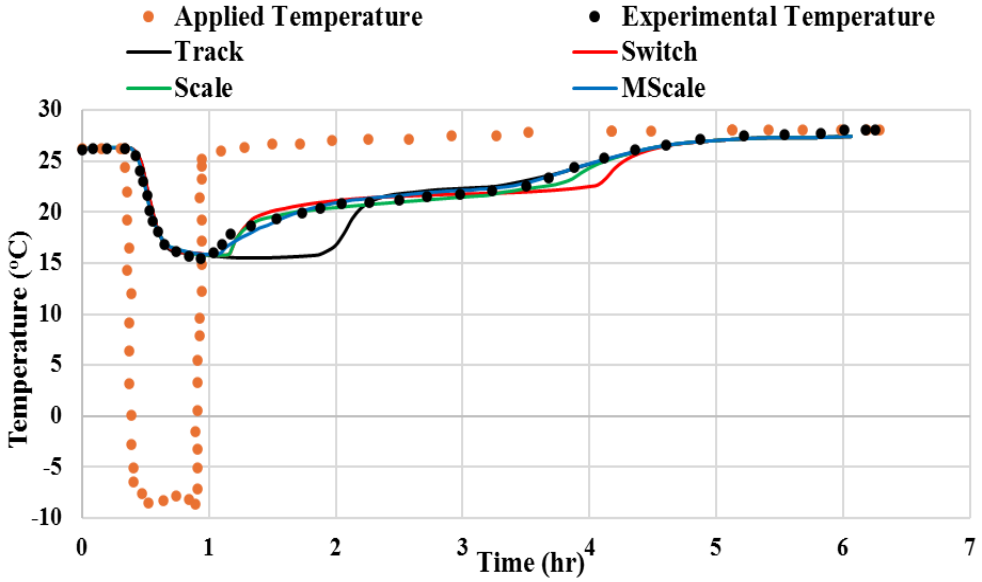

b) Interrupted cooling.

Figure 6.10. Validation and comparison of the hysteresis models with the experimental results: a) Interrupted heating; b) Interrupted cooling.

Table 6.4: The difference between the hysteresis models and the experimental case.

	Interrupted heating				Interrupted cooling			
	Track	Switch	Scale	MScale	Track	Switch	Scale	MScale
Root mean square difference (RMSD)	0.80 K	1.33 K	1.14 K	0.63 K	1.44 K	0.70 K	0.50 K	0.33 K
Coefficient of variation of RMSD (CV(RMSD)) %	5.28	8.81	7.47	4.17	6.51	3.15	2.18	1.48

6.2.2. Test Case 2: Comparison of hysteresis models in two PCM integration methods

The performance of each of the four hysteresis models (Track, Switch, Scale, MScale) for the two types of walls with microencapsulated and panel PCM was assessed by investigating and comparing the time trends of thermal energy transferred by the walls, liquid fractions, and inner temperatures. The energy consumption (Wh/m^2) is calculated by integrating the heat flux data (W/m^2) over time at the inner wall surface and represents the heat loss from the wall that has to be compensated to keep the inner schedule applied. The fluctuation characteristics (fluctuation ratio and coefficient of variation) provided insights into each model's energy curve.

6.2.2.1. Energy Consumption Analysis

Table 6.5 presents January's total energy use for the two cases of panel PCM and microencapsulated PCM walls. It is important to note that there is no difference between the no-hysteresis case and the Track hysteresis model in the case of interrupted melting and solidification for the reasons explained in the methods section (see Figure 6.2 and Figure 6.6). The overall findings show that the impact of the hysteresis is more significant for the panel PCM wall (H-Panel) than the microencapsulated PCM wall (H-Micro). At the same time, the Switch, Scale, and MScale models consider the hysteresis effect in the interrupted melting and solidification processes, predicting higher energy consumption compared to the no-hysteresis/Track model.

Thus, for the H-Panel wall, the energy consumption percentage differences between the Switch, Scale, and MScale models compared to the no-hysteresis/Track model are 0.28%, 0.63%, and 1.24%, respectively, while in the case of the H-Micro wall, the differences of 0.19%, 0.27%, and 0.49%, respectively are 30-60% smaller. These results suggest that neglecting the hysteresis phenomenon in modelling PCM, primarily bulk PCMs, can slightly overestimate the energy savings from integrating PCM materials into the building envelope. Table 6.5 also shows that the H-Micro walls have approximately 8.36% lower energy consumption than the H-Panel walls. The possible reason is the increased thermal resistance of the hempcrete wall with MPCMs integrated across its entire thickness (as shown in Chapter 5, adding 9% of MPCM to a hempcrete mixture reduced its thermal conductivity by approximately 9%). On the other hand, adding a 1 cm thin layer of PCM (higher conductivity than hempcrete and gypsum) on the inside surface of the hempcrete does not increase the H-Panel wall thermal resistance enough to match that of the H-Micro wall.

Table 6.5. Heating energy consumption for the two walls in January.

	H-Panel				**H-Micro**			
	No-hysteresis/ Track	Switch	Scale	MScale	No-hysteresis/ Track	Switch	Scale	MScale
Energy Consumption (Wh/m^2)	7589	7610	7637	7683	6974	6987	6993	7008
Percentage difference with the no-hysteresis case.	---	0.28%	0.63%	1.24%	---	0.19%	0.27%	0.49%

Figure 6.11 compares the hourly energy consumptions for both wall types in January to further understand the impact of hysteresis on the heating energy predictions of the Track, Switch, Scale, and MScale models. As shown, for the H-Panel wall, the hourly energy consumption difference

between the hysteresis models is more significant than in the H-Micro wall case, further demonstrating the lower sensitivity to the type of hysteresis model in the H-Micro wall than the H-Panel wall. For instance, for the H-Panel wall, the difference in daily averaged energy consumption on Jan 19 between the Switch, Scale, and MScale models compared to the no-hysteresis/Track model is 8.4%, 8.2%, and 7.9%, respectively. In contrast, these differences between the Switch, Scale, and MScale models compared to the no-hysteresis/Track model for the H-Micro wall are only 0.12%, 0.10%, and 0.06%, respectively, on the same day. Figure 6.11 also illustrates that both walls' Switch and Scale models exhibit more significant fluctuations than the Track and MScale models. The monthly averaged fluctuation ratio is calculated to quantify these differences and is reported in Table 6.6.

Table 6.6 also summarises the normalised root mean square difference (CV(RMSD)) between the Switch, Scale, and MScale models compared to the no-hysteresis/Track model to enable quantifying the differences between the four models throughout the entire month. The H-Panel wall has normalised RMSD values of 10.68%, 9.95%, and 6.41% for the Switch, Scale, and MScale models. The H-Micro wall values are approximately 86%, 86%, and 82% lower. In addition, for the H-Panel wall, the Switch and Scale models show a more significant difference with the no-hysteresis/Track model than the MScale model by approximately 4.27% and 3.54%, respectively. Regarding the H-Micro wall, the Switch and Scale models differ from the no-hysteresis/Track and the MScale models by only 0.38% and 0.22%, respectively. These results further demonstrate lower energy sensitivity to the hysteresis model in the H-Micro wall than in the H-Panel case.

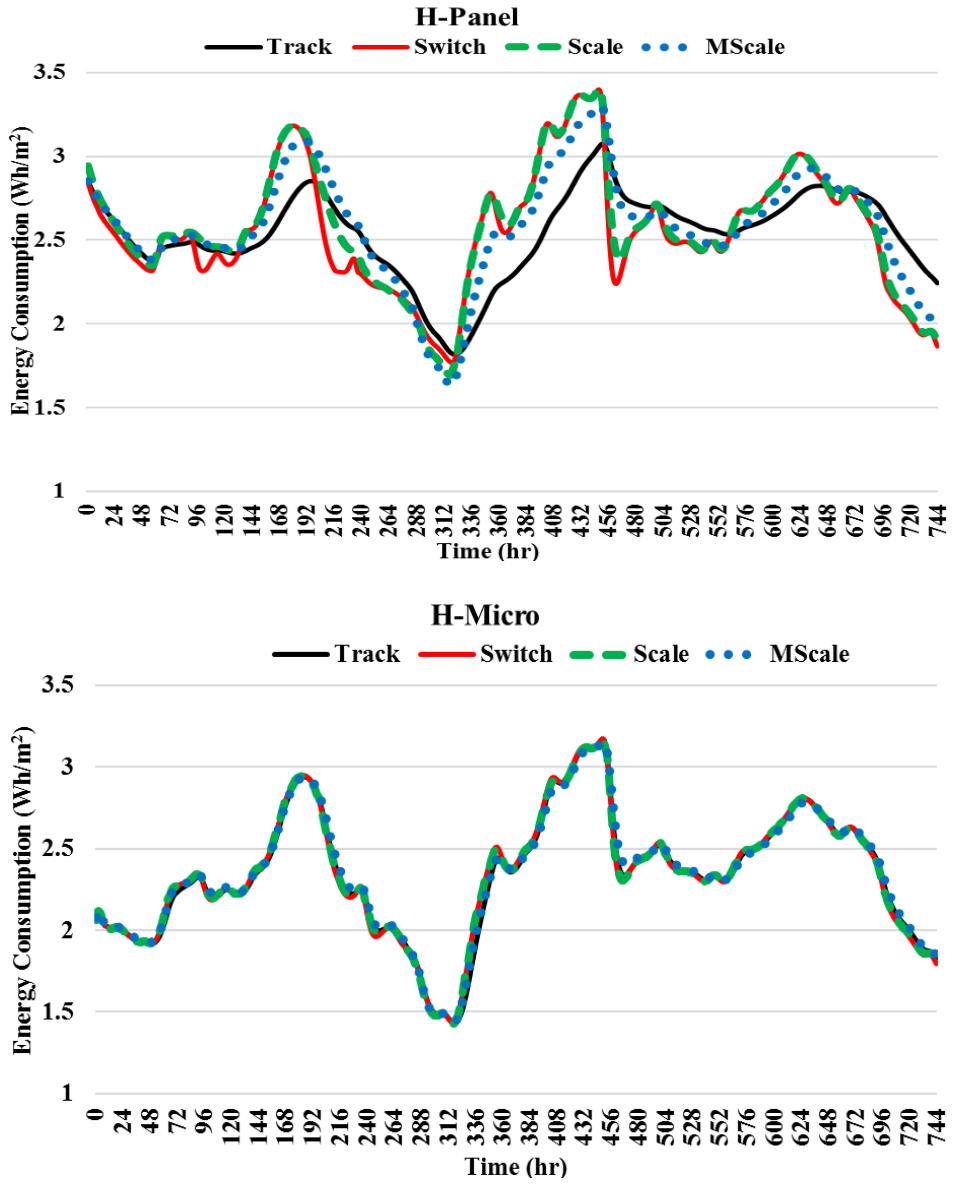

Figure 6.11. The heating energy consumption in January for the four hysteresis models in both walls: (a) H-Panel wall, (b) H-Micro wall.

Table 6.6. The normalized root mean square difference and fluctuation characteristics of the energy consumption.

	H-Panel				**H-Micro**			
	Track	Switch	Scale	MScale	Track	Switch	Scale	MScale
Coefficient of variation of the RMSD (CV(RMSD)) %	--	10.68	9.95	6.41	--	1.51	1.35	1.13
Fluctuation ratio % $((E_{Max}-E_{Min})/E_{Avg})$	6.09	10.43	10.35	8.47	10.14	10.49	10.36	9.85
Coefficient of variation (CV) %	1.80	3.25	3.14	2.54	3.03	3.15	3.12	2.97

Additionally, the monthly averaged coefficient of variation (CV) summarized in Table 6.6 presents the dispersion level of the energy consumption values. In the H-Panel wall, the fluctuation ratio of the Switch model is much higher than with the other models, except for the slight difference with the Scale model, whereas the difference is minimal for the H-Micro wall. These results indicate that the Switch and Scale models induce higher and lower peaks (wider range) than the no-hysteresis/Track and MScale models in both walls. The sensible transition (constant liquid fraction line) in the Switch and Scale models causes a lower energy storage capacity. On the contrary, the no-hysteresis/Track and MScale models, which exhibit higher liquid fraction fluctuations, show lower energy consumption fluctuation than the Switch and Scale models. The liquid fraction and inner temperature are analysed further to understand each hysteresis model's performance in both walls.

6.2.2.2. Liquid fraction analysis

Figure 6.12 presents the area-averaged hourly liquid fraction at the interior hempcrete surface according to the four hysteresis models in both wall configurations. Additionally, Table 6.7 summarizes the normalized root mean square differences for the hysteresis models compared to the no-hysteresis/Track model and the fluctuation ratio of the liquid fraction profiles. Figure 6.12 shows that the PCM undergoes incomplete phase change processes (partial charging and

discharging) for the entire month in both walls. In addition, the Switch and Scale models exhibit limited fluctuation of the liquid fraction profiles in both wall types: actually, they imply an almost constant liquid fraction throughout the month (except for a few hours on both walls). The likely reason is the sensible transition back and forth between the melting and freezing curves with constant liquid fraction values in the Switch and Scale models because the liquid fraction only changes after reaching the melting or freezing curves in the Switch model or after reaching the liquidus/solidus temperatures of the freezing/melting curves in the Scale model (as illustrated in Figure 6.3 and Figure 6.4).

Furthermore, the Track model shows a much higher fluctuation ratio than the other hysteresis models because of the change in the liquid fraction without transferring to another phase change curve to account for hysteresis. The MScale model has intermediate fluctuation ratios because the liquid fraction changes while transferring to another phase change curve. For example, as shown in Table 6.7, the Switch, Scale, and MScale fluctuation ratios for the H-Panel wall are around 92%, 88%, and 70% lower than the Track model. Similar values occur for the H-Micro wall. Figure 6.12 also illustrates that the difference in the liquid fraction profiles between the hysteresis models is more significant for the H-Panel wall than the H-Micro wall: indeed, the differences in the daily averaged liquid fraction for the H-Panel wall on January 19 between the Switch, Scale, and MScale models compared to the Track model are 0.534, 0.596, and 0.496, respectively, which is between 13% and 23% higher than their counterparts in the H-Micro wall. Table 6.7 also shows that the RMSD values for the Switch, Scale, and MScale models compared to the Track model in the H-Panel wall, are 0.30, 0.37, and 0.36, respectively, higher than their counterpart values in the H-Micro wall (0.258, 0.332 and 0269). Moreover, in the H-Panel wall, the normalised RMSD values of the Switch, Scale, and MScale models are approximately 72%, 89%, and 86%, respectively.

Their counterpart values in the H-Micro wall are 86%, 110.2%, and 90%, respectively, as shown in Table 6.7. These findings illustrate that the difference in liquid fraction values is higher in the H-Panel wall. Still, the normalized difference in liquid fraction values is higher in the H-Micro wall because of the lower average liquid fraction values. The likely reason for the lower average liquid fractions in the H-Micro wall is spreading the MPCMs across the entire wall thickness, which increases the effect of the cold outside weather on the PCM, resulting in lower average values of the liquid fraction in the H-Micro wall compared to the H-Panel wall, in which PCM layer is only in the inner surface.

Table 6.7 also shows that the fluctuation ratios and coefficient of variations are higher in the H-Micro wall than in the H-Panel wall for all hysteresis models. The likely reason for these findings is that applying a condensed thin PCM layer on the inner wall surface dampens the liquid fraction fluctuations (requires more energy to change) and isolates the effects of the outdoor weather variations on the inner conditions. In contrast, incorporating MPCMs across the entire wall thickness lowers the dampening effect (requiring less change energy). It makes the H-Micro more susceptible to variations in the outside weather, which also explains the higher fluctuation ratios of the heating energy consumption in the H-Micro wall than in the H-Panel wall, as shown in Table 6.6.

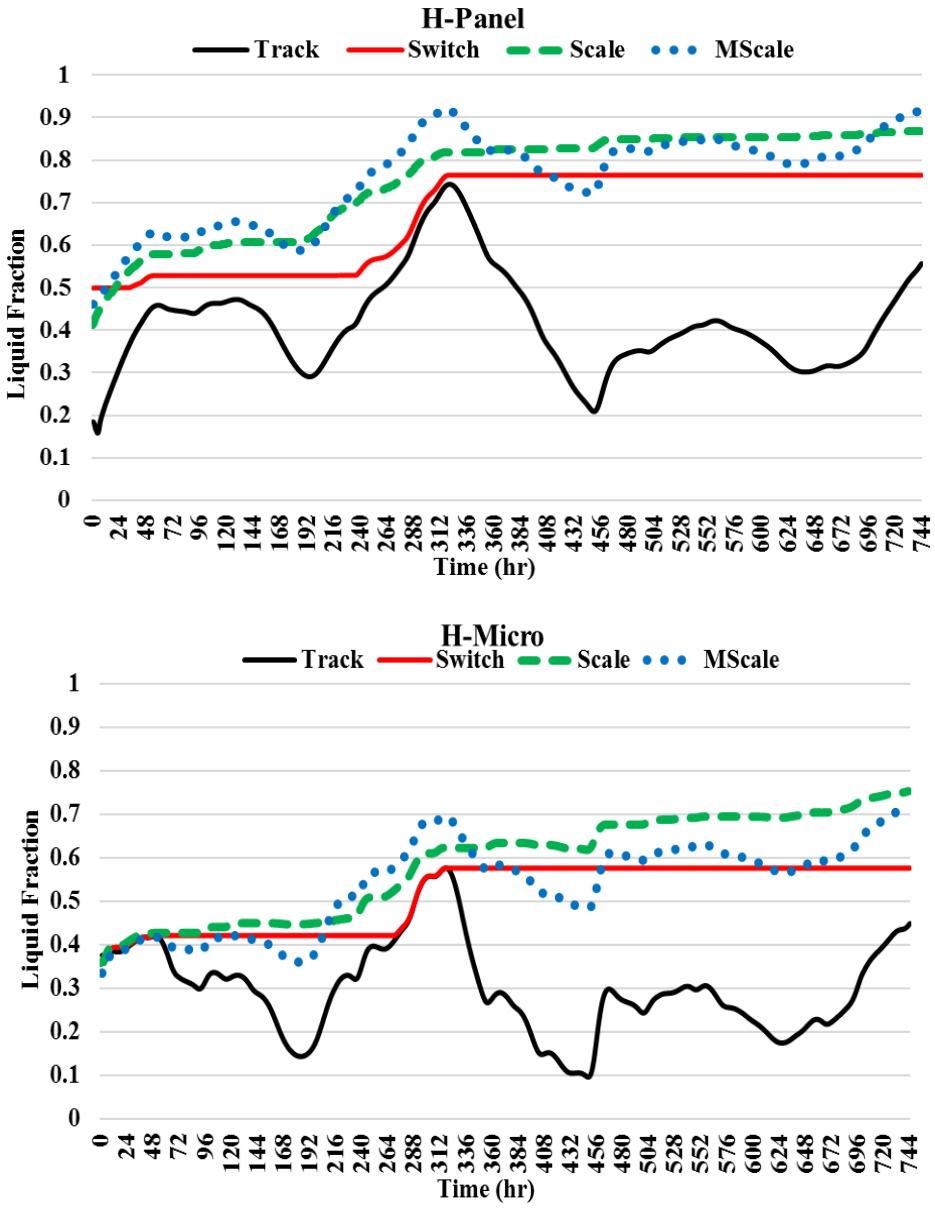

Figure 6.12. The liquid fractions profiles at the interior hempcrete surface for all hysteresis models in both walls; (a) H-Panel wall. (b) H-Micro wall.

Table 6.7. The normalized root mean square difference and fluctuation characteristics of the liquid fraction.

	H-Panel				**H-Micro**			
	Track	Switch	Scale	MScale	Track	Switch	Scale	MScale
Root mean square difference (RMSD)	--	0.30	0.37	0.36	--	0.258	0.332	0.269
Coefficient of variation of the RMSD (CV(RMSD)) %	--	71.9	89.2	86.2	--	85.9	110.2	89.8
Fluctuation ratio % $((\beta_{Max}-\beta_{Min})/\beta_{Avg})$	16.14	1.36	1.98	4.89	23.74	1.64	2.99	7.03
Coefficient of variation (CV) %	4.70	0.37	0.54	1.52	7.08	0.44	0.80	2.67

6.2.2.3. Temperature analysis

Figure 6.13 presents the hourly area-averaged inner temperatures for both wall types and the four hysteresis models. Table 6.8 shows the normalised root mean square difference for the hysteresis models compared to the no-hysteresis/Track model and the temperature fluctuation ratios for both walls. The results show that the temperature difference between the hysteresis models for the H-Panel wall is considerably higher than for the H-Micro case. For example, in the H-Panel wall, the normalised RMSD values between the Switch, Scale, and MScale models compared to the no-hysteresis/Track model are nearly 2%, 1.8%, and 1.15%, respectively. In contrast, for the H-Micro wall, these values decrease to 0.3%, 0.26%, and 0.2%, respectively, as shown in Table 6.8. These findings also suggest that the temperature difference between the hysteresis models is much lower compared to the difference in liquid fractions and energy consumption.

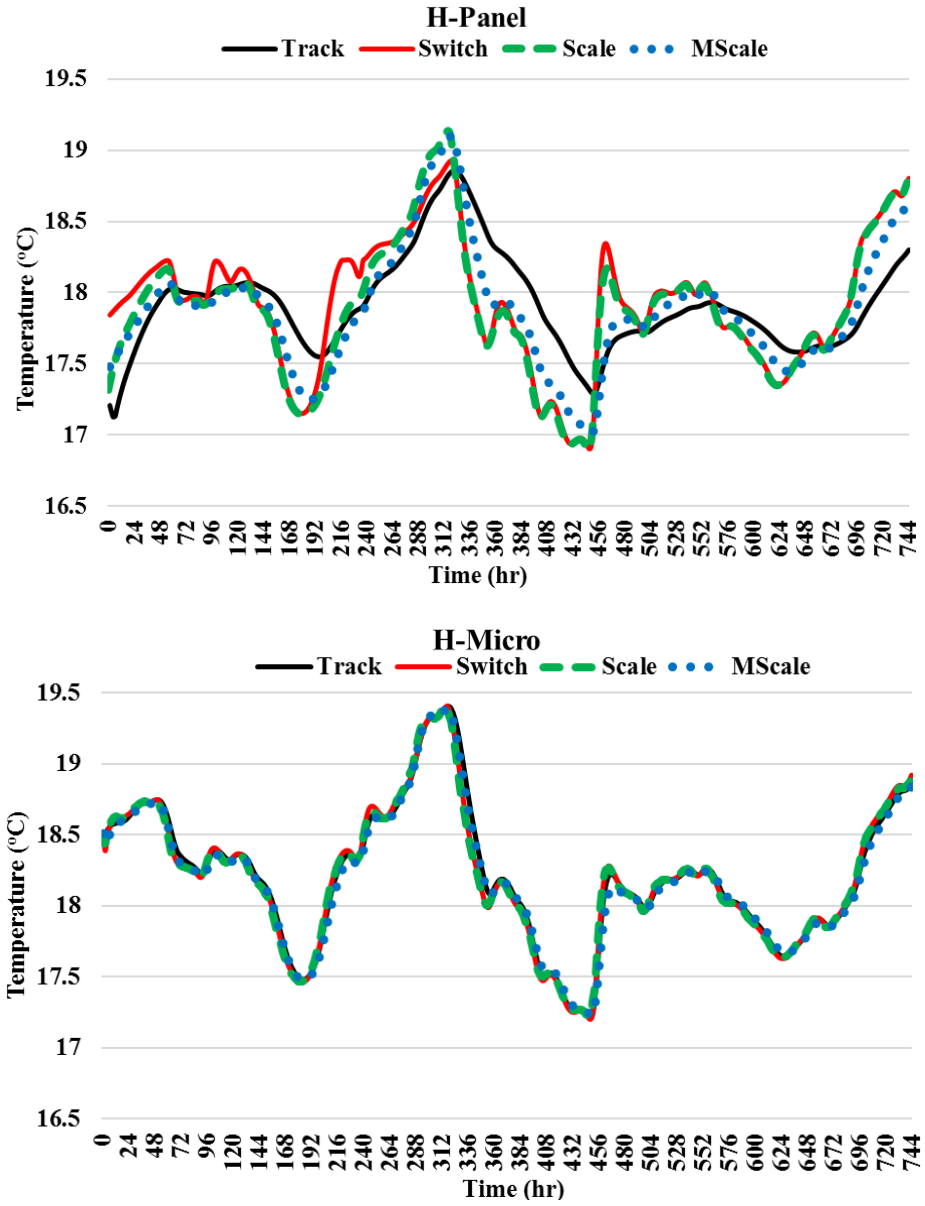

Figure 6.13. The inner temperature profiles in the two walls for the four hysteresis models: (a) H-Panel wall. (b) H-Micro wall.

Figure 6.13 also illustrates that the Switch model shows higher temperature fluctuations than the Track, Scale, and MScale models. Hence, in the H-Panel wall, the fluctuation ratio for the Switch model is 77%, 1%, and 27% higher than the Track, Scale, and MScale models, respectively. These differences become only 5.7%, 2.4%, and 9.1% in the H-Micro wall. Table 6.8 also shows that the temperature values are more spread out in the Switch and Scale models than in both walls' Track

and MScale models. For instance, in the H-Panel wall, the coefficients of variations in the Switch and Scale models are 0.58 and 0.57, respectively, higher than their counterparts of 0.31 and 0.44 in the Track and MScale models. Similar outcomes emerge in the H-Micro wall. Overall, the fluctuation ratios and coefficient of variations for the Switch and Scale models are higher than the Track and MScale models in both walls. The likely explanation for these results is the sensible transition path with constant liquid fraction in the Switch and Scale models, which also explains why the Scale model shows the closest performance to the Switch model.

Table 6.8. The normalized root mean square difference and fluctuation characteristics of the temperature.

	H-Panel				**H-Micro**			
	Track	Switch	Scale	MScale	Track	Switch	Scale	MScale
Coefficient of variation of the RMSD (CV(RMSD)) %	--	1.99	1.82	1.15	--	0.30	0.26	0.21
Fluctuation ratio % $((T_{Max}-T_{Min})/T_{Avg})$	1.05	1.86	1.84	1.46	1.59	1.68	1.64	1.54
Coefficient of variation (CV) %	0.31	0.58	0.57	0.44	0.476	0.505	0.495	0.466

Figure 6.14 shows the fluctuation ratios and coefficients of variation of energy consumptions, liquid fractions, and inner temperatures for the four hysteresis models and the two wall types. The results show that, for all hysteresis models and wall types, the fluctuation ratios and the dispersion of the inner temperature values are significantly smaller than their energy profiles and liquid fraction values. Furthermore, the Track model in both walls exhibits higher fluctuations in the liquid fraction and lower fluctuations in energy profile than the Switch, Scale, and MScale models, especially in the case of the H-Micro wall. In contrast, the Switch model in both walls has lower fluctuations in the liquid fraction and higher fluctuations in energy profiles than the Track, Scale, and MScale methods. The Scale model shows nearly the same performance as the Switch model.

The MScale model behaviour is between the Switch, Scale, and Track models regarding the fluctuations in the three performance variables. In addition, the overall fluctuation features for the liquid fractions and energy consumption in the H-Micro wall are higher than their corresponding values in the H-Panel wall for all hysteresis models. The likely reason for this result is the higher energy density of the PCM in the H-Panel wall that suppresses the liquid fraction fluctuations compared to the lower energy density in the H-Micro wall, making the H-Micro wall more susceptible to weather conditions than the H-Panel wall.

In addition, the inner temperature fluctuations of the Switch and Scale models in the H-Panel wall are higher than their counterparts in the H-Micro wall. The likely reason for this is that their liquid fraction fluctuations are lower in the H-Panel wall than in the H-Micro wall, which means that the Switch and Scale models have sensible heat transitions for longer durations in the H-Panel wall. This results in a higher rate of change and more fluctuations in inner temperatures to meet the inner schedule criteria in the H-Panel wall. In contrast, the inner temperature fluctuations of the Track and MScale models in the H-Panel wall are lower than their counterparts in the H-Micro wall. The likely reason is that the MPCM is more subjected to the outside weather variations in the H-Micro wall, which leads to higher fluctuation features than the H-Panel wall for all performance parameters (i.e., inner temperatures, liquid fractions, and energy profiles). The findings also show that the difference in energy consumption fluctuations between the four hysteresis models is higher for the H-Micro wall than the H-Panel case, and this can be attributed to the more significant difference in the liquid fraction values between the four hysteresis models in the H-Micro wall compared to the H-Panel wall.

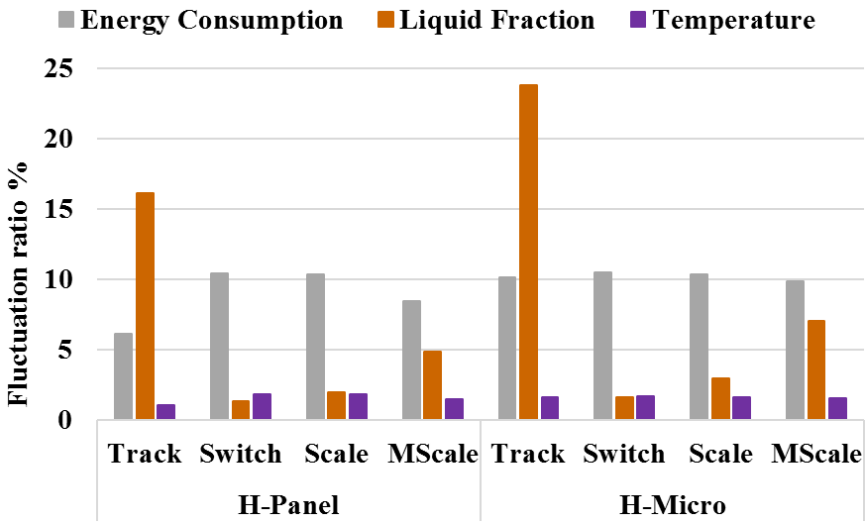

a) Fluctuation ratio.

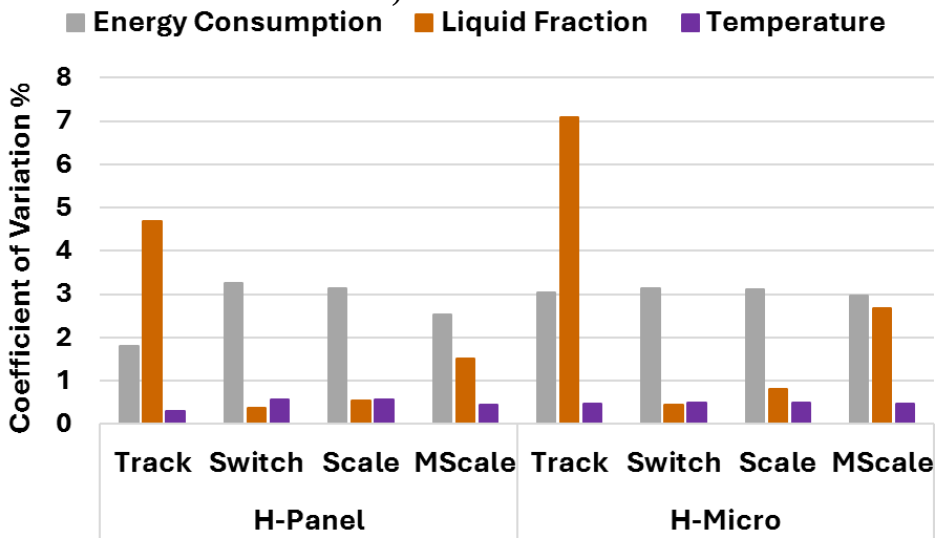

b) Coefficient of variation.

Figure 6.14. The fluctuation characteristics of the three performance values for both walls and the four hysteresis models.

6.2.3. Test Case 3: Effect of increase in microencapsulated PCM

The results of Test Case 2 show that the energy consumption performance of the H-Micro 9% wall is insensitive to the hysteresis models. Therefore, the effect of the PCM percentage on the energy consumption performance in H-Micro walls is analysed for the four hysteresis models using the Test Case 2 setup. Table 6.9 presents January's total heating energy consumption for two higher percentages of microencapsulated PCM walls, 27% and 45%. The findings show that the effect of the hysteresis model is becoming more significant with increasing the percentage of MPCM in the

H-Micro walls. Figure 6.15 illustrates the percentage difference in energy consumption between the hysteresis models and the no-hysteresis/Track case in the three percentages: 9%, 27%, and 45%. It can be observed that the percentage difference increases significantly with the increase in the microencapsulated PCM amount. Thus, the percentage differences in the heating energy consumption es of the H-Micro 9% wall between the Switch, Scale, and MScale models compared to the no-hysteresis/Track model are 0.19%, 0.27%, and 0.49%, respectively. In the case of the H-Micro 27% wall, this difference is higher; for the Switch model, it is 0.32%; for the Scale model, it is 0.44%; and for the MScale method, it is 0.94%. In the case of the H-Micro 45% wall, this difference is significantly higher; for the Switch model, it is 1.31%; for the Scale model, it is 2.10%; and for the MScale method, it is 2.85%. At the same time, the Switch, Scale, and MScale models predicted higher heating energy consumption compared to the no-hysteresis/Track model in all walls. These results suggest that neglecting the hysteresis phenomenon in modelling a high percentage of PCM walls can overestimate the energy savings from integrating PCM into the wall infills.

Table 6.9. Heating energy consumption for the two H-Micro walls in January.

		No-hysteresis/Track	Switch	Scale	MScale
Energy Consumption (Wh/m^2)	27%	6573	6589	6597	6630
	45%	6100	6180	6228	6274

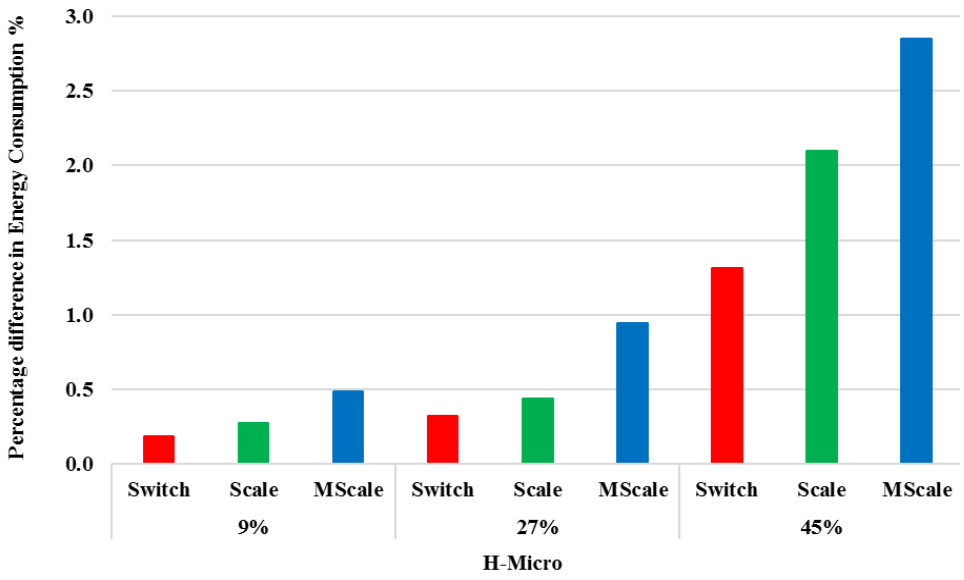

Figure 6.15. Percentage difference in energy consumption between the hysteresis models and the no-hysteresis/Track case in the H-Micro wall and the three percentages.

Figure 6.16 compares January's hourly heating energy consumption of H-Micro 27% and 45% walls for all four hysteresis models. It can be observed that for the H-Micro 45% wall, the hourly heating energy consumption difference between the hysteresis models is more significant than in the H-Micro 27% wall case, further demonstrating the higher sensitivity to the type of hysteresis model in the higher MPCM percentage wall. Table 6.10 summarises the normalised root mean square difference (RMSD) between the Switch, Scale, and MScale models compared to the no-hysteresis/Track model to enable quantifying the differences between the four models throughout the entire month. As presented, the higher MPCM percentage results in higher values of normalized RMSD and a more significant difference between the hysteresis models. For example, the H-Micro 45% wall has the highest normalized RMSD values of 6.53, 5.73, and 4.62 for the Switch, Scale, and MScale models. Additionally, there is a lower difference between the Switch, Scale, and MScale models in the H-Micro 27% wall with normalised RMSD values of 4.45, 3.93, and 3.18, respectively. These results show significantly higher normalised RMSD values of the H-

Micro 27% and 45% walls than the H-Micro 9% wall, with corresponding values of 1.51, 1.35, and 1.13, respectively. These results further emphasise that the H-Micro wall is less sensitive to the hysteresis model at lower MPCM percentages regarding the energy consumption performance.

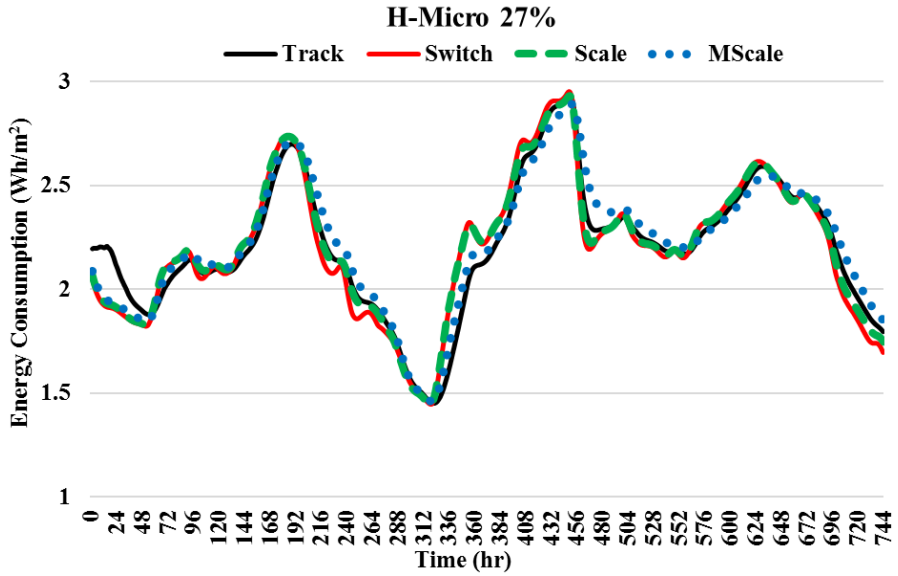

a)

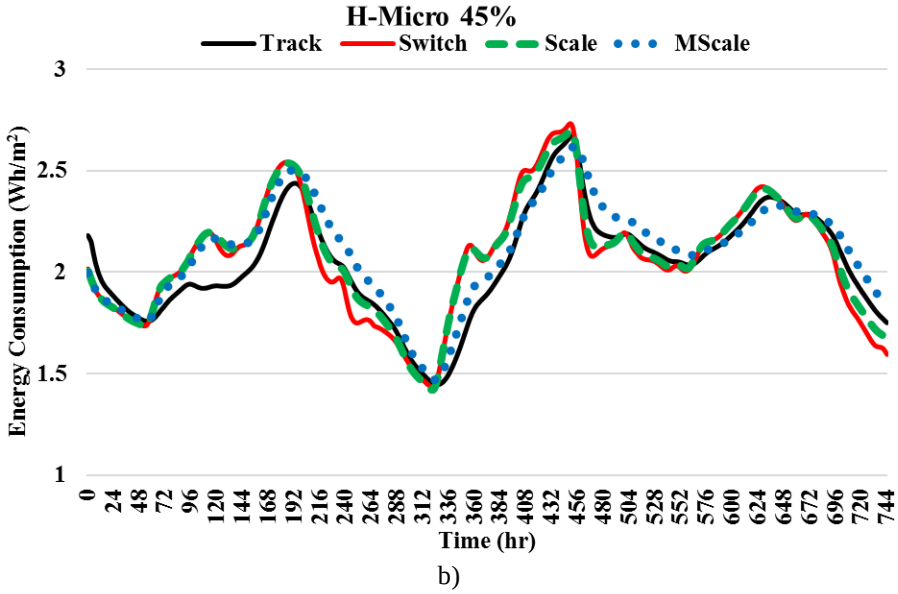

b)

Figure 6.16. The heating energy consumption profiles in January for the H-Micro wall: a) 27% and b) 45% percentages.

Table 6.10. The normalized root mean square difference and fluctuation characteristics of the energy consumption.

	9%				27%				45%			
	Track	Switch	Scale	MScale	Track	Switch	Scale	MScale	Track	Switch	Scale	MScale
Normalised RMSD	--	1.51	1.35	1.13	--	4.45	3.93	3.18	--	6.53	5.73	4.62
Fluctuation ratio %	10.14	10.49	10.36	9.85	8.74	9.74	9.46	8.22	7.53	8.98	8.56	6.85
Coefficient of variation (CV) %	3.03	3.15	3.12	2.97	2.62	2.93	2.88	2.51	2.28	2.68	2.63	2.07

Table 6.10 also shows the fluctuation characteristics of the energy consumption in the three walls (The monthly averaged fluctuation ratio and the monthly averaged coefficients of variation). The higher MPCM percentage in the wall results in lower energy consumption fluctuations due to the increased thermal inertia in the walls. However, Table 6.10 also shows that the difference between the hysteresis models becomes more significant at higher MPCM percentages. In the H-Micro 9% wall, the fluctuation ratio of the Switch model is 3.5%, 1.25%, and 6.5% higher than that of the no-hysteresis/Track, Scale, and MScale models, respectively. The fluctuation ratio of the Switch model for the H-Micro 27% wall is 11.5%, 2.95%, and 18.58% higher compared to the no-hysteresis/Track, Scale, and MScale models, respectively. Furthermore, the fluctuation ratio of the Switch model for the H-Micro 45% wall is 19.2%, 4.98%, and 31.1% higher compared to the no-hysteresis/Track, Scale, and MScale models, respectively.

Table 6.10 shows the same trend in the coefficient of variations of the energy consumption profiles. In the H-Micro 9% wall, the CV values of the Switch model are only 4%, 1%, and 6% higher than that of the no-hysteresis/Track, Scale, and MScale models, respectively. The CV values of the Switch model for the HMP 27% wall are 11.8%, 1.5%, and 16.6% higher compared to the no-hysteresis/Track, Scale, and MScale models, respectively. Furthermore, the fluctuation ratio of the Switch model for the H-Micro 45% wall is 17.4%, 2%, and 29.8% higher compared to the no-

hysteresis/Track, Scale, and MScale models, respectively. These results indicate that although the lower MPCM percentage in the H-Micro walls results in lower thermal inertia and higher fluctuations in the energy consumption profiles, the energy consumption performance is insensitive to the used hysteresis model. In contrast, the higher MPCM percentage in the HMP walls results in higher thermal inertia and lower fluctuations in the energy consumption profiles. Still, the energy consumption performance is susceptible to the hysteresis model.

6.3. Summary

The MScale model best agrees with the experimental results, indicating its capability to better capture the complex phase change phenomena in PCM modelling applications than the three other simulation approaches. In addition, a numerical analysis is performed between two walls with different integration methods for PCM with the same weight percentage, such as a panel PCM added as an internal layer (H-Panel wall) and a microencapsulated PCM distributed in the entire thickness of the infill hempcrete material (H-Micro wall). The two wall configurations were modelled, and results using the four hysteresis models were compared to investigate the performance of three key parameters: thermal energy losses, liquid fractions, and inner surface temperatures. The results indicate that in the H-Panel wall, these three performance parameters are sensitive to the hysteresis model, whereas the H-Micro wall's sensitivity to the hysteresis models regarding energy consumption and inner temperatures is relatively lower. The sensitivity is, however, higher when considering liquid fractions. These findings indicate the importance of the PCM integration technique and the required design parameters for selecting the hysteresis technique in the modelling. Although the MScale model can be utilised in all applications because of its higher accuracy, the default hysteresis models in some numerical modelling software can be used if the PCM integration method and the investigated design parameters have a low sensitivity

to the hysteresis model, such as low percentage of microencapsulated PCM in walls. However, increasing the PCM percentage results in a more significant difference between the four models and increases the sensitivity of energy consumption performance to the hysteresis model.

7. Chapter 7: Temperature Control to Improve Performance of Hempcrete-PCM Wall Assemblies in a Cold Climate

Further research on the impact of the heating setpoints on the thermal performance of hempcrete-PCM wall assemblies is carried out in this chapter. Hempcrete-PCM walls (H-Micro and H-Panel) are simulated under two heating setpoint scenarios designed to investigate and improve the performance of HPCM walls. The Base Case scenario (SCH1) consistently applied setpoint temperature within the thermal comfort range of 20°C. Schedule 2 (SCH2) introduced heating setback temperatures, while Schedule 3 (SCH3) implemented a heating setback temperature ramp-up to reduce the morning peaks occurring due to PCM melting and absorbing the energy, thus causing an increase in heating energy demand. The hysteresis models described in Chapter 6 are used and compared for this investigation. The chapter describes the implemented schedules for the same previous wall configurations, including (1) a wall with 30 cm of hempcrete infill with microencapsulated PCM (H-Micro), (2) a wall with 30 cm of hempcrete and 1 cm of PCM panel (H-Panel). The chapter closes with a summary. This chapter is modified from the journal article https://doi.org/10.3390/en14175343 [22].

7.1. Numerical simulation

The two wall models described in Chapter 6 are used in this study, and the same thermophysical properties of the materials are used in the numerical simulation. The wall types were simulated for Winnipeg, Canada's weather boundary conditions. The base case (SCH1) schedule applied a constant heating setpoint temperature of 20°C at all times. Hence, heating started when the temperature fell below 20°C. This test case investigates the effect of variable heating setpoints between day and night. Thus, the second schedule (SCH2) introduced heating setback temperatures of 18°C during the dormant hours at night (from 22:00 to 07:00) while maintaining

the heating setpoint of 20 ºC during the active hours (from 07:00 to 22:00). The goal of this setback was to increase heating energy savings. The third schedule (SCH3) applied the same heating setback temperatures of 18°C at night but with a ramp-up of 0.5°C every 30 minutes (from 06:00 to 08:00) to avoid the heating energy peaks in the morning.

7.2. Results

7.2.1. The Performance in SCH 1 & 2

Table 7.1 summarizes and compares the energy consumption of the two walls under SCH1 and SCH2 in January. As anticipated, the setback temperatures during the night under SCH2 reduced the wall heating energy consumption compared to SCH1 with a constant setpoint. Thus, heating setpoint reduction of 2 °C during the dormant hours in SCH2 achieved ~3.2% and ~1.7% total heating energy savings for H-Micro and H-Panel walls, respectively. Furthermore, similar to previous findings (Chapter 6), the H-Micro wall assembly achieved lower energy consumption than the H-Panel wall under SCH1 and SCH2.

Further understanding the performance of the two walls requires analysing the hourly energy consumption. In this respect, Figure 7.1 presents the hourly heating energy consumption during active and dormant periods for both walls under SCH1 and SCH2. As presented, both walls exhibited higher energy consumption in SCH2 than SCH1 during active hours due to the higher morning peaks resulting from the sudden increase of the setpoint by 2^{o}C. For example, the energy consumption of the H-Micro and H-Panel walls is ~16% and ~25% higher in SCH2 than SCH1 in the active hours, respectively. On the other hand, SCH2 reduced energy consumption during the night dormant hours compared to SCH1. For instance, SCH2 reduced the energy consumption in the H-Micro and H-Panel walls by ~35% and ~45% compared to SCH1 in the dormant hours, respectively.

Table 7.1. Energy consumption under SCH1 and SCH2.

	H-Micro	H-Panel
SCH1	7008	7683
SCH2	6786	7553

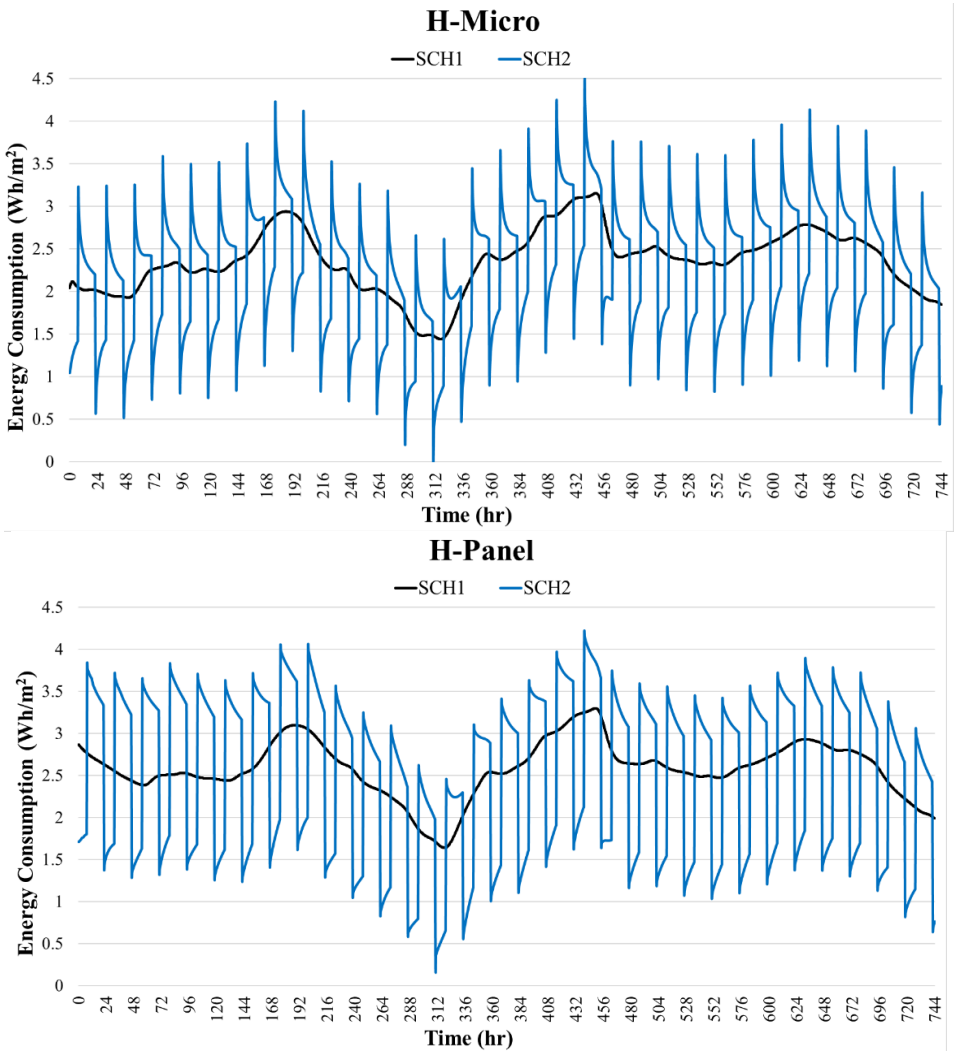

Figure 7.1. The heating energy consumption in January for the four hysteresis models in both walls: (a) H-Panel wall, (b) H-Micro wall.

These results show that the H-Panel wall is affected by the heating setpoint difference in active and dormant hours more than the H-Micro wall. For example, in the H-Micro wall, Figure 7.1 shows that after the morning peaks, the energy profile decreases with a high rate of change. Meanwhile, the energy profile has a slow reduction rate in the H-Panel wall after the morning

peaks. The possible reason for these observations is the high thermal inertia in the concentrated panel PCM compared to the distributed PCM microcapsules in the entire wall thickness. To further understand this behaviour, the monthly averaged values of the range and the coefficient of variation are calculated for the energy profiles in SCH2 for both walls and presented in Table 7.2. The table shows that, on the one hand, the difference between the two peaks (i.e., maximum in the morning, minimum at night) is higher in the H-Micro wall, compared to the H-Panel wall by ~13.2%. On the other hand, the coefficient of variation in the H-Micro wall is lower than the H-Panel wall by ~20.3%. In other words, the higher thermal inertia in the panel PCM results in lower peaks (i.e., lower range) and a slow reduction for the energy profile from the morning peak (i.e., higher coefficient of variation). Thus, the difference between SCH2 and SCH1, in the active and dormant hours, is higher in the H-Panel wall compared to the corresponding difference in the H-Micro wall.

Table 7.2. The range and coefficient of variation for the energy profiles in SCH2 for both walls.

	H-Panel	**H-Micro**
Range (E_{Max}-E_{Min}) (Wh/m^2)	2.42	2.74
Coefficient of variation (CV) %	35.9	28.6

To show an example of comparing the two schedules in both walls, Figure 7.2 illustrates the energy consumption in selected days in January, which had the highest energy consumption (Day 19th). For instance, the figure shows that, in the H-Micro wall, the morning peak in SCH2 on Day 19th is higher than that of SCH1 by ~44.1%. Meanwhile, in the H-Panel wall, the morning peak in SCH2 is higher than that of SCH1 by ~29.8%. However, at the end of the active hours, the energy consumption in SCH2 is higher than the corresponding value in SCH1, only by 5.4%, in the H-Micro wall. Meanwhile, the corresponding difference in the H-Panel wall is 13.8%. As explained before, the H-Panel wall has lower morning peaks, but the slow reduction in the energy profile

after the morning peak results in higher energy consumption overall in the active hours compared to the H-Micro wall. For the same reasons, there are higher energy savings in the dormant hours for the H-Panel wall than for the H-Micro wall.

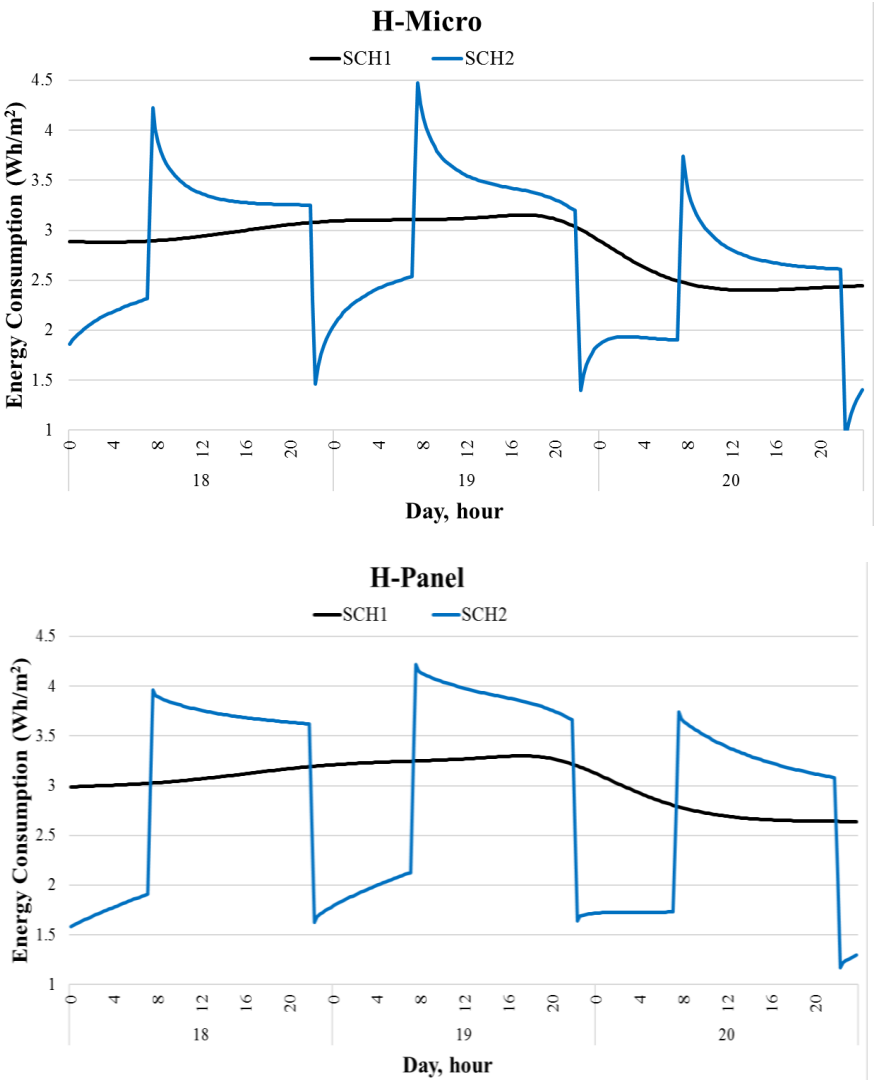

Figure 7.2. The heating energy consumption in January for selected days: a) H-Panel wall, and b) H-Micro wall.

7.2.2. The effect of ramping in SCH3

Although SCH2 achieved energy savings compared to the base case SCH1, energy increases in the daytime and morning peaks may cause higher energy prices due to the high energy demand

during the on-peak hours and larger equipment size to meet that demand. Therefore, our further investigation included applying temperature ramping to reduce the energy peaks during the morning and active hours (SCH3). Figure 7.3 shows the daily peak energy consumption value to compare the ramping effect in both walls. The figure shows that ramping up the setpoints in SCH3 reduces the peak morning values compared to SCH2, but with different rates for each wall type. As shown, the H-Micro wall is highly affected by SCH3 compared to the H-Panel wall. For example, the monthly average difference between the peaks in SCH3 and SCH2 is 11% (±0.9%) in the H-Micro wall, compared to only 1.8% (±0.6%) in the H-Panel wall.

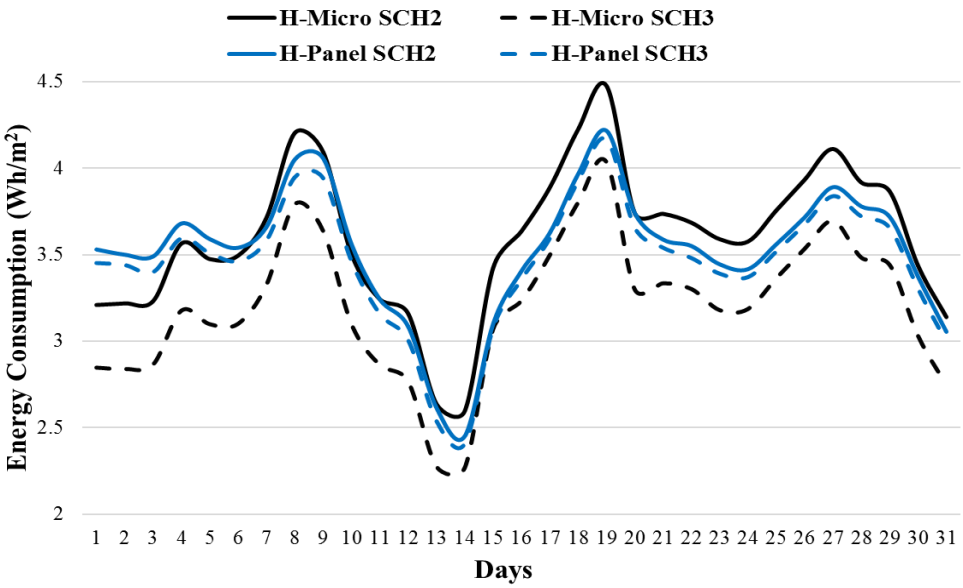

Figure 7.3. The daily peak for SCH2 and SCH3 of the two walls.

Figure 7.4 shows the energy consumption on selected January days, with the highest energy consumption (Day 19th). As shown in the H-Micro wall, the morning peak in SCH3 is lower than that of SCH2 by nearly 11%, with a peak shift of approximately one hour. Meanwhile, in the H-Panel wall, the morning peak in SCH3 is lower than that of SCH2 by only 2.2%, with nearly the same peak shift. In the H-Micro wall, the total heating energy in the three days is lower in SCH3 than in SCH2 by only ~0.6%. At the same time, the heating energy in the three days is higher in

SCH3 than SCH2 by only ~0.9% in the H-Panel wall. Ramping the schedule causes a slight increase in the energy consumption during the dormant hours and the active hours after the peak, and it reduces the energy consumption due to the peak reduction itself. The results show that in the H-Micro wall, the peak reduction outweighs the increase by a small amount (i.e., the 0.6% difference). However, in the H-Panel wall, the increase in energy outweighs the peak reduction (i.e., the 0.9% difference) due to the negligible peak reduction (i.e., only 2.2%).

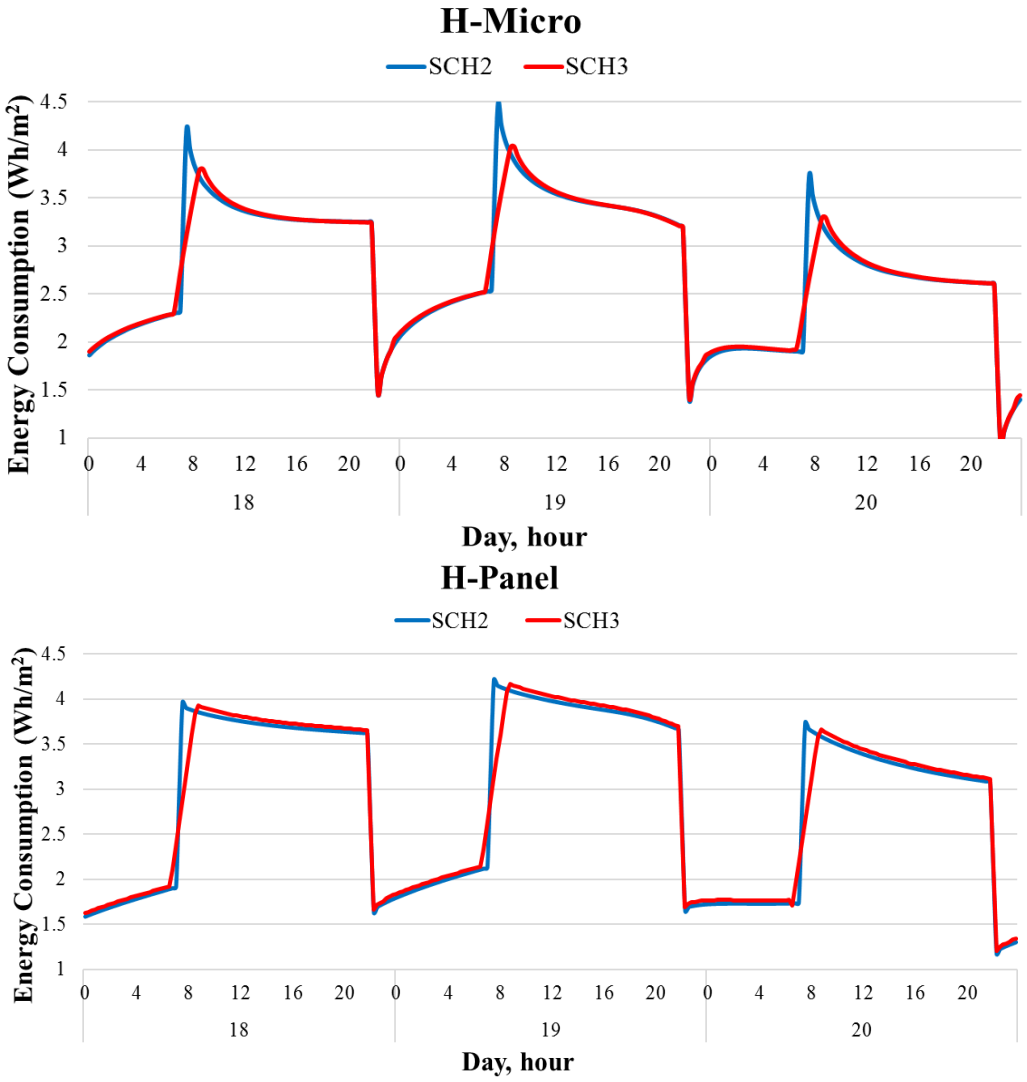

Figure 7.4. The heating energy consumption in January for selected days: a) H-Panel wall, and b) H-Micro wall.

7.2.3. The predictions of different hysteresis models

When the indoor temperature is constantly set to 20^0C, the results show that the energy consumption of the H-Micro wall is nearly insensitive to the hysteresis models (Chapter 6). However, this outcome might differ in the case of different setpoints between day and night. Table 7.3 presents the heating energy consumption in the two walls at SCH1 and SCH2. Additionally, Figure 7.5 shows the percentage difference in heating energy consumption between the hysteresis models and the no-hysteresis/Track case in the two walls and schedules.

It can be observed that the percentage difference with the no-hysteresis/Track model increases significantly with changing the day and night setpoints in SCH2 compared to SCH1 for both walls. This difference is higher in the case of the H-Panel wall; for the Switch model, it is 1.06%; for the Scale model, it is 2.15%; and for the MScale method, it is 3.57%. Thus, changing the heating schedules by lowering the night setpoint results in a more significant difference between the hysteresis models in the H-Panel wall compared to the H-Micro wall. In all cases, the Switch, Scale, and MScale models predicted higher heating energy consumption compared to the no-hysteresis/Track model, which indicates that neglecting the hysteresis phenomenon when modelling different heating schedules overestimates the energy savings achieved by integrating PCM into the wall infills. The same observation applies to the H-Micro wall. Thus, the difference with the no-hysteresis/Track model increases in SCH2 compared to SCH1; for the Switch model, it is 0.33%; for the Scale model, it is 0.57%; and for the MScale method, it is 0.95%.

Table 7.3. Heating energy consumption of the two walls in January for two schedules and all hysteresis models, and the difference with the No-hysteresis model.

		H-Panel				H-Micro			
		No-hysteresis /Track	Switch	Scale	MScale	No-hysteresis /Track	Switch	Scale	MScale
Energy Consumption (Wh/m^2)	SCH1	7589	7610	7637	7683	6974	6987	6993	7008
	Difference	-	0.27%	0.62%	1.28%	-	0.18%	0.27%	0.49%
	SCH2	7293	7370	7450	7553	6722	6744	6760	6786
	Difference	-	1.06%	2.15%	3.57%	-	0.33%	0.57%	0.95%

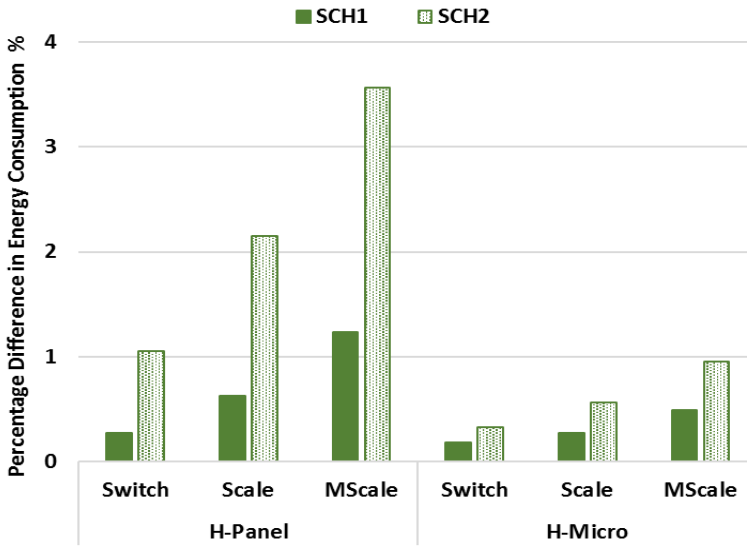

Figure 7.5. Percentage difference in energy consumption between the hysteresis models and the no-hysteresis/Track case for the two schedules.

To further understand the difference between the hysteresis models, Table 7.4 presents the average percentage increase in daily peaks in SCH2 compared to SCH1, the energy consumption difference in the active and dormant hours, and the coefficient of variation of the energy consumption profiles. The table shows that, in the H-Panel wall, the Track model has the lowest energy peak rise during the active hours (33%) in SCH2, followed by the MScale, while the Scale and Switch models are the highest with 53% and 54%, respectively. However, the total energy consumption in active hours in the Switch and Scale models is the lowest at 17% and 19%. These results can be explained by the sensible transition of the Switch and Scale models, which, on the one hand, results

in their low ability to suppress the morning peaks and, on the other hand, causes a quick reduction for the energy profile after the peak, which appears in the low coefficient of variation of the Switch and Scale models (~28%), compared to the Track and MScale models.

Meanwhile, the Track and MScale models predict higher energy consumption during the active hours by 23% and 25, respectively. Even though they are better at suppressing the morning peaks, their latent transition behaviour also causes a slow reduction for the energy profile after the peak (appears in the high coefficient of variation of the Track and MScale models). The same trend and observations appear in the H-Micro wall but with a more negligible difference between the models. However, the H-Micro wall shows a higher morning peak rise and lower energy consumption increase during the active hours, compared to the H-Panel wall, due to the effect of distributing the PCM on a broader thickness (as explained in Section 7.2.1).

Table 7.4. The energy peaks and consumption in active hours, and coefficient of variation for the energy profiles in SCH2 for both walls, and four hysteresis models.

	H-Panel				**H-Micro**			
	Track	Switch	Scale	MScale	Track	Switch	Scale	MScale
Percentage of peak increase in active hours %	33	54	53	39	55	58	58	57
Percentage of energy consumption rise in active hours %	23	17	19	25	16.1	14.6	14.8	16.3
Coefficient of variation (CV) %	37.25	28.09	28.81	36.02	28.88	27.23	27.09	28.58

Figure 7.6 shows the daily peak value of energy consumption in SCH2 and SCH3 to compare the ramping effect in both walls and the hysteresis models. The figure shows that ramping up the setpoints in SCH3 reduces the peak morning values compared to SCH2 but with different rates for each hysteresis model and wall. As shown, the Track model in the H-Micro wall is highly affected by SCH3 compared to the H-Panel wall. For example, the monthly average reduction of the

morning peak due to ramping in SCH3 is 10.9% (±0.5%) in the H-Micro wall, compared to 1.4% (±1%) in the H-Panel wall, which shows the same trend observed in the MScale model between the two walls (Section 7.2.2). On the other hand, the Switch and Scale models in both walls are highly affected by the ramping in SCH3 due to their sensible transition behaviour, but it has a slightly higher effect on the H-Micro wall than the H-Panel wall. For instance, in the Switch and Scale models, respectively, the average peak reduction in SCH3 is 12% (±1%), and 11.9% (±1%) in the H-Micro wall, compared to 9.3% (±1.8%), and 9.2% (±1.3%) in the H-Panel wall.

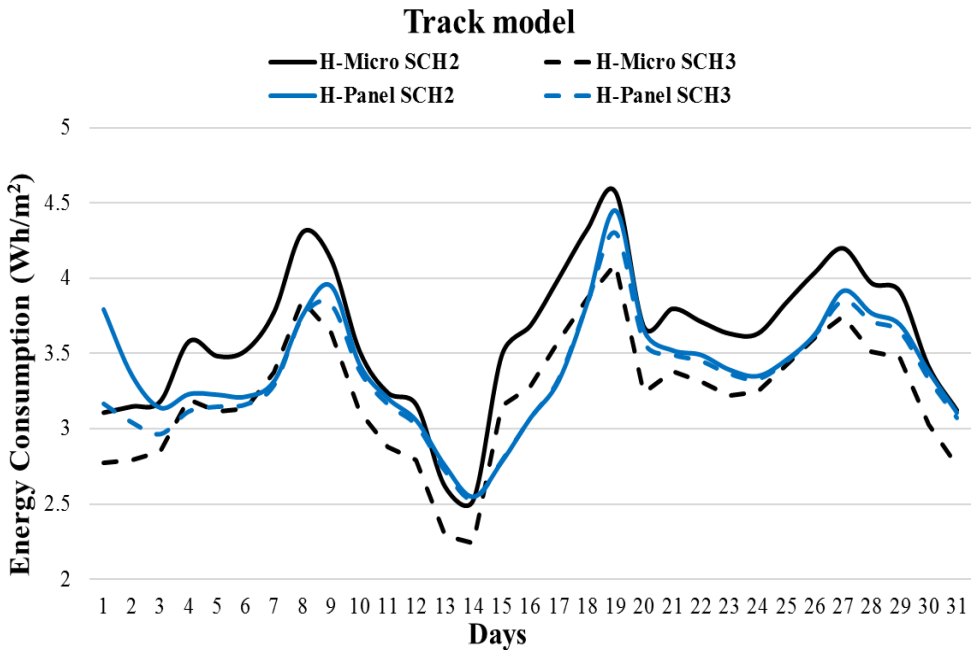

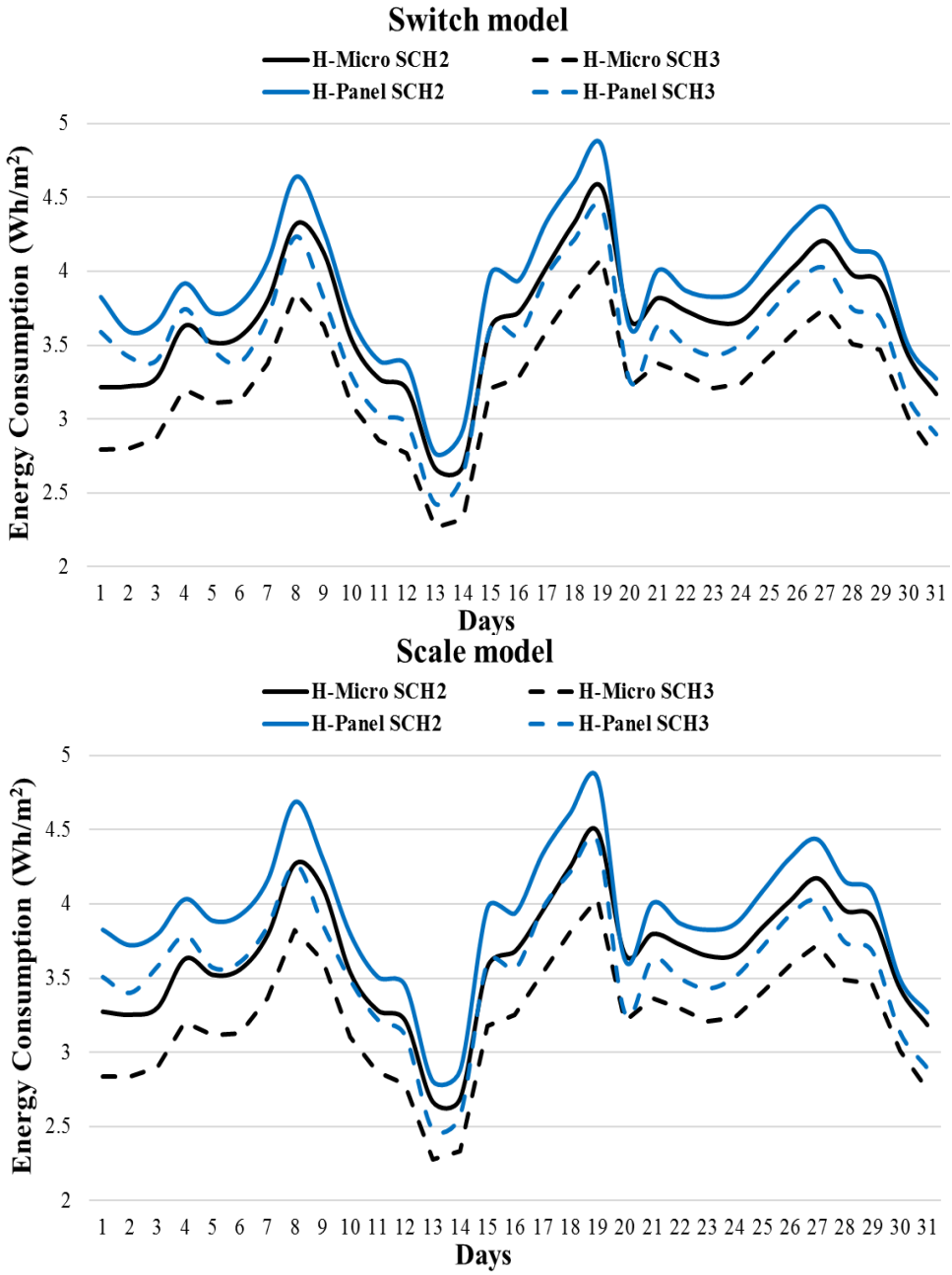

Figure 7.6. The daily peak for SCH2 and SCH3 in the two walls for the Track, Switch, and Scale models

7.3. Summary

This research investigated the effects of the scheduled heating setpoints on the performance of two different hempcrete-PCM walls while comparing the predictions of the different hysteresis models. It was observed that changing the setpoint during the active and dormant hours can significantly

influence the PCM behaviour and the thermal performance of the wall. The findings show that SCH2 and SCH3 with variable heating setpoints imply a more significant difference between the hysteresis models in both walls than SCH1 with the constant heating setpoint, especially in the H-Panel wall. Nevertheless, additional investigation and analysis are needed to understand better the impact of heating schedules on the thermal performance of PCM-enhanced wall systems. This research is fundamental because PCM's phase change must be synchronised with the operation of HVAC systems to maximise energy savings while minimising instances when PCM increases energy demand.

8. Conclusions, limitations, and future recommendations

8.1. General conclusions

- The first step included characterizing hemp-lime composites with different design mixes and obtaining their mechanical, thermal, and moisture buffering properties. Innovative, widely available binders and formulas and a better understanding of the material's performance are indispensable steps to increase hempcrete's utilization in the construction industry. This study is the first research that applies recycled crushed brick as a pozzolan in hempcrete mixes to increase their availability while reducing their environmental impact. Another contribution to the body of knowledge is the comprehensive mechanical, thermal, and moisture characterization of hemp-lime composites with different binder mix designs. The main conclusions of this study are as follows:
  - The thermal and mechanical properties of hempcrete depend on its density. While reducing the density reduces the desirable thermal conductivity, this resulted in a reduction of compressive strength at a higher rate. Therefore, optimization is needed to find a suitable value for density.
  - The higher content of hemp hurd combined with an application-orientated level and direction of compaction can further enhance the thermal properties and develop products suitable for insulation infill wall utilizations.
  - Although all the developed design mixes have mechanical, thermal, and moisture buffering properties suitable for infill wall applications, in small amounts, recycled crushed brick is an excellent alternative to conventional pozzolans for creating more environmentally friendly hempcrete composites. For example, the hempcrete samples with 10% crushed brick have the lowest thermal conductivity considering their density and the highest

moisture buffer capacity. Furthermore, the new hydrated lime and crushed brick formulas have comparable mechanical properties to metakaolin and hydraulic lime formulas.

  - The water content is an essential design parameter due to its significant impact on the mechanical and thermal properties of the hempcrete samples. This study indicates that a smaller amount of water leads to some specimens' inferior mechanical properties due to incomplete hydration caused by the high suction ability of the hemp hurd.

- The second step included investigating the effect of integrating MPCMs with different phase change temperatures and percentages into a hempcrete mixture to improve its thermal properties. Moreover, the work presented herein provides new and valuable design recommendations regarding the material amount and characteristics of new hempcrete-phase change material composites. Therefore, the results and findings from this study provide helpful guidance for applying advanced materials, especially in buildings exposed to cold climates. The main conclusions of this study are as follows:
  - The microstructural analysis indicates that new Nextek products exhibit better shell integrity and less agglomeration than the previous generation Micronal. The observations also showed well-dispersed MPCM particles within the hempcrete specimen with no signs of capsule damage or observable agglomeration.
  - Incorporating MPCMs into a hempcrete mixture produces a new latent material with different thermal properties and behavior. Thus, the developed HPCM formulas have superior heat storage potential over hempcrete due to their higher specific heat capacity. Nextek products MPCM18 and MPCM24 have approximately 45% higher encapsulation efficiency than Micronal products MPCM23 and MPCM25.

- The thermal conductivity of the HPCM samples has a strong linear relationship with the density, the same as the hempcrete samples. The findings also show increased HPCM samples' density, resulting in lower thermal conductivity than the base hempcrete sample. Hence, precise control of the tamping process and ingredient amounts is essential to avoid increasing the HPCM thermal conductivity.
- The numerical analysis shows promising savings in heating and cooling, ranging from approximately 5% to 16% and 1% to 36%, respectively. These results are consistent with the previous Canadian studies that reported heating energy savings ranging from 2.5% to 17% and maximum cooling energy savings of approximately 50% [19, 181].
- The numerical analysis also indicates that an increase in the percentage share of MPCMs from 9% to 18% in the hempcrete mixture reduces cooling savings by approximately 13% and 7% for 18HPCM18 and 18HPCM23, respectively. It also reduces heating energy savings by about 4% and 2% for 18HPCM23 and 18HPCM18, respectively. These results support the findings of previous studies, which reported that an increase in the amount of phase change materials stops being effective after a certain point [19].
- In summary, there is a need to thoroughly consider the operating temperature and percentage share of MPCMs within hempcrete concerning the specific application and performance objectives. The optimal integration of HPCMs into the building envelope might also require changes in the operation of the heating and cooling systems.

- The third step proposed a new hysteresis model, called the Modified Scale model (MScale), to accurately capture the complex hysteresis phenomena occurring in partial phase change processes while overcoming the limitations of the three already established hysteresis models (Track, Switch, and Scale). Unlike these models, the new MScale model allows for changing

the liquid fraction during a partial phase change process but with a changing rate that is different from the Track model and considers hysteresis by allowing the phase change curve transition without assuming that the liquid fraction is constant, as in the Switch and Scale models. Another novelty of this study is the first use of the new model in a finite-volume commercial code (ANSYS Fluent). Moreover, to the best of the authors' knowledge, this is the first study to investigate the hysteresis effect on two different PCM integration methods in walls: microencapsulation and macroencapsulation.

- The four hysteresis models were compared and validated against the experimental results. The MScale model best agrees with the experimental results, indicating its capability to better capture the complex phase change phenomena in PCM modelling applications than the three other simulation approaches.
- In addition, a numerical analysis is performed between two walls with different integration methods for PCM with the same weight percentage, such as a panel PCM added as an internal layer (H-Panel wall) and a microencapsulated PCM distributed in the entire thickness of the infill hempcrete material (H-Micro wall). The two wall configurations were modelled, and results using the four hysteresis models were compared to investigate the performance of three key parameters: thermal energy losses, liquid fractions, and inner surface temperatures. The results indicate that in the H-Panel wall, these three performance parameters are sensitive to the hysteresis model, whereas the H-Micro wall's sensitivity to the hysteresis models regarding energy consumption and inner temperatures is relatively lower. The sensitivity is, however, higher when considering liquid fractions.
- These findings indicate the importance of the PCM integration technique and the required design parameters for selecting the hysteresis technique in the modelling. Although the

MScale model can be utilised in all applications because of its higher accuracy, the default hysteresis models in some numerical modelling software can be used if the PCM integration method and the investigated design parameters have a low sensitivity to the hysteresis model (as for the energy consumptions in the H-Micro wall). These apply to a relatively low percentage of microencapsulated PCM (~9%); different outcomes emerge with higher distribution in the entire thickness of the wall.

  - Thus, the additional numerical test case is performed to study the effect of PCM percentage in the H-Micro wall on the sensitivity of the energy consumption performance to the hysteresis models. The findings show that increasing the PCM percentage results in a more significant difference between the four models and increases the sensitivity of energy consumption performance to the hysteresis model.

- The fourth step investigated the effects of the scheduled heating setpoints on the performance of the two hempcrete-PCM walls and compared the predictions of the hysteresis models. It was observed that changing the setpoint during the active and dormant hours can significantly influence the PCM behaviour and the thermal performance of the wall. The findings show that:
  - The setback temperatures at night under SCH2 reduced the total heating energy compared to SCH1 with a constant setpoint. Moreover, SCH2 with variable heating setpoints implies a more significant difference between the hysteresis models in both walls than SCH1 with the constant heating setpoint.
  - Both walls showed higher energy consumption in SCH2 than SCH1 during the active hours due to the higher morning peaks resulting from the sudden increase of the setpoint by 2 ^{o}C. The results also showed that the H-Panel wall is more affected by the heating setpoint difference in active and dormant hours than the H-Micro wall.

- The effect of applying temperature ramping to reduce the energy peaks during the morning was also investigated. The findings showed that ramping up the setpoints in SCH3 reduced the peak morning values compared to SCH2 but with different values in each wall type, as the H-Micro wall was more affected by SCH3 than the H-Panel wall.
- The different predictions of the hysteresis models were investigated and compared. Lowering the night setpoint in SCH2 resulted in a more significant difference between the hysteresis models than SCH1, with a higher difference in the H-Panel wall than the H-Micro wall. These findings indicate that neglecting the hysteresis phenomenon in modelling can give false predictions about the energy savings achieved by integrating PCM into the wall infills.

8.2. Limitations and future work

- Future work should focus on optimizing and standardizing methods for hempcrete design mixes and testing procedures (i.e., no standards for hempcrete have been developed so far), in which increasing the number of tested design mixes in each hempcrete composite is necessary. For instance, only two design mixes were studied for CB and NHL composites, and three design mixes were studied for MK composites, so a design mix could be selected to continue with the HPCM research. Hence, further research is needed with more design mixes in each composite.
- A follow-up study should investigate mechanical properties in the perpendicular and thermal behavior in the parallel direction of hempcrete formulas with a 1:1 binder to hemp hurd ratio and wider density ranges. Further research should also optimize compaction levels and orientations for infill wall installations of hemp-lime composites using blocks or wall panels.

- Future research should optimize the use of the investigated lime mortars and pozzolans in hemp-lime mixes, especially the crushed brick ingredient, as it requires a more detailed investigation before generalizing its use in hemp-lime composites. A follow-up study should also explore other locally available materials to improve hemp-lime composites' performance and affordability while reducing their environmental impact. Chemical analysis should also be performed to understand the pozzolanic reactivity and hydration process in hempcrete samples, especially for crushed brick, to understand further and optimize pozzolan inclusion in the design mix.
- A follow-up study should optimize water content for different infill wall applications. Further research should also investigate a hemp pretreatment process and water retainers' application to balance the high suction of the hurd and improve the mechanical behavior and durability of hemp-lime composites. Further research is needed to investigate hemp-lime composites' durability and decay under different environmental conditions, freezing and thawing properties, and acoustic performance.
- The number of samples in the mechanical strength experiments was only four for each design mix in the compressive tests and only two samples per design mix in the tensile tests. Further research is needed with more samples for each design mix to improve the accuracy of the results and its repeatability. Different shapes of samples should also be tested to investigate the sensitivity of the mechanical properties to the mold shape.
- The moisture buffering tests were performed only on three selected design mixes (one from each composite). More research with more design mixes is needed to understand hempcrete moisture regulation better. In addition, MBV is calculated only for hempcrete in this research. Hence, extra experimental work is needed at a wall system level to obtain the effective MBV

of the hempcrete walls. A follow-up study should also investigate the vapor and moisture diffusion phenomena in the hempcrete/HPCM walls with more realistic configurations to include insulations, air barriers, and vapor barrier layers to the wall.

- There is a need to investigate different design approaches for HPCM walls. For example, adding an insulation layer at the exterior surface of the wall could reduce the impact of outdoor temperature fluctuations. Furthermore, using multiple types of MPCM with different operating ranges within the wall infill could cover the whole year. Another approach could include dividing the hempcrete wall into separate layers with different MPCM types and amounts.
- Moreover, cost analysis should be performed to facilitate the decision-making process regarding implementing the new hempcrete-phase change material composites. Subsequent work should also include further experimental testing of Nextek and Micronal products to expand our understanding of their differences, especially knowing that the small sample sizes in the SEM analysis do not provide enough information about the PCM distribution in the entire hempcrete sample. Thermal imaging can provide valuable information in this respect. A follow-up study is also needed to investigate the effect of possible PCM agglomeration on the thermal performance of hempcrete/PCM walls.
- This research is also limited to the thermal properties of hempcrete-PCM walls. Further research is needed to characterize the mechanical properties of HPCM composites and study the effect of adding PCM into hemp-lime composites. In addition, there is a need to investigate reducing the thermal conductivity of the HPCM samples using the proper layering orientation for the application (i.e., parallel orientation). Additional research is needed to investigate the moisture buffering performance, fire resistance, acoustic properties, freezing and thawing tests, and durability of the HPCM composite under repetitive thermal cycles.

- This research is also limited to numerical analysis of hempcrete-PCM walls. Future research should include a more extensive numerical analysis of whole buildings and on-site experimental testing of hempcrete-PCM walls to optimise their integration and further understand their influence on heating systems. Moreover, more realistic boundary conditions such as actual weather data, internal radiation exchange, and variable solar absorptivity should be included.
- Biobased products should be included instead of the Paraffin core products to improve further the MPCMs integrated into buildings (Nextek and Micronal). In this regard, the same manufacturer (Microtek) produced a biobased and less flammable product (Vivtek) with the same patented Nextek encapsulation technology. Such products can further decrease embodied energy and improve the sustainability of MPCMs.
- This research was conducted for a hysteresis range of approximately 7 $^{\circ}$C. In the case of different hysteresis ranges, the Track model is expected to be insensitive in partial phase change processes because it does not allow any transition between the melting and freezing curves. The Switch and Scale models are expected to be highly sensitive to such variations because they allow a sensible transition process between the curves, which means the duration of this sensible storage transition process would directly depend on the range of hysteresis. The MScale model is also expected to be sensitive to the hysteresis range but with a lower degree than the Switch and Scale models. A follow-up study should investigate and quantify each model's sensitivity difference in-depth.
- Moreover, the numerical modelling in this paper is limited to conduction-dominant cases, which is the case with buildings' walls. A follow-up study should experimentally and numerically investigate the possibility of following dynamic hysteresis curves to capture

further complex details in the phase change process in the non-conduction dominant applications that involve convection and need to add the momentum governing equation.

- In the fourth step of this research, only two schedules for heating setpoints were analysed. Further research is needed to provide a sensitivity analysis between inner schedules and PCM temperatures. Different ramping profiles should also be investigated to reduce the morning peaks further.
- More work is needed to understand the relationship between the PCM store/release cycles at different time scales, weather conditions, and their interaction with the active HVAC systems. This research was also limited to the typical weather profile, south wall orientation, and heating consumption for winter conditions. Follow-up research should investigate the effect of the actual weather data, different orientations, and PCM performance in cooling applications for summer.

References

1. Pérez-Lombard, L., J. Ortiz, and C. Pout, *A review on buildings energy consumption information.* Energy and Buildings, 2008. **40**(3): p. 394-398.
2. González-Torres, M., et al., *A review on buildings energy information: Trends, end-uses, fuels and drivers.* Energy Reports, 2022. **8**: p. 626-637.
3. Jaysawal, R.K., et al., *Concept of net zero energy buildings (NZEB) - A literature review.* Cleaner Engineering and Technology, 2022. **11**.
4. Karlessi, T., et al., *The Concept of Smart and NZEB Buildings and the Integrated Design Approach.* Procedia Engineering, 2017. **180**: p. 1316-1325.
5. IEA, *Net Zero by 2050: A Roadmap for the Global Energy Sector.* INTERNATIONAL ENERGY AGENCY, 2021.
6. Zhou , G., M. Krarti, and G.P. Henze, *Parametric Analysis of Active and Passive Building Thermal Storage Utilization*.* Journal of Solar Energy Engineering, 2005. **127**(1): p. 37-46.
7. Liu, J., et al., *The thermal mechanism of warm in winter and cool in summer in China traditional vernacular dwellings.* Building and Environment, 2011. **46**(8): p. 1709-1715.
8. Ahmed Ali, K., M.I. Ahmad, and Y. Yusup, *Issues, Impacts, and Mitigations of Carbon Dioxide Emissions in the Building Sector.* Sustainability, 2020. **12**(18).
9. Sarbu, I. and C. Sebarchievici, *A Comprehensive Review of Thermal Energy Storage.* Sustainability, 2018. **10**(1).
10. Sharma, A., et al., *Review on thermal energy storage with phase change materials and applications.* Renewable and Sustainable Energy Reviews, 2009. **13**(2): p. 318-345.

11. Pielichowska, K. and K. Pielichowski, *Phase change materials for thermal energy storage.* Progress in Materials Science, 2014. **65**: p. 67-123.

12. da Cunha, S.R.L. and J.L.B. de Aguiar, *Phase change materials and energy efficiency of buildings: A review of knowledge.* Journal of Energy Storage, 2020. **27**.

13. Hasnain, S.M., *Review on sustainable thermal energy storage technologies, Part I: heat storage materials and techniques.* Energy Conversion and Management, 1998. **39**(11): p. 1127-1138.

14. Imafidon, O.J. and D.S.K. Ting, *Retrofitting buildings with Phase Change Materials (PCM) – The effects of PCM location and climatic condition.* Building and Environment, 2023. **236**.

15. Gholamibozanjani, G. and M. Farid, *A Critical Review on the Control Strategies Applied to PCM-Enhanced Buildings.* Energies, 2021. **14**(7).

16. Klimeš, L., et al., *Computer modelling and experimental investigation of phase change hysteresis of PCMs: The state-of-the-art review.* Applied Energy, 2020. **263**.

17. Barz, T., et al., *Phenomenological modelling of phase transitions with hysteresis in solid/liquid PCM.* Journal of Building Performance Simulation, 2019. **12**(6): p. 770-788.

18. Mohammadzadeh, A. and M. Kavgic, *Multivariable optimization of PCM-enhanced radiant floor of a highly glazed study room in cold climates.* Building Simulation, 2019. **13**(3): p. 559-574.

19. Al-Janabi, A. and M. Kavgic, *Application and sensitivity analysis of the phase change material hysteresis method in EnergyPlus: A case study.* Applied Thermal Engineering, 2019. **162**.

20. Al-janabi, A., et al., *Comparison of EnergyPlus and IES to model a complex university building using three scenarios: Free-floating, ideal air load system, and detailed.* Journal of Building Engineering, 2019. **22**: p. 262-280.

21. Imghoure, O., et al., *Evaluation of phase change material and thermochromic layers in a "smart wall" in different climates for improving thermal comfort in a building.* Journal of Building Engineering, 2022. **56**: p. 104755.

22. Kavgic, M. and Y. Abdellatef, *Temperature Control to Improve Performance of Hempcrete-Phase Change Material Wall Assemblies in a Cold Climate.* Energies, 2021. **14**(17).

23. Feng, F., et al., *Enhancement of phase change material hysteresis model: A case study of modeling building envelope in EnergyPlus.* Energy and Buildings, 2022. **276**.

24. Hoes, P., et al., *Investigating the potential of a novel low-energy house concept with hybrid adaptable thermal storage.* Energy Conversion and Management, 2011. **52**(6): p. 2442-2447.

25. Jami, T., S.R. Karade, and L.P. Singh, *A review of the properties of hemp concrete for green building applications.* Journal of Cleaner Production, 2019. **239**.

26. Barbhuiya, S. and B. Bhusan Das, *A comprehensive review on the use of hemp in concrete.* Construction and Building Materials, 2022. **341**.

27. Dahal, R.K., B. Acharya, and A. Dutta, *Mechanical, Thermal, and Acoustic Properties of Hemp and Biocomposite Materials: A Review.* Journal of Composites Science, 2022. **6**(12).

28. Aigbomian, E.P. and M. Fan, *Development of Wood-Crete building materials from sawdust and waste paper.* Construction and Building Materials, 2013. **40**: p. 361-366.

29. Yates, T., *Final Report on the Construction of the Hemp House at Haverhill, Suffolk.* Building Research Establishment, Watford, England, 2002.

30. Barnat-Hunek, D., P. Smarzewski, and S. Fic, *Mechanical And Thermal Properties Of Hemp-Lime Composites.* Composites Theory and Practice, 2015. **15**(1): p. 21-27.

31. Evrard, A., *Transient hygrothermal behavior of Lime-Hemp Materials.* PhD, Universite Catholique De Louvain., 2008.

32. Latif, E., et al., *Moisture buffer potential of experimental wall assemblies incorporating formulated hemp-lime.* Building and Environment, 2015. **93**: p. 199-209.

33. Stanwix, W. and A. Sparrow, *The Hempcrete Book: Designing and building with hemp-lime.* Green Books, 2014.

34. Shewalul, Y.W., et al., *Fire behavior of hemp blocks: A biomass-based construction material.* Journal of Building Engineering, 2023. **80**.

35. Magwood, C., *Essential Hempcrete Construction*. Sustainable Building Essentials Series. 2016, Canada: New Society Publishers.

36. Zhu, L., et al., *Numerical study on the thermal performance of lightweight temporary building integrated with phase change materials.* Applied Thermal Engineering, 2018. **138**: p. 35-47.

37. Liu, Z.a., et al., *Thermal performance analysis of lightweight building walls in different directions integrated with phase change materials (PCM).* Case Studies in Thermal Engineering, 2022. **40**.

38. McLaggan, M., *Novel fire testing frameworks for Phase Change Materials and hemp-lime insulation*. 2016, Doctor of Philosophy, The University of Edinburgh.

39. Ürge-Vorsatz, D., et al., *Heating and cooling energy trends and drivers in buildings.* Renewable and Sustainable Energy Reviews, 2015. **41**: p. 85-98.

40. GhaffarianHoseini, A., et al., *Sustainable energy performances of green buildings: A review of current theories, implementations and challenges.* Renewable and Sustainable Energy Reviews, 2013. **25**: p. 1-17.

41. Li, C., et al., *Phase change material for passive cooling in building envelopes: A comprehensive review.* Journal of Building Engineering, 2023. **65**: p. 105763.

42. Cuce, E. and S.B. Riffat, *A comprehensive assessment of sectoral energy consumption in the UK: past, present and future.* International Journal of Low-Carbon Technologies, 2016. **11**(3): p. 424-430.

43. Belussi, L., et al., *A review of performance of zero energy buildings and energy efficiency solutions.* Journal of Building Engineering, 2019. **25**.

44. Tirelli, D. and D. Besana, *Moving toward Net Zero Carbon Buildings to Face Global Warming: A Narrative Review.* Buildings, 2023. **13**(3).

45. Kalnæs, S.E. and B.P. Jelle, *Phase change materials and products for building applications: A state-of-the-art review and future research opportunities.* Energy and Buildings, 2015. **94**: p. 150-176.

46. (NRCan)., N.R.C., *Energy efficiency trends in Canada.* 2019.

47. NRDC, *The road from Paris: Canada's progress towards its Climate Pledge.* Natural Resources Defense Council, Issue Brief IB: 16-10-A., November 2016.

48. Balali, A., A. Hakimelahi, and A. Valipour, *Identification and prioritization of passive energy consumption optimization measures in the building industry: An Iranian case study.* Journal of Building Engineering, 2020. **30**: p. 101239.

49. Balali, A., A. Yunusa-Kaltungo, and R. Edwards, *A systematic review of passive energy consumption optimisation strategy selection for buildings through multiple criteria decision-making techniques.* Renewable and Sustainable Energy Reviews, 2023. **171**.

50. Navarro, L., et al., *Thermal energy storage in building integrated thermal systems: A review. Part 2. Integration as passive system.* Renewable Energy, 2016. **85**: p. 1334-1356.

51. Zhang, Y., X. Sun, and M.A. Medina, *A reduced-scale experimental method for the thermal evaluation of building envelopes outfitted with phase change materials.* Journal of Building Engineering, 2022. **62**: p. 105372.

52. Aksamija, A., *Regenerative Design of Existing Buildings for Net-Zero Energy Use.* Procedia Engineering, International Conference on Sustainable Design, Engineering and Construction, 2015. **118**: p. 72 – 80.

53. Gupta, V. and C. Deb, *Envelope design for low-energy buildings in the tropics: A review.* Renewable and Sustainable Energy Reviews, 2023. **186**.

54. Kishore, R.A., et al., *Parametric and sensitivity analysis of a PCM-integrated wall for optimal thermal load modulation in lightweight buildings.* Applied Thermal Engineering, 2021. **187**: p. 116568.

55. Reilly, A. and O. Kinnane, *The impact of thermal mass on building energy consumption.* Applied Energy, 2017. **198**: p. 108-121.

56. Karlsson, J., L. Wadsö, and M. Öberg, *A conceptual model that simulates the influence of thermal inertia in building structures.* Energy and Buildings, 2013. **60**: p. 146-151.

57. Ahangari, M. and M. Maerefat, *An innovative PCM system for thermal comfort improvement and energy demand reduction in building under different climate conditions.* Sustainable Cities and Society, 2019. **44**: p. 120-129.

58. Stritih, U., et al., *Integration of passive PCM technologies for net-zero energy buildings.* Sustainable Cities and Society, 2018. **41**: p. 286-295.

59. Li, G., *Sensible heat thermal storage energy and exergy performance evaluations.* Renewable and Sustainable Energy Reviews, 2016. **53**: p. 897-923.

60. Khudhair, A.M. and M.M. Farid, *A review on energy conservation in building applications with thermal storage by latent heat using phase change materials.* Energy Conversion and Management, 2004. **45**(2): p. 263-275.

61. Gao, Y. and X. Meng, *A comprehensive review of integrating phase change materials in building bricks: Methods, performance and applications.* Journal of Energy Storage, 2023. **62**.

62. Hayatina, I., A. Auckaili, and M. Farid, *Review on the Life Cycle Assessment of Thermal Energy Storage Used in Building Applications.* Energies, 2023. **16**(3).

63. Ali, H.M., et al., *Advances in thermal energy storage: Fundamentals and applications.* Progress in Energy and Combustion Science, 2024. **100**.

64. Zhou, D., C.Y. Zhao, and Y. Tian, *Review on thermal energy storage with phase change materials (PCMs) in building applications.* Applied Energy, 2012. **92**: p. 593-605.

65. Wang, X., et al., *A critical review on phase change materials (PCM) for sustainable and energy efficient building: Design, characteristic, performance and application.* Energy and Buildings, 2022. **260**.

66. Aghakhani, S., et al., *Phase change materials: Agents towards energy performance improvement in inclined, vertical, and horizontal walls of residential buildings.* Journal of Building Engineering, 2022. **56**: p. 104656.

67. Al-Abidi, A.A., et al., *Review of thermal energy storage for air conditioning systems.* Renewable and Sustainable Energy Reviews, 2012. **16**(8): p. 5802-5819.

68. Farajollahi, A., et al., *Reducing the cooling and heating energy of a building in hot and cold climates by employing phase change materials.* Journal of Building Engineering, 2022. **57**: p. 104917.

69. Nazir, H., et al., *Recent developments in phase change materials for energy storage applications: A review.* International Journal of Heat and Mass Transfer, 2019. **129**: p. 491-523.

70. Huang, Y., A. Stonehouse, and C. Abeykoon, *Encapsulation methods for phase change materials – A critical review.* International Journal of Heat and Mass Transfer, 2023. **200**.

71. Tyagi, V.V. and D. Buddhi, *PCM thermal storage in buildings: A state of art.* Renewable and Sustainable Energy Reviews, 2007. **11**(6): p. 1146-1166.

72. Sivanathan, A., et al., *Phase change materials for building construction: An overview of nano-/micro-encapsulation.* 2020. **9**(1): p. 896-921.

73. Mohamed, S.A., et al., *A review on current status and challenges of inorganic phase change materials for thermal energy storage systems.* Renewable and Sustainable Energy Reviews, 2017. **70**: p. 1072-1089.

74. Sharshir, S.W., et al., *Thermal energy storage using phase change materials in building applications: A review of the recent development.* Energy and Buildings, 2023. **285**.

75. Rathod, M.K. and J. Banerjee, *Thermal stability of phase change materials used in latent heat energy storage systems: A review.* Renewable and Sustainable Energy Reviews, 2013. **18**: p. 246-258.

76. Kahwaji, S. and M.A. White, *Prediction of the properties of eutectic fatty acid phase change materials.* Thermochimica Acta, 2018. **660**: p. 94-100.

77. Sharma, R.K., et al., *Developments in organic solid–liquid phase change materials and their applications in thermal energy storage.* Energy Conversion and Management, 2015. **95**: p. 193-228.

78. Png, Z.M., et al., *Strategies to reduce the flammability of organic phase change Materials: A review.* Solar Energy, 2022. **231**: p. 115-128.

79. Ismail, A., et al., *Microencapsulated phase change materials for enhanced thermal energy storage performance in construction materials: A critical review.* Construction and Building Materials, 2023. **401**.

80. Muzhanje, A.T., et al., *An overview of the preparation and characteristics of phase change materials with nanomaterials.* Journal of Energy Storage, 2022. **51**: p. 104353.

81. Lecompte, T., et al., *Mechanical and thermo-physical behaviour of concretes and mortars containing phase change material.* Energy and Buildings, 2015. **94**: p. 52-60.

82. Franquet, E., et al., *Experimental and theoretical analysis of a cement mortar containing microencapsulated PCM.* Applied Thermal Engineering, 2014. **73**(1): p. 32-40.

83. Toppi, T. and L. Mazzarella, *Gypsum based composite materials with micro-encapsulated PCM: Experimental correlations for thermal properties estimation on the basis of the composition.* Energy and Buildings, 2013. **57**: p. 227-236.

84. Fenollera, M., et al., *The Influence of Phase Change Materials on the Properties of Self-Compacting Concrete.* Materials (Basel), 2013. **6**(8): p. 3530-3546.

85. Navarro, L., et al., *Thermal energy storage in building integrated thermal systems: A review. Part 1. active storage systems.* Renewable Energy, 2016. **88**: p. 526-547.

86. Ben Romdhane, S., et al., *A review on thermal energy storage using phase change materials in passive building applications.* Journal of Building Engineering, 2020. **32**.

87. Li, L., H. Yu, and R. Liu, *Research on composite-phase change materials (PCMs)-bricks in the west wall of room-scale cubicle: Mid-season and summer day cases.* Building and Environment, 2017. **123**: p. 494-503.

88. Liu, L., et al., *Description of phase change materials (PCMs) used in buildings under various climates: A review.* Journal of Energy Storage, 2022. **56**.

89. Jin, X., et al., *Effects of PCM state on its phase change performance and the thermal performance of building walls.* Building and Environment, 2014. **81**: p. 334-339.

90. Sadineni, S.B., S. Madala, and R.F. Boehm, *Passive building energy savings: A review of building envelope components.* Renewable and Sustainable Energy Reviews, 2011. **15**(8): p. 3617-3631.

91. Baylis, C. and C.A. Cruickshank, *Review of bio-based phase change materials as passive thermal storage in buildings.* Renewable and Sustainable Energy Reviews, 2023. **186**.

92. Aelenei, D. and F.M.A. Henriques, *Analysis of the condensation risk on exterior surface of building envelopes.* Energy and Buildings, 2008. **40**(10): p. 1866-1871.

93. Memon, S.A., *Phase change materials integrated in building walls: A state of the art review.* Renewable and Sustainable Energy Reviews, 2014. **31**: p. 870-906.

94. Konuklu, Y., et al., *Review on using microencapsulated phase change materials (PCM) in building applications.* Energy and Buildings, 2015. **106**: p. 134-155.

95. Tyagi, V.V., et al., *Development of phase change materials based microencapsulated technology for buildings: A review.* Renewable and Sustainable Energy Reviews, 2011. **15**(2): p. 1373-1391.

96. Cárdenas-Ramírez, C., F. Jaramillo, and M. Gómez, *Systematic review of encapsulation and shape-stabilization of phase change materials*. Journal of Energy Storage, 2020. **30**.

97. Bastani, A., F. Haghighat, and J. Kozinski, *Designing building envelope with PCM wallboards: Design tool development.* Renewable and Sustainable Energy Reviews, 2014. **31**: p. 554-562.

98. Rathore, P.K.S. and S.K. Shukla, *Potential of macroencapsulated PCM for thermal energy storage in buildings: A comprehensive review.* Construction and Building Materials, 2019. **225**: p. 723-744.

99. Zastawna-Rumin, A. and K. Nowak, *Effects of Neglecting PCM Hysteresis While Making Simulation Calculations of a Building Located in Polish Climatic Conditions.* Applied Sciences, 2021. **11**(19).

100. Biswas, K., et al., *Thermal characterization of full-scale PCM products and numerical simulations, including hysteresis, to evaluate energy impacts in an envelope application.* Applied Thermal Engineering, 2018. **138**: p. 501-512.

101. Que, L., et al., *Numerical simulation and experimental research progress of phase change hysteresis: A review.* Energy and Buildings, 2021. **253**.

102. Abdellatef, Y., et al., *Hysteresis model predictions of thermal performance of hempcrete-based walls with phase change materials.* Journal of Building Engineering, 2024. **84**.

103. Chandrasekharan, R., et al., *An enhanced simulation model for building envelopes with phase change materials.* ASHRAE Transactions, 2013. **119**(2): p. 1-10.

104. Gasia, J., et al., *Use of partial load operating conditions for latent thermal energy storage management.* Applied Energy, 2018. **216**: p. 234-242.

105. Delcroix, B., M. Kummert, and A. Daoud, *Thermal Behavior Mapping of a Phase Change Material Between the Heating and Cooling Enthalpy-temperature Curves.* Energy Procedia, 2015. **78**: p. 225-230.

106. Barz, T., *Paraffins as phase change material in a compact plate-fin heat exchanger - Part II: Validation of the "curve scale" hysteresis model for incomplete phase transitions.* Journal of Energy Storage, 2021. **34**.

107. Dutil, Y., et al., *Modeling phase change materials behavior in building applications: Comments on material characterization and model validation.* Renewable Energy, 2014. **61**: p. 132-135.

108. Stanwix, W. and A. Sparrow, *The Hempcrete Book: Designing and Building with Hemp-lime*. 2014: Green Books.

109. Pochwala, S., et al., *The Heat Conductivity Properties of Hemp-Lime Composite Material Used in Single-Family Buildings.* Materials (Basel), 2020. **13**(4).

110. Collet, F. and S. Pretot, *Thermal conductivity of hemp concretes: Variation with formulation, density and water content.* Construction and Building Materials, 2014. **65**: p. 612-619.

111. Abdellatef, Y., et al., *Mechanical, Thermal, and Moisture Buffering Properties of Novel Insulating Hemp-Lime Composite Building Materials.* Materials (Basel), 2020. **13**(21).

112. Abdellatef, Y., M. Kavgic, and R. Foruzanmehr, *THERMAL AND MOISTURE BUFFERING PROPERTIES OF NOVEL HEMP-LIME COMPOSITES INTEGRATED WITH MICROENCAPSULATED PHASE CHANGE MATERIALS.* Proceedings of the 4th International Conference on Bio-based Building Materials, Barcelona, Spain, 2021.

113. Magwood, C., *Essential Hempcrete Construction: The Complete Step-by-Step Guide.* New Society Publishers., 2016.

114. Jami, T., D. Rawtani, and Y.K. Agrawal, *Hemp concrete: carbon-negative construction.* Emerging Materials Research, 2016. **5**(2): p. 240-247.

115. Florentin, Y., et al., *A life-cycle energy and carbon analysis of hemp-lime bio-composite building materials.* Energy and Buildings, 2017. **156**: p. 293-305.

116. Rivas-Aybar, D., M. John, and W. Biswas, *Can the Hemp Industry Improve the Sustainability Performance of the Australian Construction Sector?* Buildings, 2023. **13**(6).

117. Bevan, R. and T. Woolley. *Constructing a low energy house from hempcrete and other natural materials*. in *Proceedings of the 11th International Conference on Non-conventional Materials and Technologies (NOCMAT 2009), Bath, UK*. 2009.

118. Ip, K. and A. Miller, *Life cycle greenhouse gas emissions of hemp–lime wall constructions in the UK.* Resources, Conservation and Recycling, 2012. **69**: p. 1-9.

119. Busbridge, R. and R. Rhydwen. *An investigation of the thermal properties of hemp and clay monolithic walls*. in *Proceedings of Advances in Computing and Technology,(AC&T) The School of Computing and Technology 5th Annual Conference, University of East London, pp*. 2010.

120. Rhydwen, R., et al. *Dry-lining versus a hemp and lime insulating render for internal thermal renovation of a stone cottage in West Wales, including embodied energy assessment, interstitial wall monitoring, in-situ U-value and WUFI modelling*. in *Retrofit 2012 Academic Conference, Salford University, UK*. 2012.

121. Cérézo, V., *Propriétés mécaniques, thermiques et acoustiques d'un matériau à base de particules végétales : approche expérimentale et modélisation théorique.* Le grade de docteur L'Institut National des Sciences Appliquées de Lyon., 2005.

122. Walker, R., S. Pavia, and R. Mitchell, *Mechanical properties and durability of hemp-lime concretes.* Construction and Building Materials, 2014. **61**: p. 340-348.

123. Lawrence, M., et al., *Hygrothermal Performance of an Experimental Hemp-Lime Building.* Key Engineering Materials, 2012. **517**: p. 413-421.

124. Walker, R. and S. Pavía, *Moisture transfer and thermal properties of hemp–lime concretes.* Construction and Building Materials, 2014. **64**: p. 270-276.

125. Nguyen, T.-T., et al., *Influence of compactness and hemp hurd characteristics on the mechanical properties of lime and hemp concrete.* European Journal of Environmental and Civil Engineering, 2009. **13**(9): p. 1039-1050.

126. MANH, D.T., *Contribution to the development of precast hempcrete using innovative pozzolanic binder.* Doctoral dissertation Université Toulouse III-Paul Sabatier, 2014.

127. Ntimugura, F., et al., *Mechanical, thermal, hygroscopic and acoustic properties of bio-aggregates – lime and alkali - activated insulating composite materials: A review of current status and prospects for miscanthus as an innovative resource in the South West of England.* Sustainable Materials and Technologies, 2020. **26**.

128. Williams, J., M. Lawrence, and P. Walker, *The influence of the casting process on the internal structure and physical properties of hemp-lime.* Mater Struct, 2017. **50**(2): p. 108.

129. Seng, B., C. Magniont, and S. Lorente, *Characterization of a precast hemp concrete. Part I: Physical and thermal properties.* Journal of Building Engineering, 2019. **24**: p. 100540.

130. de Bruijn, P. and P. Johansson, *Moisture fixation and thermal properties of lime–hemp concrete.* Construction and Building Materials, 2013. **47**: p. 1235-1242.

131. Arnaud, L., B. Boyeux, and Y. Hustache, *Hemp and the Construction Industry, Hemp: Industrial Production and Uses.* CABI, 2013: p. 239-259.

132. Rahim, M., et al., *Effect of moisture and temperature on thermal properties of three bio-based materials.* Construction and Building Materials, 2016. **111**: p. 119-127.

133. Maalouf, C., et al., *Effect of moisture transfer on thermal inertia in simple layer walls, Case of a vegetal fibre material.* 2011. **5**(1): p. 33-47.

134. Ahlberg, J., E. Georges, and M. Norlén, *The potential of hemp buildings in different climates : A comparison between a common passive house and the hempcrete building system*, in *TVE*. 2014. p. 59.

135. Abdellatef, Y. and M. Kavgic, *Thermal, microstructural and numerical analysis of hempcrete-microencapsulated phase change material composites.* Applied Thermal Engineering, 2020. **178**.

136. Mukherjee, A. and C. MacDougall, *Structural benefits of hempcrete infill in timber stud walls.* International Journal of Sustainable Building Technology and Urban Development, 2013. **4**(4): p. 295-305.

137. Elfordy, S., et al., *Mechanical and thermal properties of lime and hemp concrete ("hempcrete") manufactured by a projection process.* Construction and Building Materials, 2008. **22**(10): p. 2116-2123.

138. Murphy, F., S. Pavia, and R. Walker, *An assessment of the physical properties of lime-hemp concrete.* Proceeding of the bridge concrete research in Ireland, Cork, 2010.

139. Cigasova, J., N. Stevulova, and J.J.C.E.T. Junak, *Innovative use of biomass based on technical hemp in building industry.* 2014. **37**.

140. Tronet, P., et al., *Study of lime hemp composite precasting by compaction of fresh mix — An instrumented die to measure friction and stress state.* Powder Technology, 2014. **258**: p. 285–296.

141. Rode, C., et al., *NORDTEST Project on Moisture Buffer Value of Materials.* In AIVC 26th conference: Ventilation in relation to the energy performance of buildings, 2005: p. 47-52.

142. Collet, F., et al., *Comparison of the hygric behaviour of three hemp concretes.* Energy and Buildings, 2013. **62**: p. 294-303.

143. Collet, F. and S. Pretot, *Experimental investigation of moisture buffering capacity of sprayed hemp concrete.* Construction and Building Materials, 2012. **36**: p. 58-65.

144. McLaggan, M.S. *Novel fire testing frameworks for Phase Change Materials and hemp-lime insulation*. 2016.

145. McLaggan, M.S., R.M. Hadden, and M. Gillie, *Flammability assessment of phase change material wall lining and insulation materials with different weight fractions.* Energy and Buildings, 2017. **153**: p. 439-447.

146. Kumarasamy, K., et al., *Novel CFD-based numerical schemes for conduction dominant encapsulated phase change materials (EPCM) with temperature hysteresis for thermal energy storage applications.* Energy, 2017. **132**: p. 31-40.

147. C136–06, A., *ASTM C136–06, Standard Test Method for Sieve Analysis of Fine and Coarse Aggregates*, in *ASTM International, West Conshohocken, PA.* 2006.

148. C207-06, A., *ASTM C207-06, Standard Specification for Hydrated Lime for Masonry Purposes.* ASTM International, West Conshohocken, PA., 2006.

149. C618, A., *ASTM C618, Standard Specification for Coal Fly Ash and Raw or Calcined Natural Pozzolan for Use in Concrete.* ASTM International, West Conshohocken, PA., 2012.

150. C1707, A., *ASTM C1707, Standard Specification for Pozzolanic Hydraulic Lime for Structural Purposes.* ASTM International, West Conshohocken, PA., 2009.

151. Nguyen, T.T., *Contribution à l'étude de la formulation et du procédé de fabrication d'éléments de construction en béton de chanvre.* Doctoral dissertation Université de Bretagne Sud, Français., 2010.

152. Evrard, A. and A.D. Herde, *Bioclimatic envelopes made of lime and hemp concrete.* at CISBAT2005 Conference - Renewables in a Changing Climate - Innovation in Building Envelopes and Environmental Systems at Lausanne., 2005.

153. Pinkos, J., *The Effectiveness of Hempcrete as an Infill Insulation in the Prairies Compared to a Standard Building Based on Power Consumption.* Master of Science, Faculty of Engineering, University of Manitoba, 2014.

154. C39M, A.C., *ASTM C39 / C39M, Standard Test Method for Compressive Strength of Cylindrical Concrete Specimens.* ASTM International, West Conshohocken, PA., 2012.

155. C496M-17, A.C., *ASTM C496 / C496M-17, Standard Test Method for Splitting Tensile Strength of Cylindrical Concrete Specimens*, in *ASTM International, West Conshohocken, PA*. 2017.

156. D4832, A., *ASTM D4832-16e1, Standard Test Method for Preparation and Testing of Controlled Low Strength Material (CLSM) Test Cylinders.* ASTM International, West Conshohocken, PA, 2016.

157. C518–17, A., *ASTM C518–17, Standard Test Method for Steady-State Thermal Transmission Properties by Means of the Heat Flow Meter Apparatus.* ASTM International, West Conshohocken, PA., 2017.

158. NIST-1450b-SRM, *NIST SRM 1450, "Energy and Environment Division, NIST." https://www.nist.gov/ energy-and environment-division/nist-srm-1450.*

159. C1784-14, A., *ASTM C1784-14, Standard Test Method for Using a Heat Flow Meter Apparatus for Measuring Thermal Storage Properties of Phase Change Materials and Products.* ASTM International, West Conshohocken, PA., 2014.

160. Tleoubaev, A. and A. Brzezinski, *Thermal Diffusivity and Volumetric Specific Heat Measurements Using Heat Flow Meter Instruments.* presented at the Thermal Conductivity 29/Thermal Expansion 17 Conference, Birmingham, Alabama, 2007.

161. Ge, H., et al., *Influence of moisture load profiles on moisture buffering potential and moisture residuals of three groups of hygroscopic materials.* Building and Environment, 2014. **81**: p. 162-171.

162. Li, Y., P. Fazio, and J. Rao, *An investigation of moisture buffering performance of wood paneling at room level and its buffering effect on a test room.* Building and Environment, 2012. **47**: p. 205-216.

163. R. Eires, et al., *New Eco-Friendly Hybrid Composite Materials For Civil Construction.* In European Conference on Composite Materials Biarritz., 2006.

164. Hirst, E., et al. *Characterisation of low density hemp-lime composite building materials under compression loading*. in *Second international conference on sustainable construction materials and technologies*. 2010.

165. Tran Le, A.D., et al., *Transient hygrothermal behaviour of a hemp concrete building envelope.* Energy and Buildings, 2010. **42**(10): p. 1797-1806.

166. Nguyen, T.T., et al., *Effect of compaction on mechanical and thermal properties of hemp concrete.* European Journal of Environmental and Civil Engineering, 2010. **14**(5): p. 545-560.

167. Murphy, F., S. Pavía, and R. Walker, *An assessment of some physical properties of hemp-lime concrete.* Proceedings of the BCRI bridge infrastructure concrete research ireland, Univ. of Cork, Ireland, 2010: p. 431–438.

168. Laboratories, M., *Microtek Laboratories Inc. "MPCM Technical Information." https://www.microteklabs.com/.*

169. Liu, Y. and D.J. Harris, *Measurements of wind speed and convective coefficient on the external surface of a low-rise building.* International Journal of Ambient Energy, 2015. **36**(5): p. 225-234.

170. Mirsadeghi, M., et al., *Review of external convective heat transfer coefficient models in building energy simulation programs: Implementation and uncertainty.* Applied Thermal Engineering, 2013. **56**(1-2): p. 134-151.

171. Awbi, H.B. and A. Hatton, *Natural convection from heated room surfaces.* Energy and Buildings, 1999. **30**(3): p. 233-244.

172. Hunger, M., et al., *The behavior of self-compacting concrete containing micro-encapsulated Phase Change Materials.* Cement and Concrete Composites, 2009. **31**(10): p. 731-743.

173. Fernandes, F., et al., *On the feasibility of using phase change materials (PCMs) to mitigate thermal cracking in cementitious materials.* Cement and Concrete Composites, 2014. **51**: p. 14-26.

174. Su, J.-F., et al., *Preparation and characterization of polyurethane microcapsules containing n-octadecane with styrene-maleic anhydride as a surfactant by interfacial polycondensation.* Journal of Applied Polymer Science, 2006. **102**(5): p. 4996-5006.

175. Shukla, N. and J. Kosny, *DHFMA Method for Dynamic Thermal Property Measurement of PCM-integrated Building Materials.* Current Sustainable/Renewable Energy Reports, 2015. **2**(2): p. 41-46.

176. Diaconu, B.M., S. Varga, and A.C. Oliveira, *Experimental assessment of heat storage properties and heat transfer characteristics of a phase change material slurry for air conditioning applications.* Applied Energy, 2010. **87**(2): p. 620-628.

177. Bony, J. and S. Citherlet, *Numerical model and experimental validation of heat storage with phase change materials.* Energy and Buildings, 2007. **39**(10): p. 1065-1072.

178. Andrássy, Z. and Z. Szánthó, *Thermal behaviour of materials in interrupted phase change.* Journal of Thermal Analysis and Calorimetry, 2019. **138**(6): p. 3915-3924.

179. Serikawa, M., et al., *Measurement of full-scale phase change material products considering hysteresis.* Applied Thermal Engineering, 2021. **192**.

180. *PureTemp. "Global Authority On Phase Change Material®.*

181. Guarino, F., et al., *PCM thermal storage design in buildings: Experimental studies and applications to solaria in cold climates.* Applied Energy, 2017. **185**: p. 95-106.

Appendix

A. Approximate Young modulus of hempcrete samples

Table A.1. Approximate Young's modulus and density of all hempcrete samples.

Design mix	Name		Density (kg/m^3)	E (MPa)
Hydrated Lime-Crushed Brick	LCB10	A	344	10.42
		B	337	6.02
	LCB20	A	323	6.38
		B	318	3.16
Hydrated Lime-Metakaolin	LMK20	A	325	7.20
		B	358	9.00
	LMK50	A	368	8.05
		B	353	8.31
	LMK70	A	314	7.64
		B	324	4.00
Hydrated Lime-Natural Hydraulic Lime	LNHL50	A	334	9.01
		B	350	5.21
	LNHL70	A	337	10.22
		B	352	8.22

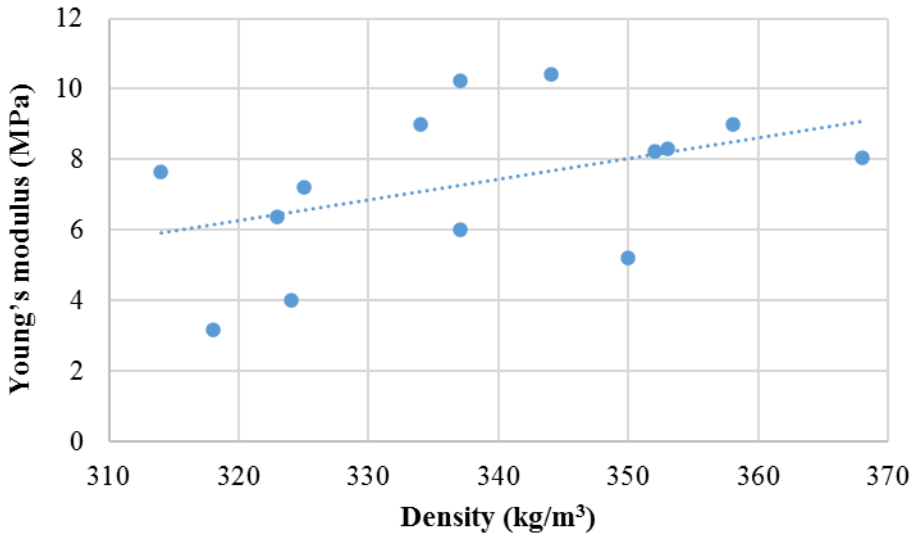

Figure A.1. Approximate Young's modulus and density of hempcrete samples.

As presented, the approximate modulus of elasticity shows a wide variation between design mixes and a weak relationship with the samples' density. Thus, approximate Young's modulus ranges from 3.16 to 10.42 MPa, and the average value of all samples is 7.35 MPa, with a standard deviation of 2.096 MPa (~28%). Increasing the CB content reduces Young's modulus in both water contents, with the same trend in MK samples only in high water content. On the other hand, increasing NHL slightly increases Young's modulus in both water contents. The LCB20B shows the lowest value of Young's modulus (3.16 MPa), followed by LMK70B (4.00 MPa). In contrast, the LCB10A has the highest Young's modulus (10.42 MPa), followed by LNHL70A (10.22 MPa). While increasing water content in CB and NHL samples decreases Young's modulus, it increases it in MK samples (except LMK70 samples).

B. Moisture buffering values of selected HPCM samples

Figure B.1 presents three hempcrete samples' moisture buffering values from each design mix (LMK50, LNHL50, LCB10), compared to HPCM samples with the highest encapsulation efficiency in each MPCM product (HPCM18 in Nextek, HPCM25 in Micronal). The average MBV for all hempcrete samples is 2.78 (gm/m^2 RH%), with a standard deviation of (0.24 gm/m^2 RH%) (8.6%). Moreover, the average MBV for all HPCM samples was 2.76 (gm/m^2 RH%), with a standard deviation of (0.12 gm/m^2 RH%) (4.3%). These results indicate that all HPCM and hempcrete samples have excellent moisture buffering performance (MBV > 2). For example, Collet et al. (2013) reported an MBV of 2.14 (gm/m^2 %RH), with a binder-to-hemp ratio of 2:1 and density of 430 kg/m^3 [142], while Latif et al. (2015) reported an MBV of 3.47 (gm/m^2 %RH) with a binder to hemp ratio of 1.2:1 and density of 290 kg/m^3 [32]. The figure shows that all HPCM samples have higher MBV than the base hempcrete sample (LMK50), with the Micronal samples showing higher values. The figure also shows that increasing MPCM share from 9% to 18%

slightly decreases moisture buffering values but is still in the excellent performance category (MBV > 2).

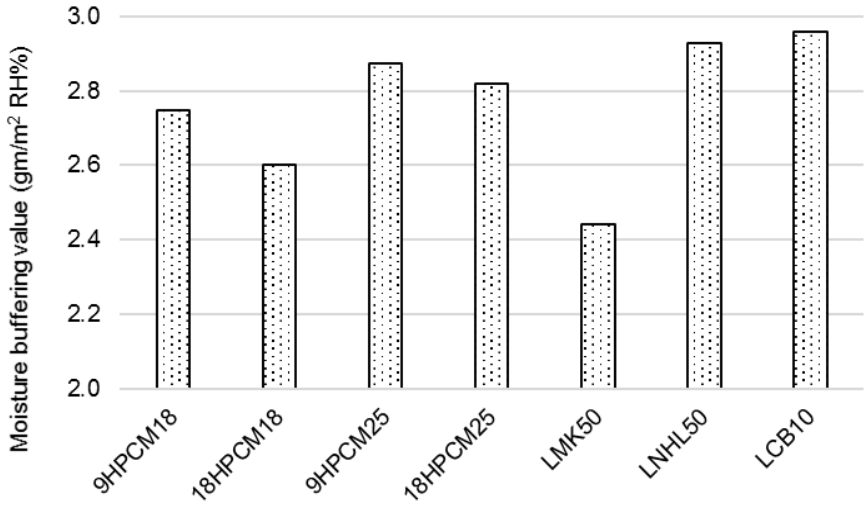

Figure B.1. Moisture buffering values (MBV) for selected HPCM and hempcrete samples.

C. Flow charts for the hysteresis model codes

Figure C.1 illustrates the logic used to implement the hysteresis approaches into the C language.

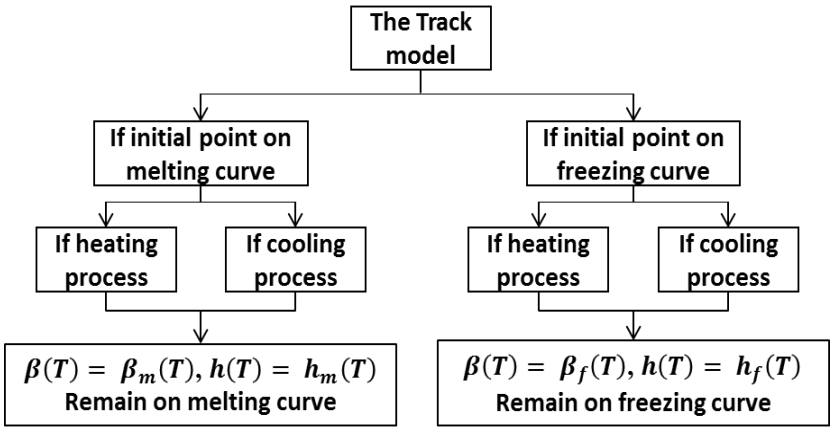

a) The Track model.

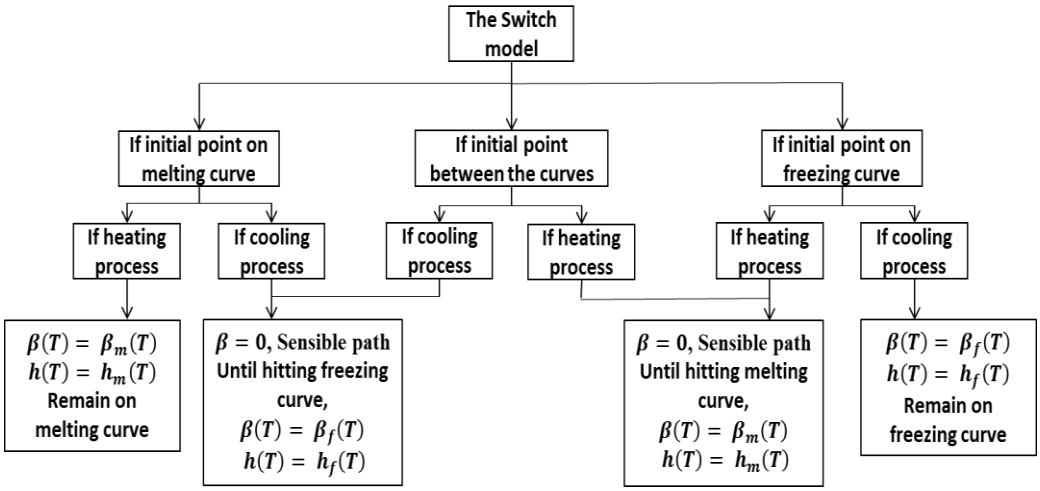

b) The Switch model.

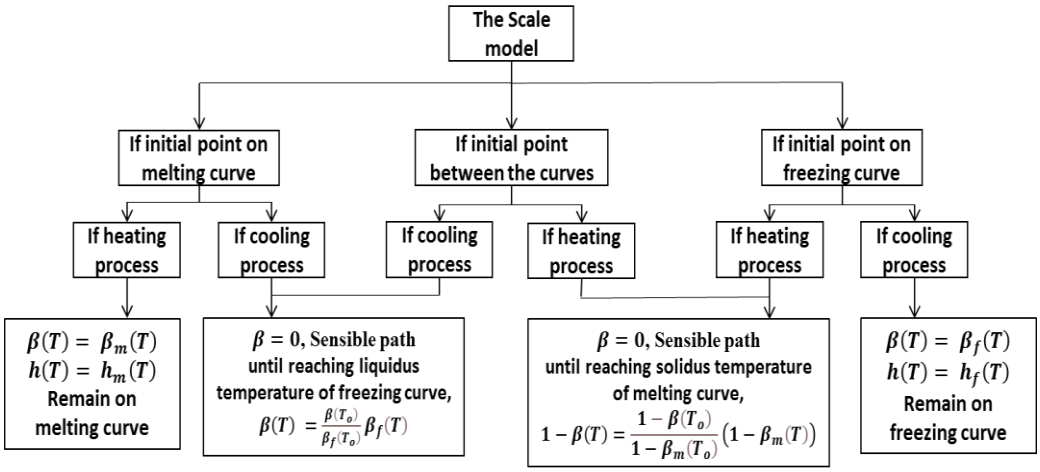

c) The Scale model.

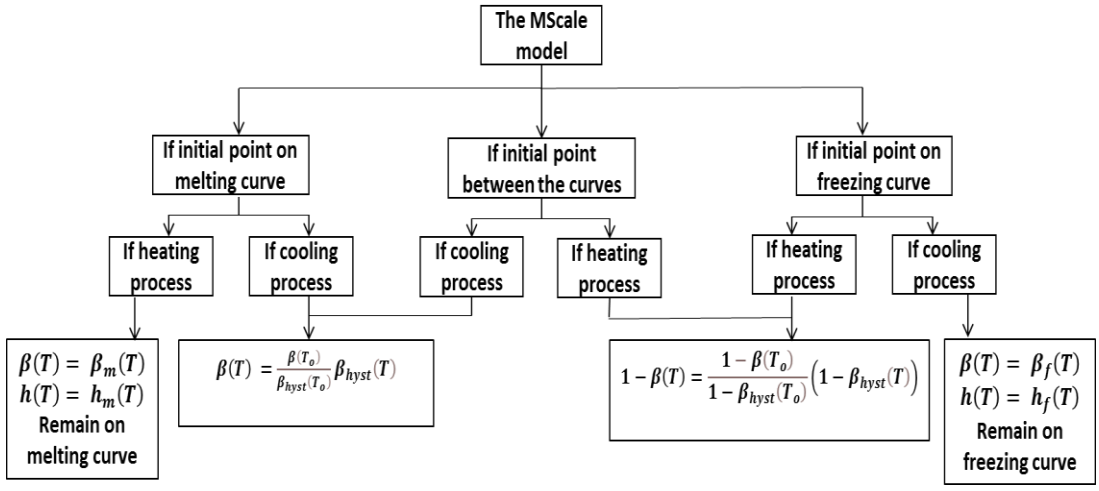

d) The MScale model.

Figure C.1. Simplified flow charts for the four hysteresis models in interrupted phase change processes. In d), $\beta(T_o)$ is the liquid fraction of the initial point.

D. PCM cycles and weather conditions

In addition to the daily PCM cycle of storage (during the day) and release (during the night), random weather conditions can create broader PCM cycles. For example, from days 9 to 14, the outdoor temperature increases, reaching its highest in January, which results in lower energy consumption and higher liquid fractions (PCM charging). On the other hand, from days 15 to 20, the outdoor temperature decreases, reaching its lowest in January, which results in higher energy consumption and lower liquid fractions (PCM release). The following are examples of such phenomena.

D.1. The H-Panel wall in SCH2 (Chapter 7).

As shown in the table, the Track model has the highest energy consumption in the first period, followed by the MScale, the Scale, and the Switch model. In the second period, the Track model has the lowest energy consumption as it releases energy absorbed in the first period. The Switch and Scale models show the opposite performance of the Track because of its sensible transition feature, and the MScale comes with in-between performance.

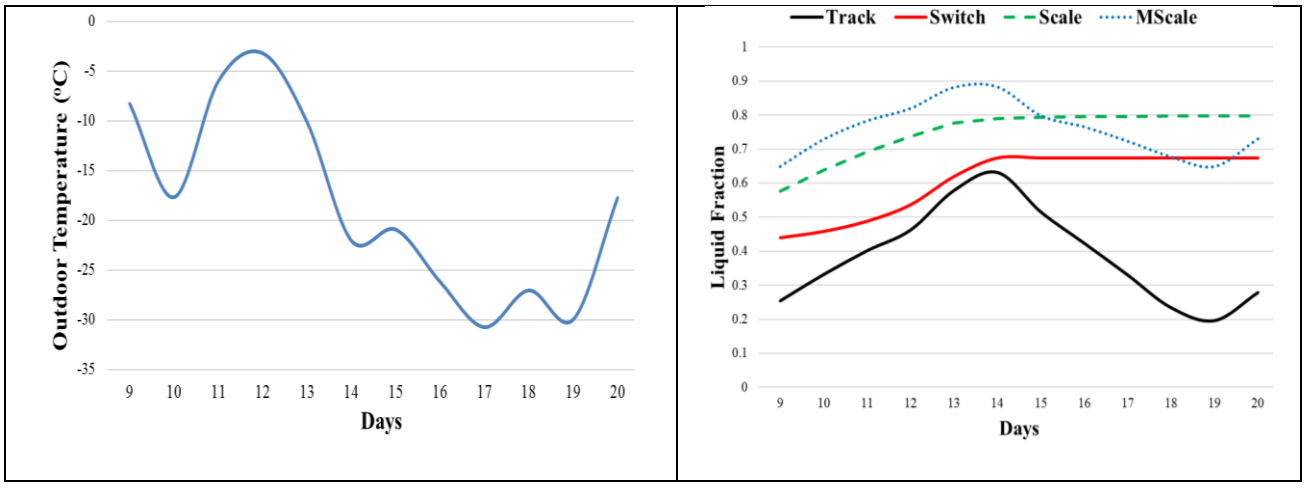

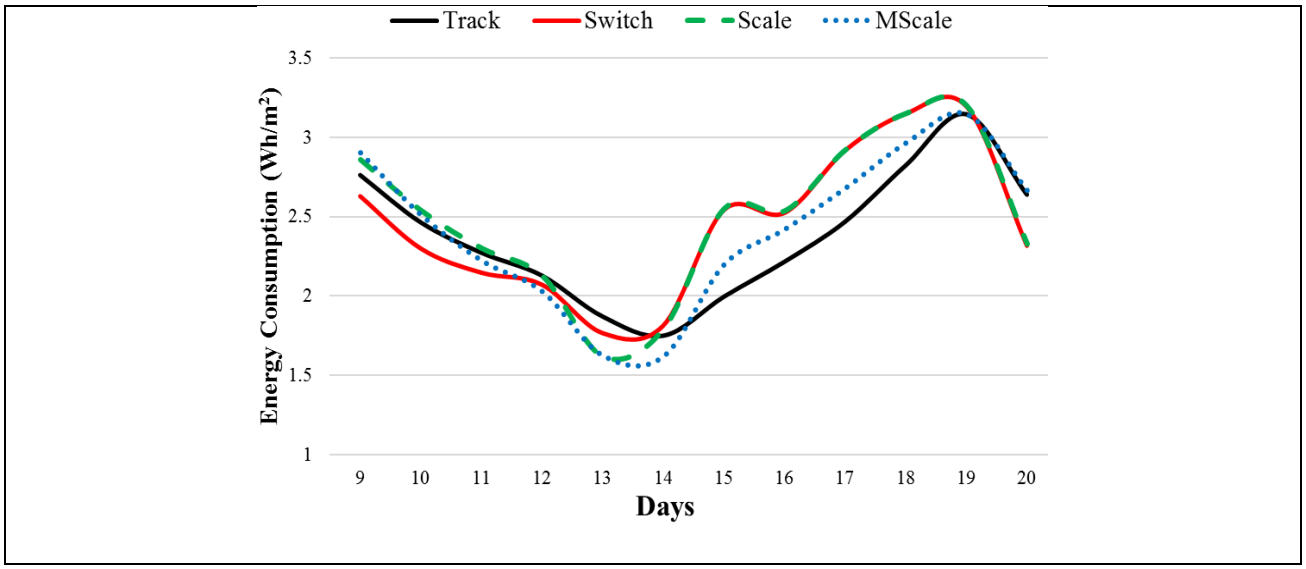

Figure D.1. Outdoor temperature, energy consumption, and liquid fraction profiles at the period (days 9-20) in January.

Table D.1. Energy consumption for all hysteresis models in the H-Panel wall at the two periods.

	H-Panel			
	Track	Switch	Scale	MScale
Days (9-14)	1272	1221	1225	1239
Days (15-20)	1468	1597	1586	1543
Percentage increase%	15.4	30.8	29.5	24.5
Total	2740	2818	2811	2782

D.2. The H-Micro wall in SCH1 (Chapter 5).

The case of the hempcrete, 9HPCM18, and 18HPCM18 walls, at SCH1. As shown in the table and figure, the 18HPCM18 wall has the highest energy consumption in the first period. In the second period, the 18HPCM18 wall has the lowest energy consumption as it releases energy absorbed in the first period. The hempcrete wall show the opposite performance of the 18HPCM18 wall (no latent storage). However, the 9HPCM18 wall shows the largest savings on the total consumption.

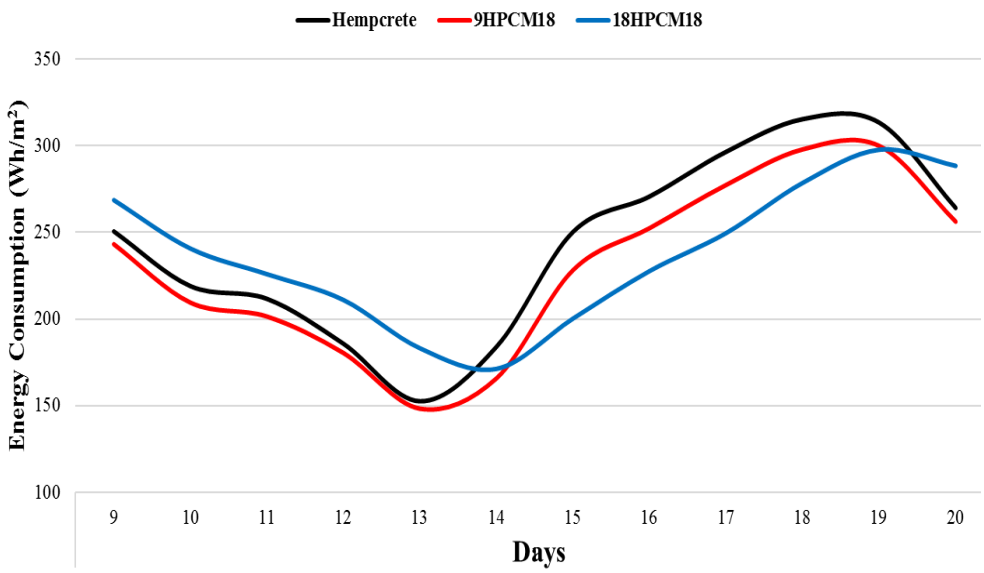

Figure D.2. Energy consumption profiles at the period (days 9-20) in January.

Table D.2. Energy consumption for hempcrete and HPCM18 walls at the two periods.

	H-Panel		
	Hempcrete	9HPCM18	18HPCM18
Days (9-14)	1204	1178	1301
Days (15-20)	1712	1570	1543
Percentage increase%	42	33	19
Total	2916	2749	2844

E. Chemical composition of binders and pozzolans

The following table and figure illustrate the chemical composition of the binders and pozzolans used, and the SEM images for the composites' ingredients.

Table E.1. Chemical composition of binders and additives by weight as per the manufacturers.

Chemical compounds	Hydrated lime (%)	Metakaolin (%)	Natural Hydraulic Lime (%)	Crushed Brick (%)
$Ca(OH)_2$	87 - 99	-	30 - 60	-
MgO	-	0.30	-	-
CaO	-	0.379	-	-
Crystalline SiO_2	0.0001 to 1	60.434	0.0001 - 1	50-60

Al_2O_3	-	31.200	-	20-30
K_2O	-	1.826	-	-
Na_2O	-	0.197	-	-
Fe_2O_3	-	1.106	-	-
SO_3	-	0.029	-	-
Na_2O	-	0.197	-	-
P_2O_5	-	0.031	-	-
TiO_2	-	0.642		-
Mn_2O_3	-	0.007	-	-
SrO	-	0.012	-	-
ZnO	-	0.011		-
$CaHMgO^{+3}$ or CaMg(OH)4	-	-	60 - 100	-
CaH_2MgO_3 or CaMg(OH)2O	-	-	60 - 100	-

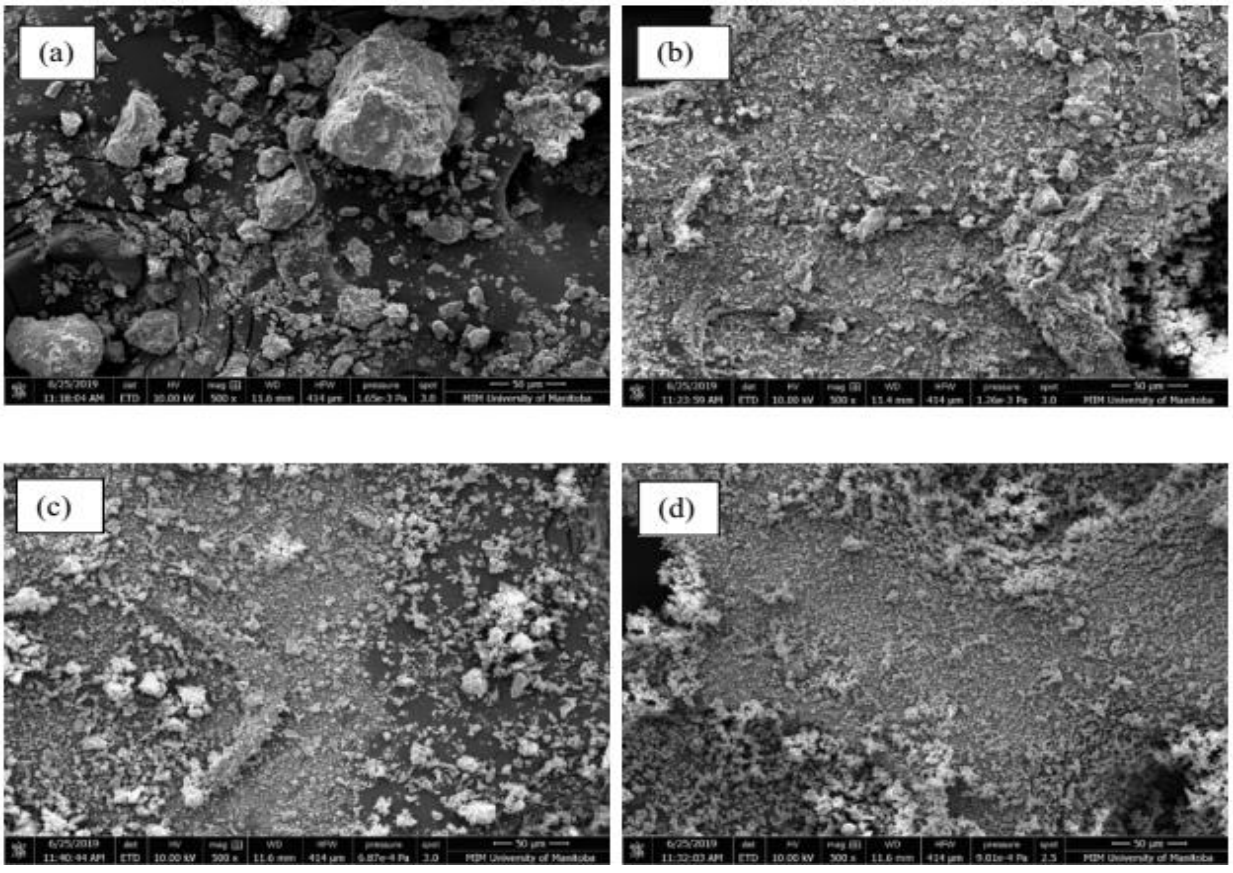

Figure E.1. Microstructural images of ingredients: a) Crushed Brick; b) Metakaolin; c) Natural hydraulic lime (NHL 5); d) Hydrated lime. All images at magnification of 50 µm.